TECHNISCHE UNIVERSITÄT DRESDEN

Fakultät Forst-, Geo- und Hydrowissenschaften

Potential of Spaceborne X & L-Band SAR-Data for Soil Moisture Mapping Using GIS and its Application to Hydrological Modelling: the Example of Gottleuba Catchment, Saxony / Germany

Dissertation zur Erlangung des akademischen Grades
Doktoringenieur (Dr.-Ing.)

vorgelegt von

M.Sc. Samy Gamal Khedr Elbialy

Gutachter:

Herr Prof. Dr.phil.habil. Manfred F. Buchroithner
Technische Universität Dresden

Herr Prof. Dr.-Ing. Uwe Sörgel
Leibniz-Universität Hannover

Dresden, den 08. März 2011

Erklärung des Promovenden

Die Übereinstimmung dieses Exemplars mit dem Original der Dissertation zum Thema:

"Potential of Spaceborne X & L-Band SAR-Data for Soil Moisture Mapping Using GIS and ist Application to Hydrological Modelling: the Example of Gottleuba Catchment, Saxony / Germany"

wird hiermit bestätigt.

……..…
Ort, Datum

……..…
Unterschrift (Vorname Name)

Anything is possible if you wish hard enough

(James Matthew Barrie)

Declaration

I hereby certify that the PhD thesis entitled

Potential of Spaceborne X & L- Band SAR-Data for Soil Moisture Mapping Using GIS and its Application to Hydrological Modelling: the Example of Gottleuba Catchment, Saxony / Germany

is a bona fide record of research work carried out by me without any assistance and that it has not been submitted in any previous application for a higher degree.

Dresden, …….

.....

Acknowledgements

This thesis was carried out in the Institute for Cartography, Dresden University of Technology, Germany. In this context I would like to express special thanks to my academic advisor Prof. Dr. Manfred Buchroithner who was a distinct supervisor and gave numerous critical comments as well as various ideas for structuring the present thesis. I also want to express my gratitude to the whole academic stuff of the institute, especially Mrs. Sharma for her efforts to communicate the various authorities to achieve this work.

My gratitude goes to the *Staatsbetrieb Geobasisinformation und Vermessung Sachsen* (GeoSN) for supporting and providing the data used in this study. Thanks to Mr. Hagen Linke from the *Landestalsperrenverwaltung des Freistaates Sachsen* (LTV) for providing storage and hydrological data. Dr. Johannes Franke from Institute of Hydrology and Meteorology, Dresden University of Technology, is gratefully acknowledged for collection and provision of meteorological data.

I would like to express my deep thanks to Mrs. Antje Peter from the *Sächsisches Landesamt für Umwelt, Landwirtschaft und* Geologie (LfULG) for supplying precipitation and discharge data. Great thanks to Thomas Hahmann from the *Deutsches Luft- und Raumfahrtzentrum* (DLR) for providing the required TerraSAR-X data.

During the field work I used equipments which were borrowed from the Institute of Hydrology and Meteorology, Dresden University of Technology. Thus I would like to thank Mr. Heiko Prasse for his nice cooperation. Many thanks also go to the Institute of Geography, Dresden University of Technology to permit me to use the laboratory to measure the soil moisture for the collected field samples.

I also want to thank the Cultural Affairs & Mission Sector, Ministry of Higher Education of Egypt, for awarding a PhD scholarship.

Last but not least, very special thanks go to my family and in particular to my wife Amany and my two daughters Rawan, Noran and Myiar for the support, inspiration and patience which I could always count on. Very special thanks go to my mother and to my father's spirit.

Abstract

Hydrological modelling is a powerful tool for hydrologists and engineers involved in the planning and development of integrated approach for the management of water resources. With the recent advent of computational power and the growing availability of spatial data, RS and GIS technologies can augment to a great extent the conventional methods used in rainfall runoff studies; it is possible to accurately describe watershed characteristics in particularly when determining runoff response to rainfall input. The main objective of this study is to apply the potential of spaceborne SAR data for soil moisture retrieval in order to improve the spatial input parameters required for hydrological modelling. For the spatial database creation, high resolution 2 m aerial laser scanning Digital Terrain Model (DTM), soil map, and landuse map were used. Rainfall records were transformed into a runoff through hydrological parameterisation of the watershed and the river network using HEC-HMS software for rainfall runoff simulation. The Soil Conservation Services Curve Number (SCS-CN) and Soil Moisture Accounting (SMA) loss methods were selected to calculate the infiltration losses. In microwave remote sensing, the study of how the microwave interacts with the earth terrain has always been interesting in interpreting the satellite SAR images. In this research soil moisture was derived from two different types of Spaceborne SAR data; TerraSAR-X and ALOS PALSAR (L band). The developed integrated hydrological model was applied to the test site of the Gottleuba Catchment area which covers approximately 400 sqkm, located south of Pirna (Saxony, Germany). To validate the model historical precipitation data of the past ten years were performed. The validated model was further optimized using the extracted soil moisture from SAR data. The simulation results showed a reasonable match between the simulated and the observed hydrographs. Quantitatively the study concluded that based on SAR data, the model could be used as an expeditious tool of soil moisture mapping which required for hydrological modelling.

Table of Contents

List of Figures

List of Tables

Acronyms and Abbreviations

ADEOS	Advanced Earth Observing Satellite
ALOS	Advanced Land Observing Satellite
ALS	Airborne Laser Scanning
ASF	Alaska Satellite Facility
ATKIS	Authoritative Topographic-Cartographic Information System
BTLNK	Biotoptypen- und Landnutzungskartierung
AVNIR-2	Advanced Visible and Near Infrared Radiometer Type 2
Bkkonz	Bodenkonzeptkarten
CCRS	Canada Centre for Remote Sensing
CLISAX	Statistische Untersuchungen regionaler Klimatrends in Sachsen
CN	Curve Number
DEM	Digital Elevation Model
DLR	Deutsches Zentrum für Luft- und Raumfahrt
DSM	Digital Surface Model
DTM	Digital Terrain Model
DWD	German Weather Service
EOLi	Earth Observation Link
ESA	European Space Agency
ESRI	Environmental Systems Research Institute
FBD	Fine-Beam Double Polarisation
FEMA	Federal Emergency Management Agency
GeoSN	Staatsbetrieb Geobasisinformation und Vermessung Sachsen
GIS	Geographical Information System
HEC	Hydrologic Engineering Center
HMS	Hydrologic Modeling System
HSG	Hydrologic Soil Group
JAROS	Japan Resources Observation System Organization
JAXA	Japan Exploration Space Agency
JERS-1	Japanese Earth Resources Satellite-1
LDMS	Low-Dimensional Modelling System
LfULG	Sächsisches Landesamt für Umwelt, Landwirtschaft und Geologie
LTV	Landestalsperrenverwaltung des Freistaates Sachsen
NASA	National Aeronautics and Space Administration
NASDA	National Space Development Agency of Japan
PALSAR	Phased Array L-Band Synthetic Aperture Radar
PRISM	Panchromatic Remote-Sensing Instrument for Stereo Mapping
Radar	Radio Detection and Ranging
SAR	Synthetic Aperture Radar
SCS	Soil Conservation Services
SMC	Soil Moisture Content
SRTM	Shuttle Radar Topography Mission
TanDEM-X	TerraSAR-X Add-on for Digital Elevation Measurement
TDR	Time Domain Reflectometry
TSX	TerraSAR-X
USACE	US Army Corps of Engineers
WMS	Watershed Modelling System
DOP	Digital Ortho-Photo

ADEN	Data European Node
ENL	Equivalent Number of Looks
SMA	Soil-Moisture Accounting
RMSE	Root Mean Square Error
U	Theil's coefficient
S_i	Simulated runoff records
O_i	Observed runoff records

Symbol/ Parameter Definitions

S	potential maximum retention
P	rainfall depth
Q	runoff depth
L	watershed hydraulic length
W_s	average watershed slope
L_t	lag time
$f_\circ$	frequency
λ	wavelength
σ°	backscattering coefficient
h	vertical relief height
m_v	volumetric moisture content
R_s	surface roughness
S	soil-moisture sensitivity
σ_v	backscatter from vegetation
σ_s	backscatter from soil
L_c	attenuation caused by the vegetation canopy
DN	digital numbers
K_S	calibration coefficient
β°	radar brightness
θ_i	incidence angle
θ_{loc}	local incidence angle
GIM	Geocoded Incidence Angle Mask
NESZ	Noise Equivalent Sigma Zero
NEBN	Noise Equivalent Beta Naught
LS	Layover and Shadow
R^2	coefficient of determination
O	outlet flow
I	inflow
S	storage volume
X	dimensionless weighting factor
K	time constant or storage coefficient
Δt	time interval
γ_b	bulk density

Chapter 1: Introduction

In August 2002, heavy rainfall event occurred in Saxony/Germany; a violent flash flood and extreme high water levels happened in some tributaries of the River Elbe in the Ore Mountains. 21 people were killed, and massive parts of the infrastructure were destroyed immediately after the event. The total loss in Germany was estimated to be by about six billion Euro not including indirect losses of the private economic sector. Figure 1.1 shows examples of these damages. All these facts motivate hydrological flood modelling.

Hydrological modelling relies on the spatial characterization of the land surface concerning parameters relevant for runoff formation. However, land surface parameters which are required for these models are temporally highly variable, like soil moisture which plays an important role in the surface energy balance at the terrain-atmosphere interface and is considered a key state variable influencing the redistribution of the radiant energy and the runoff generation and percolation of water in soil.

Figure 1.1: Flooded Urban Areas in Pirna, Saxony, Germany during the 2002 Flood Event (www1).

Local measurements of soil moisture are strongly affected by spatial variability, besides being time-consuming and expensive. Soil moisture is a difficult parameter to measure in a large area, in a cost-effective way, and on a routine basis (Engman & Chauhan, 1995).

Remote sensing data and geo-information systems are increasingly becoming an important tool in hydrology and water resources development. This is due to the fact that most of the data required for hydrological analysis can easily be obtained from remotely sensed images. The greatest advantage of using remotely sensed data for hydrological modelling is its ability to generate information in spatial and temporal domain which is very crucial for successful model analysis, prediction and validation (Jagadeesha, 1999). In microwave remote sensing, the question how the microwaves interact with the earth terrain has always been interesting in interpreting satellite SAR imagery (Albert, 2005).

With advances in computational power and the growing availability of spatial data, it is possible to accurately describe watershed characteristics when determining runoff response to rainfall input (Arwa, 2001). Due to the development of geo information systems and remote sensing techniques the hydrological catchments models have been more physics-based and distributed to enumerate various interactive hydrological processes considering spatial heterogeneity (Mohan & Shrestha, 2000). SAR technology can be used to derive the soil moisture content corresponding to the degree of saturation in the near surface layer. Since microwave measurements of the soil surface are affected by the water content (Ulaby et al., 1986; Engman and Gurney, 1991, & Buchroithner and Granica 1997), it is easy to see the potential of remote sensing in soil moisture mapping and other related applications. Active microwave remote sensing to estimate spatial distribution of surface soil moisture has been demonstrated fully at the field scale (Bernard et al., 1986; Soares et al., 1987 & Brun et al., 1990), over areas characterized by fairly uniform attributes (land cover, topography, etc.).

Given the fact presence of dense and high vegetation cover prevents X- and C-band radar signals (wavelengths between 3 and 6 cm) from reaching the ground (Ulaby et al., 1986), soil moisture mapping is often carried out exclusively on bare soils or zones with little vegetation cover (e.g. Baghdadi et al., 2002, 2006, 2007; Le Hégarat et al., 2002; Zribi & Dechambre, 2002; Zribi et al., 2008). Furthermore, the increased number of SAR systems together with their good calibration performance has made SAR data more readily available for the quantitative retrieval of soil moisture. The big difference between the dielectric constant of water and of dry soil at microwave frequencies is the main factor for soil moisture estimation using microwaves. Whereas the dielectric constant for water is at least 10 times bigger than that of the dry soil, the presence of water in top few centimeters of bare soil can be detected in SAR imagery (Lillesand & Kiefer, 2008).

For the present study soil moisture represents an important parameter for hydrological modelling. The main objective of this work is the evaluation of the potential of spaceborne X & L-band SAR data for soil moisture retrieval and subsequently applying the extracted soil moisture as a required input parameter in hydrological modelling process.

The HEC-HMS model was applied to generate the rainfall runoff response of a river basin to precipitation representing the basin as an interconnected system of hydrologic and hydraulic components.

Finally, I would like to mention That the TerraSAR-X data were provided by the German Aerospace Center (DLR) under the Science proposal ID HYD0326 (Thomas Hahmann and Manfred F. Buchroithner) and the ALOS PALSAR data were acquired by the European Space Agency (ESA) under the Science proposal ID C1P6618.

1.2 Thesis Organisation

This thesis consists of six chapters. It is delineated as follows.

Chapter 1 addresses the necessity and the importance of the soil moisture in hydrological modelling and applying of spaceborne SAR data to derive the soil moisture content corresponding to the degree of saturation in the near surface layer. It gives a brief description of the problem and overall objectives.

Chapter 2 demonstrates a background of the microwave remote sensing and its application in Hydrology, its principles and limitations. It shows also, how GIS works as an efficient tool to link spatial data with hydrological models. Subsequently, flood hazard and the potential of hydrological flood modelling are introduced.

Chapter 3 outlines the boundaries of the study area and a full description of the data sources, instruments, softwares and the general layout of the implemented methodology.

Chapter 4 presents how the data were processed to achieve the purpose of this study. It also includes the results and their accuracy.

Chapter 5 provides a comprehensive discussion of the results of this research.

Chapter 6 draws conclusions and makes recommendations for future studies based on the obtained results.

Chapter 2: Literature Review

In the first part of this chapter Microwave Remote Sensing and its application in Hydrology, its principles and limitations are described. The second part of this chapter deals with the question how GIS as an efficient tool links spatial data with hydrological models. Subsequently flood hazard and the potential of hydrological flood modelling are introduced.

2.1 Microwave Remote Sensing and its Applications in Hydrology

2.1.1 Principles of Microwave Remote Sensing

Remote sensing has been defined as the science and art of obtaining information about an object, area, or phenomenon through the analysis of data acquired by sensors which are not in direct contact with the target of investigation. Airborne and satellite radar systems are adaptable imagery sources with day-night, all-weather capability. Radar imagery will likely increase in importance in the future as new multi-wavelength, multi-polarisation radar systems are disposed that allow interpreters to better discriminate between different surface materials. Microwave remote sensing uses electromagnetic waves with wavelengths between 1 mm and 1m (Figure 2.1). These relatively longer wavelengths have the advantage that they can penetrate clouds and are independent of atmospheric conditions, like haze. An imaging radar system emits discrete radar pulses that are directed to one side, so that each pulse illuminates a strip of terrain perpendicular to the flight path. The microwaves interact with surface objects and some portion of them return toward the radar antenna. The system records the pulse “echoes” from the terrain and their variation in strength with travel time. Since the microwaves travel at the speed of light in air, the timing of each portion of the returned signal establishes its image position in the range direction (perpendicular to the flight line). The image is built up from the returns of successive pulses as the aircraft or spacecraft moves forward in the azimuth direction, (radar image acquisition illustrated in Figure 2.2).

Microwave remote sensors can be classified as either passive (radiometers) or active (radars). Each sensor class provides unique insights into the electrical and mechanical properties of the sensed environment. Microwave remote sensing instruments provide a unique view which can augment traditional visible and infrared observations.

Passive microwave sensors rely on the thermal emission of microwave signals from objects and surfaces. The emission is related to the physical temperature and electrical and mechanical properties of the sensed surface, with modulation by the intervening atmosphere. Since they contain no transmitter, passive sensors typically require less power to operate than radars and operate over a much broader frequency range. On a global scale, passive measurements find utility in measuring surface and atmospheric temperatures, atmospheric water

vapor, precipitation, sea surface salinity, vegetation, and polar ice properties. Radio astronomy applies microwave radiometers in the study of the cosmos.

Active microwave remote sensors can be divided into four general classes: Synthetic Aperture Radar (SAR) imaging systems, scatterometers, altimeters, and weather radars. The latter systems typically use real-aperture antennas while SAR is based on synthetic aperture processing techniques. (Hybrid systems also exist.) Inverse synthetic aperture radar is used for ground-based sensing of extra-terrestrial bodies. SAR systems create high resolution radar backscatter images using Doppler/range processing. Scatterometers precisely measure radar backscatter at multiple azimuth angles at lower resolution than SARs. Spaceborne scatterometer data is used for wind measurement over the ocean and monitoring polar ice melting. Satellite-based altimeters measure sea surface height from which ocean current information is extracted. Weather radars measure rainfall, high altitude winds, and other meteorological phenomena. Active radar sensors can further be subdivided into non-imaging and imaging sensors. Important active non-imaging sensors are radar altimeters and scatterometers (Soergel, 2010).

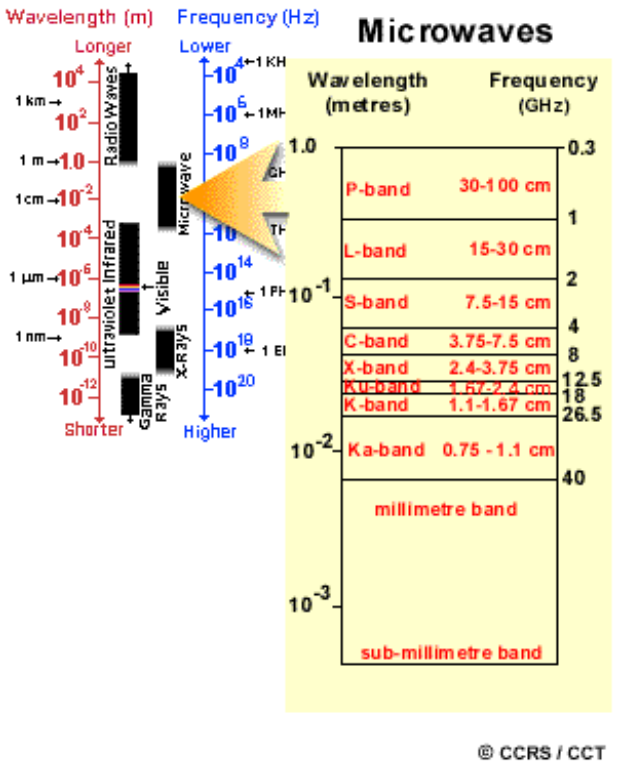

Figure 2.1: Microwave Electromagnetic Spectrum (from CCRS RS Tutorial).

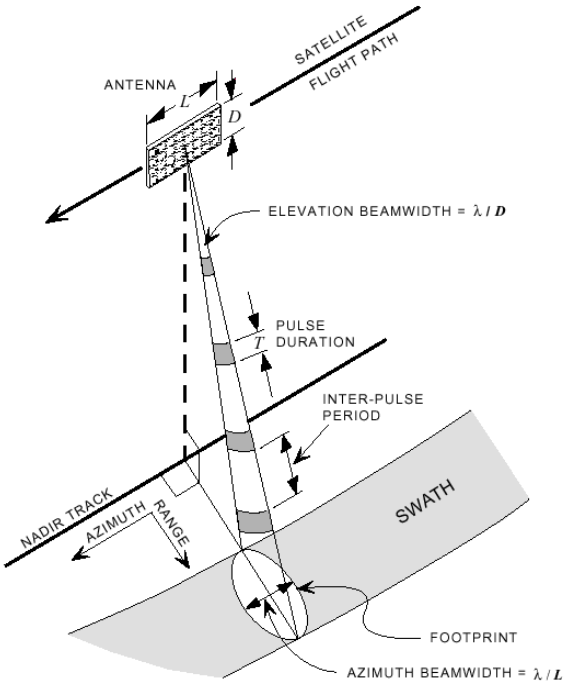

Figure 2.2: Radar Image Acquisition (from SAR-Guidebook, 2007).

2.1.1.1 Radar Polarisation and Scattering Type

Imaging radar systems typically transmit a plane-polarised radar pulse. The electric field associated with such a pulse oscillates in a single plane perpendicular to the direction the wave is traveling (Figure 2.3). The most common polarisation mode is to both transmit and receive horizontally polarised signals (designated HH mode, with the first letter indicating the transmitted polarisation) some systems transmit and receive vertically polarised waves (VV mode). Both HH and VV mode scan be called like-polarised radar modes. The cross-polarised (HV or VH) return is usually weaker, and often associated with different reflections due to, for instance, surface roughness. Thus, there can be four combinations of both transmit and receive polarisations as follows:

- HH for horizontal transmit and horizontal receive,
- VV for vertical transmit and vertical receive,
- HV for horizontal transmit and vertical receive, and
- VH for vertical transmit and horizontal receive.

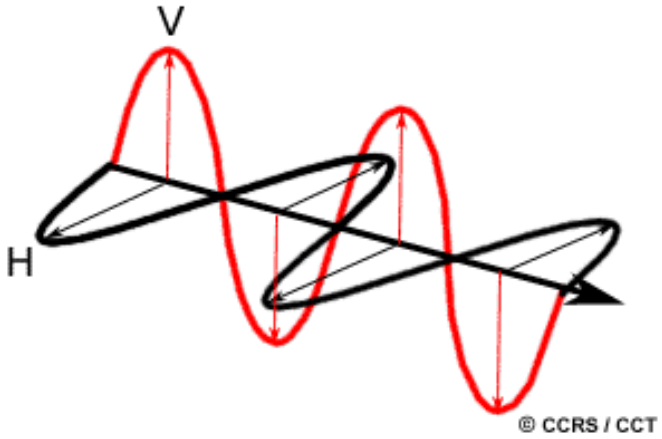

Figure 2.3: Radar Polarisation (from CCRS RS Tutorial).

2.1.2 Interpretation of Radar Images

The brightness of features in a radar image depends on the strength of the backscattered signal. In turn, the amount of energy that is backscattered depends on various factors, including the orientation of the surface, its roughness and electrical properties, and the polarisation direction of the returning radar wave. Areas with stronger radar returns are shown as brighter areas. Because of the side-looking geometry of imaging radar systems only a small portion of the broadcast energy returns back in the direction of the antenna and is detected by it.

2.1.2.1 Microwave Signal and Object Interactions

The amount of energy that is received at the radar antenna depends on the illuminating signal (radar system parameters such as wavelength, polarisation, viewing geometry, et cetera) and the characteristics of the illuminated object (roughness, shape, orientation, dielectric constant, etc.)

Influence of the Illuminating Signal

To a certain degree, penetration is the key factor for the selection of the wavelength: the longer the wavelength (the smaller the frequency), the stronger the penetration into vegetation and soil; the wavelength determines the size of the objects that the waves interact with. For example, a short microwave will only penetrate the leaves on top of the trees (e.g., X-band = 3 cm) whereas in

the case of L-band (23 cm), the radiation penetrates into the canopy. Table 2.1 gives an overview of all the codes with their corresponding parameters.

The polarisation of the microwave plays an important role in the interpretation of the form and the orientation of small scattering elements that compose the surface object. Therefore, the use of microwaves with different polarisations yields different images that might help in the identification of objects.

Table 2.1: Radar Bands and their Parameters and Operational Use.

Band	Frequency $f_\circ$ (GHz)	Wavelength Range $\lambda = c / f_\circ$ (cm)	Application
P	0.3 - 1	30 - 100	AIRSAR
L	1 - 2	15 - 30	JERS-1 SAR, ALOS PALSAR
S	2 - 4	7.5 - 15	Almaz-1
C	4 – 8	3.8 - 7.5	ERS-1/2 SAR, RADARSAT-1/2, ENVISAT ASAR, RISAT-1
X	8 – 12	2.4 - 3.8	TerraSAR-X-1, COSMO-SkyMed
Ku	12 - 18	1.7 - 2.4	satellite altimetry
K	18 - 27	1.1 – 1.7	military domain
Ka	27 – 40	0.8 - 1.1	surveillance

Influence of the Illuminated Surface

An absolute measure for the backscatter behavior of an object-similar to reflectance in optical systems-is calculated from the ratio of the emitted and received signal, taking into account the range to the object. This is called the radar cross section sigma (σ) expressed in decibels (db). The amount of energy backscattered from an object depends on its characteristics such as surface roughness, moisture content (electrical properties of the object), its orientation with respect to the illuminating signal (local incidence angle) and its shape. Apart from the relief, the surface roughness is the terrain property that most strongly influences the strength of the radar return. It is a relative aspect, depending upon wavelength and incidence angle. A surface is considered ‘rough’ if it has height variations of dimensions that are close to the radar

wavelength. In radar images, rough surfaces appear bright, smooth surfaces appear dark. This is a result of the scattering behaviour of radar waves.

Short-wavelength radar signals (X and C bands) interact primarily with the uppermost leaf canopy, and do not penetrate beyond it. Longer-wavelength radars (L and P bands) penetrate deeper to interact with stems of smaller plants and twigs and branches of trees. Another important parameter that influences the microwave backscatter behavior is the dielectric constant, which describes the electrical properties of the surface material. The moisture content of the object affects the electrical properties and therefore the dielectric constant. Depending on the moisture content of the object, the radar is scattered in different ways.

2.1.2.2 Scattering Patterns

The radar is scattered in different ways depending on the above/mentioned characteristics of the signal and object. The amount of backscattered microwave energy depends, in part, on the surface or target properties, such as surface roughness and moisture (Buchroithner & Granica 1997). Changes in the electrical properties influence the absorption, transmission and reflection of microwaves. This means that the moisture content of the surface determines the scattering. If an object is wet, surface scattering takes place. The type of reflection (ranging from specular to diffuse) and its intensity depends on the roughness of the material (Figure 2.4). Generally, reflectivity and therefore image brightness increases with increasing moisture content. Consequently, *soil moisture maps* can be derived from radar backscatter.

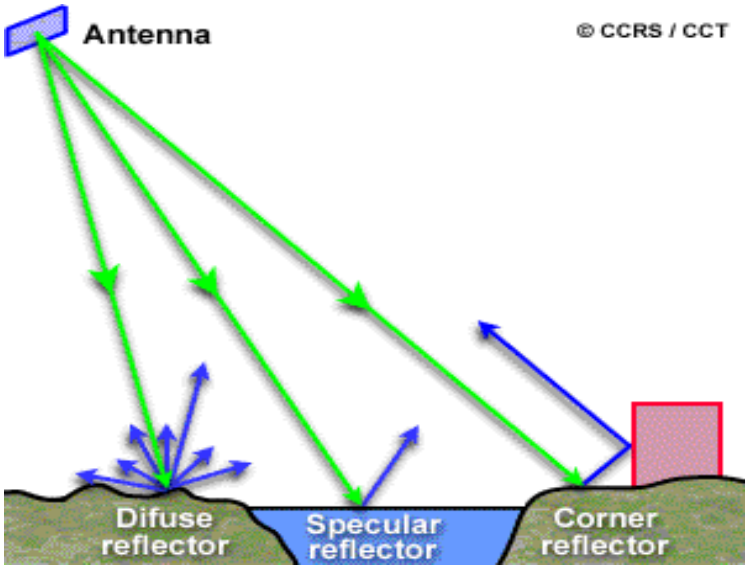

Figure 2.4: Radar Reflection from Various Surfaces (from CCRS RS Tutorial).

2.1.3 Geometrical Characteristics

Large-scale variations in the surface (for example, terrain slopes), affect the backscattering properties. In a radar image, broadly four geometrical characteristics are observed, namely, (i) slope foreshortening, (ii) aspect, (iii) radar shadow, and (iv) layover.

2.1.3.1 Slope Foreshortening

For similar terrain slopes, or for the same slope recorded at different depression angles, there is a variation in the slope length on the radar image. Slopes are often made to appear shorter than they really are, that is, they are foreshortened. Foreshortening is at a maximum for a slope when the incident angle (θ_i) is equal to zero, where the slopes are recorded in true proportion to their length. Figure 2.5 shows this effect. A slope is recorded at its true length if it slopes away from the radar antenna at an angle at which it is truncated in its slant range presentation. For slope 1 in Figure 2.5, which faces the radar and has a gradient equal to the depression angle, both the top and the base of the slope are intercepted simultaneously by the radar beam wavefront, and so are recorded as a single point on the image. Foreshortening thus occurs when a slope is less steep than when perpendicular to the wavefront, with the base of the slope intercepting the wavefront first (Lillesand and Kiefer, 1979), as shown for slope 2 in Figure. 2.5.

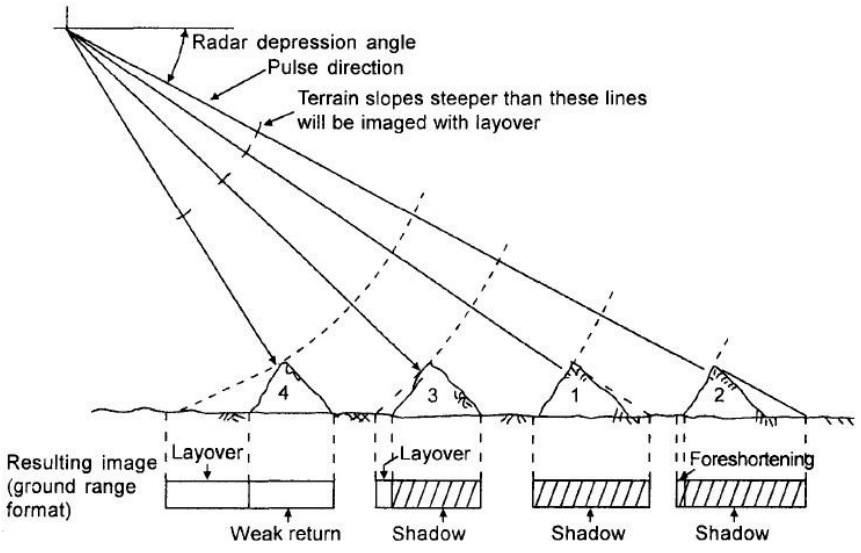

Figure 2.5: Influence of Terrain Slope on Radar Imagery (Lillesand & Kiefer 1979).

2.1.3.2 Aspect

Aspect is important since, if a slope is orientated away from the flight line, then the wave front's journey from the base of the slope to its top is further increased, and hence the amount of energy per unit area is reduced. This can greatly affect the backscatter recorded and so the interpretability of the imagery. Slope orientation relative to the radar look direction is therefore important.

2.1.3.3 Radar Shadow

The other important characteristic of radar imagery is the radar shadow, which occurs whenever the terrain backslope is steeper than the depression angle. This is due to the absence of radar illumination because of intervening reflecting or absorbing objects, for example terrain obstructions (mountains, cliffs) or by artificial features (buildings) within the illuminating radar beam. The length of the radar shadow is determined by the wavefront angle, as are layover and foreshortening. Areas of radar shadow are generally more common in the far range, because in the near range fewer backslopes are steep enough to be obscured from the radar beam.

2.1.3.4 Layover

If, however, the terrain slope is steeper than a line perpendicular to the incident wavefront, so that its top intercepts the radar beam wavefront before the base of the slope, then layover occurs. This is illustrated in Figure 2.5 for slopes 3 and 4. It was shown that foreshortening occurs when a slope facing the radar is not as steep as the wavefront. With layover, however, a slope facing the radar appears to be steeper than it really is, as its slope is steeper than that of the wavefront. From the above discussion of layover and foreshortening, and the fact that the depression angle varies across the image swath, it can be seen that similar terrain slopes at different positions from the flight line will be recorded differently. Layover is most likely to occur in the near range where the depression angle is large. Layover and foreshortening are important factors, and should be considered while interpreting radar imagery. This is not only because of the distortion they introduce into the image but also because the amount of energy received per unit area varies with the angle at which the energy is received and so with the slope. The angle at which the energy is received at the surface is critical to the distribution of the energy backscatter from that surface. For flat terrain the angle at which the energy arrives varies across the swath, and further complexity is introduced by variations in the surface slope.

2.1.4 Spaceborne Radar Systems

2.1.4.1 Historical Account

This section is based on: A Canada Centre for Remote Sensing (CCRS), Remote Sensing Tutorial "Fundamentals of Remote Sensing'' and from the book "Observation of the earth and its environment" by Herbert Kramer, 2002.

With the advances and success of airborne imaging radar, satellite radars were the next logical step to complement the optical satellite sensors in operation. SEASAT, launched in 1978, was the first civilian remote sensing satellite to carry a spaceborne SAR sensor. The SAR operated at L-band (23.5 cm) with HH polarisation. The viewing geometry was fixed between nine and 15 degrees with a swath width of 100 km and a spatial resolution of 25 meters. This steep viewing geometry was designed primarily for observations of ocean and sea ice, but a great deal of imagery was also collected over land areas. However, the small incidence angles amplified foreshortening and layover effects over terrain with high relief, limiting its utility in these areas. Although the satellite was only operational for three months, it demonstrated the wealth of information (and the large volumes of data) possible from a spaceborne radar.

With the success of the short-lived SEASAT mission and impetus provided from positive results with several airborne SARs the European Space Agency (ESA) launched ERS-1 in July of 1991. ERS-1 carried on-board a radar altimeter, an infrared radiometer and microwave sounder, and a C-band (5.66 cm) active microwave instrument. This is a flexible instrument which can be operated as a scatterometer to measure reflectivity of the ocean surface, as well as ocean surface wind speed and direction. It can also operate as synthetic aperture radar, collecting imagery over a 100 km swath with an incidence angle range of 20 to 26 degrees and a resolution of approximately 30 meters. Polarisation is vertical transmit and vertical receive (VV) which, combined with the fairly steep viewing angles, make ERS-1 particularly sensitive to surface roughness. The revisit period (or repeat cycle) of ERS-1 can be varied by adjusting the orbit, and ranged from three to 168 days, depending on the mode of operation. Generally, the repeat cycle is about 35 days. A second satellite, ERS-2, was launched in April of 1995 and carries the same active microwave sensor as ERS-1. Designed primarily for ocean monitoring applications and research, ERS-1 provided the worldwide remote sensing community with the first wide-spread access to spaceborne SAR data. Imagery from both satellites has been used in a wide range of applications over both ocean and land. Like with SEASAT, the steep viewing angles limit their utility for some land applications due to geometry effects.

In February 1992, the National Space Development Agency of Japan (NASDA) launched the JERS-1. In addition to carrying two optical sensors, JERS- 1 has an L-band (23.5 cm) SAR operating at HH polarisation. The swath width is approximately 75 km and the spatial resolution approximately 18 meters in both range and azimuth. The imaging geometry of JERS-1 is slightly shallower than either SEASAT that of the ERS satellites, with the incidence angle at the middle

of the swath being 35 degrees. Thus, JERS-1 images are slightly less susceptible to geometry and terrain effects. The longer L-band wavelength of JERS-1 allows some penetration of the radar energy through vegetation and other surface types.

Canada started their radar satellite program in 1995 with Radarsat-1. Radarsat-2 followed in 2007, with both satellites operating in C-Band. Radarsat-1 was the first satellite worldwide capable of acquiring images in ScanSAR mode with a swath width of 500 km. It can also operate in numerous beam modes that allow a wide variety of swath widths, incidence angles and image resolution. Radarsat-2 is a further development of the Radarsat-1 mission. It can operate in a fully polarimetric mode. As it can even acquire images on both sides of the satellite track, the satellite can map Antarctica on a daily basis; which is of great interest for scientific research activities. In February 2000 the Shuttle Radar Topography Mission (SRTM), which lasted for eleven days, was launched by NASA. It was acquired radar images in the C- and X-Band. Like for the SIR-C mission the X-Band radar was provided by Germany and Italy. A special feature was that the shuttle was equipped with two antennas, thus a single-pass interferometry had been made possible. As a result a DEM covering the world from 56° southern to 60° northern latitude could be generated. In 2006 Japan launched the ALOS satellite carrying the PALSAR instrument which is an improvement of the SAR on board JERS-1.

Since Germany had gathered considerable experience in X-Band radar, it developed the TerraSAR-X satellite which was launched in 2007. Together with a twin satellite which operates since June 2010, these satellites will operate in tandem mode under the mission name ''TanDEM-X'' to acquire images for a global DEM of an unprecedented quality. A short introduction to the history of spaceborne radar systems is summarised in Table 2.2.

Table 2.2: Overview of Spaceborne SAR-Missions.

System	Institution / Country	Launch	Band	Pol.	Look angle	Swath width (km)	Resolution (m)
SEASA	NASA/USA	1978	L	HH	20˚	100	25
ALMAZ-1	NPO/Russia	1991	S	HH	25°- 60°	40	13 - 20
ERS-1	ESA/Europe	1991	C	VV	23°	100	30
J-ERS-1	NASDA/Japan	1992	L	HH	35˚	75	18
SIR-C/ X-SAR	NASA-JPL/USA DLR/Germany ASI/Italy	1994	L C X	Quad Quad VV	20°-55°	30-100	15 - 25
ERS-2	ESA/Europe	1991	C	VV	23°	100	30
Radarsat-1	CSA/Canada	1995	C	HH	20°- 55˚	10-500	10 -100
SRTM	NASA-JPL/USA DLR/Germany ASI/Italy	2000	C X	VV+HH VV	17°- 65° 55°	225 50	30 30
ENVISAT	ESA/Europe	2002	C	Quad	15°- 45˚	100 400 400	30 150 1000
ALOS	JAXA/Japan	2006	L	Quad	8°- 60°	20-350	7-100
TerraSAR-X	DLR/Germany	2007	X	Quad	20°- 60˚	10-100	1 -17.6
Radarsat-2	CSA/Canada	2007	C	Quad	10°- 60°	20-500	3 -100
TanDEM-X	DLR/Germany	2010	X	Quad	20°- 60˚	10-100	1 -17.6

Since TerraSAR-X and ALOS PALSAR Satellite data are used in this thesis, they will be described in more detail.

2.1.4.2 TerraSAR-X

TerraSAR-X is the first satellite in Germany that has been implemented in a public-private partnership between the German Aerospace Center (DLR) and EADS Astrium. The satellite was launched on 15 June 2007 from Baikonour, Kazakhstan, with a DNEPR-1 rocket and has been designed for five years of operation. The satellite travels in a sun-synchronous circular orbit at an altitude above the equator of 514 km, a repeat cycle of 11 days and an inclination of 97.44°. The maximum duration of image acquisition is limited to approximately ten minutes per orbit, whereas the duration of one orbit is 95 min. The spacecraft has a hexagonal outer shape and a mass of 1200 kg. With this satellite it is possible to perform a roll manoeuvre. Therefore it can acquire images to both sides of the satellite track.

The SAR sensor operates in X-Band with a frequency around 9.65 GHz. This corresponds to a wavelength of 3 cm. It is capable of transmitting and receiving

in horizontal and vertical like-polarisation. The SAR antenna has a dimension of 4.8 x 0.8 m², and it is an active phase array antenna that consists of 12 panels. Each of these panels is equipped with 32 slotted waveguide subarrays that contain a transmit and receive module. The radar beam is steerable in elevation by 0.75° and in azimuth from 20° to 60°. With the help of these different view angles, each point on earth can be targeted within two to four days. The antenna allows also the operation of different acquisition modes: Spotlight, StripMap and ScanSAR are distinguished by their resolution and the size of the area they cover. The characteristics of these acquisition modes are illustrated in Figure 2.6 and listed in Table 2.3.

The antenna can also work in a dual receive mode. It can then be split into two halves that can both receive the echo. This mode facilitates along track interferometry and the acquisition of full polarimetric data.

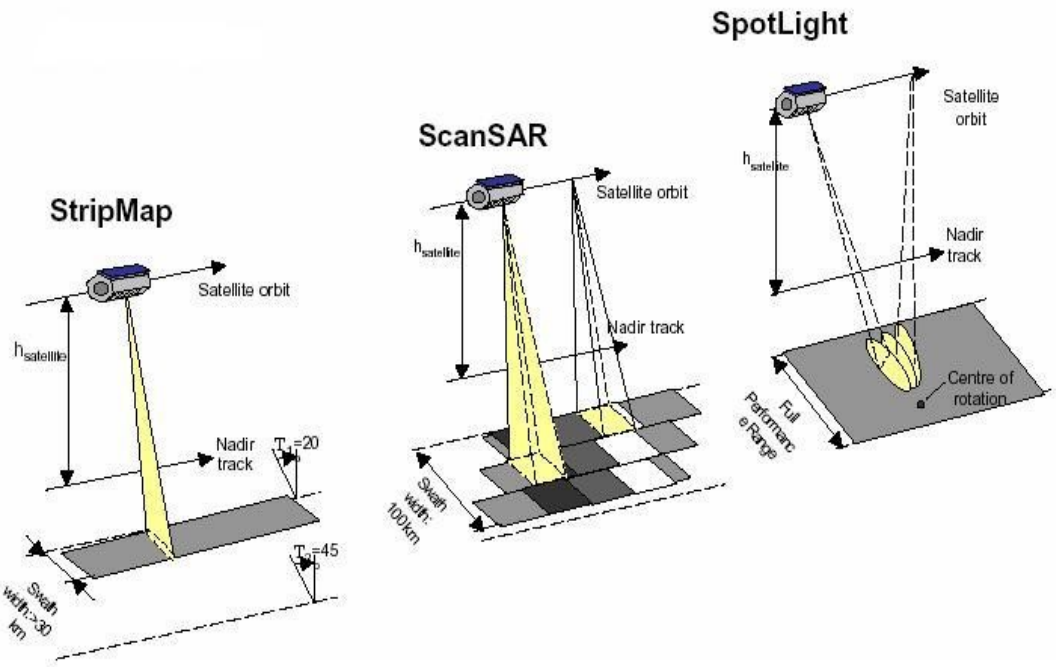

Figure 2.6: Scanning Modes of TerraSAR-X (from SAR-Guidebook, 2007).

Table 2.3: SAR Mode Performance (Pitz, 2006).

	ScanSAR Mode	StripMap Mode	High Resolution Spotlight Mode
Ground Resolution - Across Track	16m	3m	1m
- Along Track	16m	3m	1m
Product Coverage - Along Track	<1500km	<1500km	5km
- Across Track	100km	30km	10km

2.1.4.3 ALOS

ALOS Characteristics

In January 2006 the Advanced Land Observing Satellite (ALOS) was launched on an H-IIA launch vehicle from Tanegashima Space Center, Japan. The Japanese earth observing satellite program consists of two series: those satellites used mainly for atmospheric and marine observation, and those for land observation. ALOS follows the Japanese Earth Resources Satellite-1 (JERS-1) and the Advanced Earth Observing Satellite (ADEOS) and utilizes advanced land-observing technology. ALOS will be used for cartography, regional observation, disaster monitoring, and resource surveying.

ALOS has three remote-sensing instruments: the Panchromatic Remote-Sensing Instrument for Stereo Mapping (PRISM) for digital elevation mapping, the Advanced Visible and Near Infrared Radiometer Type 2 (AVNIR-2) for precise land coverage observation, and the Phased Array L-band Synthetic Aperture Radar (PALSAR) for day-and-night and all-weather land observation. In order to fully utilize the data obtained by these sensors, ALOS was designed with two advanced technologies: first, a high-speed and large-capacity mission data handling technology and second, a precision spacecraft position and attitude determination capability. Both will be essential to high-resolution remote sensing satellites of the next decade.

ALOS PALSAR

The Phased Array type L-band Synthetic Aperture Radar (PALSAR) is an active microwave sensor using L-band frequency to achieve cloud-free and day-and-night land observation. It provides higher performance than the JERS-1's SAR. Fine resolution in a conventional mode, but PALSAR will have another advantageous observation mode. ScanSAR, which will enable us to acquire a 250 to 350 km width of SAR images (depending on the number of scans) at the expense of spatial resolution (Figure 2.7 and Table 2.4). This swath is three to

five times wider than conventional SAR images. The development of the PALSAR is a joint project between JAXA and the Japan Resources Observation System Organization (JAROS).

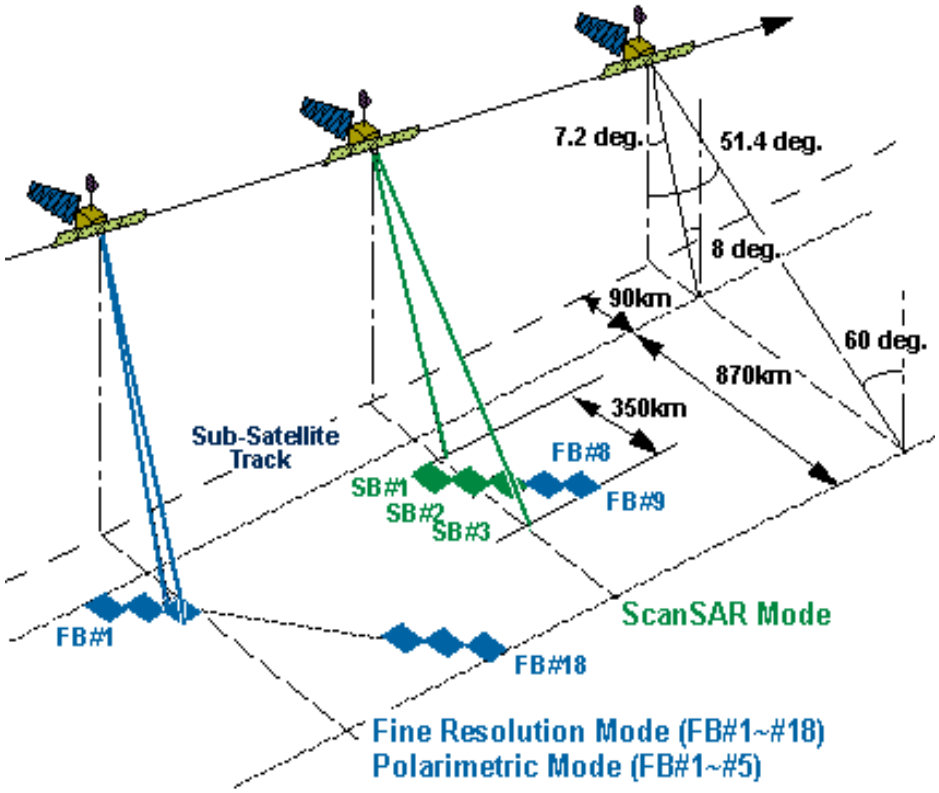

Figure 2.7: PALSAR Observation Mode (from ALOS User Handbook, 2007).

Table 2.4: PALSAR Characteristics (from ALOS User Handbook, 2007).

Mode	**Fine**		**ScanSAR**	**Polarimetric (Experimental mode)*[1]**
Center frequency	1270 MHz(L-band)			
Chirp bandwidth	28 MHz	14 MHz	14 MHz, 28 MHz	14 MHz
Polarisation	HH or VV	HH+HV or VV+VH	HH or VV	HH+HV+VH+VV
Incident angle	8 to 60 deg.		18 to 43 deg.	8 to 30 deg.
Range resolution	7 to 44 m	14 to 88 m	100m (multi look)	24 to 89 m
Observation swath	40 to 70 km		250 to 350 km	20 to 65 km
Bit length	5 bits			3 or 5 bits
Data rate	rate 240 Mbps		20Mbps,240Mbps	240 Mbps
NE sigma zero *[2]	< -23 dB (Swath Width 70 km) < -25 dB (Swath Width 60 km)		< -25 dB	< -29 dB
S/A *[2],*[3]	> 16 dB (Swath Width 70 km) > 21dB (Swath Width 60 km)		> 21dB	> 19 dB
Radiometric accuracy	scene: 1 dB / orbit: 1.5 dB			

PALSAR cannot observe areas beyond 87.8 deg. north latitude and 75.9 deg. south latitude when the off-nadir angle is 41.5 deg.

*1 Due to power consumption, the operation time will be limited.
*2 Valid for off-nadir angle 34.3 deg. (Fine mode), 34.1 deg. (ScanSAR mode), 21.5 deg. (Polarimetric mode).
*3 S/A level may deteriorate due to engineering changes in PALSAR.

2.1.5 Remote Sensing in Hydrological Modelling

Remote sensing plays an important role in hydrological modelling, especially at regional scale or watershed scale, and the hydrological cycle components may involve precipitation, evapotranspiration, soil moisture, surface water as well as groundwater. Remote sensing can provide earth surface information over large areas and long periods at different scales, and the derived data can be used as input data for the hydrological models.

For hydrological modelling, time series of runoff and possibly precipitation, as well as a climatological estimate of monthly evapotranspiration are very important, these parameters may be obtained by station-based observation systems. The model development based on surface stations almost impossible for a large river basin is due to the scarcity of land surface observations and difficulties in representing hydrological processes at larger scales. Remote sensing may provide the required data, such as information on land surface/cover, soil texture, initial soil moisture and topography, for hydrological modelling at regional to global scales. For modelling land-atmospheric hydrological interactions, remote sensing provides both model parameters and meteorological data, like surface air temperature, humidity, precipitation and radiation.

Liu and Zhang (2004) gave a review of application of remote sensing to retrieval of precipitation, land use/ cover classification, leaf area index, albedo, land surface heat flux and some indirect parameters in distributed hydrological models, and proposed a framework for developing a distributed hydrological model by integrating GIS and remote sensing. Wu and Liu (2002) considered that the data obtained from remote sensing is still hard to use in hydrological model directly, and the hydrological scale problem is the crucial aspect for hydrological modelling using remote sensing. Li et al. (2005) developed a physics-based distributed hydrological model to simulate the watershed runoff response process under climate and land-cover changes in the head area of the Yellow River by using remote sensing and GIS. Liu et al. (2004) developed a distributed hydrological model for the Yellow River Basin, which represents a part of National Key Project “Yellow River Water Resources Evolution Law and Renewability Maintaining Mechanism”. The area precipitation data obtained from meteorology satellite imagery was treated as an input for the model.

2.1.5.1 Precipitation

Precipitation is of primary importance in hydrology. It shows large and frequent spatial and rapid temporal variations. The scales over which precipitation occurs are so large that methods of measurement are wide- ranging and usually complementary. Point measurements are insufficiently representative for catchment scales. So remote sensing becomes a very powerful tool for obtaining the precipitation information for water cycle research. Currently, the emphases are put on the application of ground-based or space-borne radar as

well as passive microwave data. The approaches based on visible and infrared satellite data were also developed.

Two basic approaches namely the “life-history” and the “cloud-indexing” are widely used. Wang J.H. (2003) developed the area precipitation model according to the regression relationship between cloud and point precipitation by using GMS image and surface rain gage. In the Yellow River Basin, the model prediction precision reached to 90%. Huang, (2006) developed the Flood-Causing Torrential Rain Forecasting and Warning System for Huaihe River. Rainfall was estimated by using satellite and radar data. Furthermore, form GMS-5 multi-channel data, the empirical formula of rainfall measurement was developed using a statistic approach in the Huaihe River catchment. The model was tested and verified during the application of flood season 2003.

2.1.5.2 Evapotranspiration

Evapotranspiration includes water that evaporates from the soil surface and water that is transpired from vegetation. It plays an important role in earth-atmosphere interaction process, and has attracted a rather considerable amount of attention and research work. Transpiration rates are largely controlled by: radiant energy, temperature, humidity, soil moisture, land cover physiography, and topography (Buttle, et al., 2000 & Hetherington, 1987). The net absorbed energy used for evapotranspiration goes into transpiration of soil water and evaporation from wet vegetation. The remaining energy goes into evaporation from the ground and water (Hetherington, 1987).

The researches are related to the use of thermal infrared observations and the land surface heat balance as well as to the spectrum of multi-spectral measurements by space- and airborne instruments to estimate potential evaporation and crop water requirements for the purpose of water management especially in irrigation regions. Wang (2003), Guo (2004) and Sun (2005) et al. gave a review of advances in the monitoring approaches of evapotranspiration with remote sensing data and its application in water resources management. Sun (2005) et al. developed the SEBAL model by using spectral radiances recorded by satellite-based sensors plus ordinary meteorological data to solve the energy balance at the earth surface, and to evaluate evapotranspiration in the Haihe River Basin. Hu (2006) considered ET technique of remote sensing monitoring to realize the sustainable management of agricultural water supply in Beijing. Pang et al. (2004) developed the evapotranspiration estimation model based on energy balance by using remote sensing. Their approaches were demonstrated in the province of Heilongjiang.

2.1.5.3 Soil Moisture

Soil moisture can be considered as an interface between the solid earth surface and the atmosphere, and is very important to understand the hydrological cycle process in both smaller and larger scales. However, soil moisture is a very difficult variable to measure, not at a point in time but on a consistent and spatially comprehensive basis. Surface soil moisture is an important and very dynamic state variable of the hydrological cycle. The knowledge of its magnitude and dynamics is crucial for studying and modelling important processes on the earth surface. Therefore, the estimation of soil moisture by means of remotely sensed observations is very attractive to domains like hydrology, agronomy or meteorology (Engman, 1991).

In recent years, many researchers have demonstrated the potential of microwave remote sensing for the estimation of surface roughness and soil moisture (e.g. Baghdadi et al., 2002, 2006, 2007; Le Hégarat et al., 2002; Satalino et al., 2002; Zribi and Dechambre 2002; Oh, 2004; Alvarez et al., 2005; Mattia et al., 2006; Rahman et al., 2008 & Zribi et al., 2008). Whereas, the SAR technique is very sensitive to soil surface conditions, especially roughness and moisture content in the first few centimeters of soil (Bruckler et al., 1988). Soil moisture mapping is often carried out exclusively on bare soils or zones with little vegetation cover (e.g. Baghdadi et al., 2002, 2006, 2007; LeHégarat et al., 2002; Zribi and Dechambre 2002 & Zribi et al., 2008).

The successful measurement of soil moisture by remote sensing depends on the amount of reflected or emitted electromagnetic radiation, and only the microwave region of the spectrum can provide a quantitative approach to estimate soil moisture under a variety of topographic and vegetation cover conditions (Engman, 2000). Most reviews suggest that surface soil moisture could be retrieved with sufficient accuracy from a system providing two or more polarisations of a single frequency such as L-band SAR (e.g. Ulaby et al., 1982, 1996). Several studies suggested that the accuracy of SAR-based volumetric soil moisture content estimates could be improved by combining data from optical sensors (e.g. surface reflectance and temperature) to discriminate the SAR signal response to vegetation (Moran et al., 1997).

Zhang and Sha (2005) & Zhang (2006) summarised the theories and methods of soil moisture monitoring by remote sensing, including microwave remote sensing monitoring, thermal inertia, the composite index of crop vegetation and brightness index, as well as thermal infrared monitoring. Bao et al. (2006) discussed the estimation approaches of soil water content and wheat coverage with ASAR imagery. The authors concluded that backscattering, which was greatly affected by land surface roughness and soil texture, is a key problem which must be considered in the retrieval of soil water content. The vertical polarisation backscattering coefficient is significantly correlated to the soil water content while the horizontal polarisation backscattering coefficient is significantly correlated to both soil water content and wheat cover. Moran (2000) evaluated the soil moisture using multi-temporal SAR in semiarid rangeland, the correction for surface roughness conditions resulted in a

substantial improvement in the correlation between the SAR signal and the surface soil moisture. Many semi-empirical and physical models have been developed for the estimation of soil moisture and surface roughness from SAR data (e.g. Fung, 1994; Dubois et al., 1995 & Weimann et al., 1998).

2.1.5.4 Surface Water

Surface water may occur in the form of lakes, reservoirs, rivers as well as snow and ice. Remote sensing can be used to estimate the areal extent and water content of these surface water-bodies, as well as the changes in water regimes. One of the main obscurations to remote sensing application is the limitation of relatively cloud-free and daylight conditions. Microwave satellites offer the potential of all-weather application and the synergistic application of combined SAR; also optical remote sensing for surface water estimates needs to be examined more closely. Yang et al. (2003) presented a method for analyzing the surface water system in plain areas with the help of GIS, DEM and remote sensing. Hong et al. (2006) utilized the various sources of remote sensing images combined with DEM and DSM data to analyse the characteristics of surface water system including springs, lakes, water resources of head regions in Tsinghai and on the Tibet plateau. Wang & Zhang (2005) developed a momentum BP neural network model to retrieve the water depth information for the South Channel of the Yangtze River Estuary using the relationship between reflectance derived from Landsat ETM+ satellite data and water depth.

2.1.5.5 Groundwater

Groundwater is essentially a subsurface phenomenon, so the common current remote sensing, mainly recording features on the surface, can only provide information to indirectly help qualitative or semi-quantitative analysis of groundwater systems with a simple geological condition and shallow groundwater table. Remote sensing data provide accurate spatial information and can be economically utilized over conventional techniques of groundwater studies. Remote sensing and GIS techniques have emerged as handy, complementary tools in assessing, monitoring and conserving ground water resources, owing to spatial, spectral and temporal data availability and data integration capability (Sener et al., 2005). Blending the two techniques has proved to be an efficient tool in groundwater studies (Gustafsson, 1993; Saraf and Jain, 1994; Krishnamurthy and Srinivas, 1995 and Krishnamurthy et al., 1996). Abduwasit & Qin (2004) presented a review of the development and progress of remote sensing application research on groundwater exploration, as well as the methods of regional groundwater monitoring, delineation and detection. Tashpolat et al. (2005) developed a quantitative model for deriving the groundwater level in oasis-desert ectones in arid areas using LandSat-7 ETM+ data.

2.1.5.6 Infiltration

Infiltration is commonly defined as the process of water entry at the land surface into soil from a source such as rainfall or snowmelt (ASCE, 1996). It is an important component of the boreal forest water balance dynamics because it dictates the amount of rainfall excess that is generated versus the water entering the groundwater system. Infiltration is a complex process that is affected by a number of factors such as soil characteristics, surface characteristics, and natural processes like rainfall intensity, freezing, and soil moisture. The near surface portion of the forest soils contain a high degree of macropores, pore spaces that are much larger than those of the soil matrix, created by long root densities and faunal activity. Preferential flow in the macropores can cause infiltrating water to reach depths much quicker than water traveling through macropores (Buttle et al., 2000). The hydraulic conductivity of the upper soil layer in a muskeg environment reduces exponentially with depth (Radforth and Brawner, 1977; Nyberg et al., 2001 and Metcalf & Buttle, 2001). Metcalfe & Buttle (2001) measured the saturated hydraulic conductivity at the BOREAS NSA in northern Manitoba. Peng et al. (2008) explained how to predict the soil erosion process based on the remote sensing and GIS modelling technique. Their model calculates the soil process by incorporating the parameters concerned, such as rock infiltration. The results indicate that RS and GIS techniques are indeed valuable tools for predicting soil erosion processes.

2.2 Integration of GIS with Hydrological Modelling

2.2.1 General

Hydrology and GIS are two technologies that, in different ways have tried to solve some of the same kinds of problems. As the synergy of these two technologies was realized, many successful attempts were made at integrating them

For almost two decades in the 1960s and 1970s, GIS and hydrological modelling developed in parallel with few interactions. Major research efforts toward the integration of GIS with hydrological modelling did not take place until the late 1980s, as a part of the GIS community's efforts to improve the analytical capabilities of GIS (Fotheringham and Rogerson, 1994 & Goodchild, et al., 1992) and hydrologists' new demand for accurate digital repre- sentations of the terrain (Singh and Fiorentino, 1996 & Clark, 1998).

The use of GIS as a management and data integration tool has grown since the late 20th century. Figure 2.8 illustrates the linking of information in different forms through a GIS. GIS technology has eased previously laborious procedures. Exchange of data between GIS, CAD, supervisory control and data acquisition (SCADA), and hydrologic and hydraulic (H&H) models is becoming much simpler. For example, delineating watersheds and stream networks has been simplified and the difficulty of conducting spatial data management and model parameterization reduced (Miller et al., 2004).

Nowadays, both GIS users and hydrologists have increasingly recognized the mutual benefits of such integration from the successes of the past ten years. Various hydrological modelling techniques have enabled GIS users to go beyond the data inventory and management stage to conduct sophisticated modelling and simulation. For hydrological modelling efforts, GIS, especially through their powerful capabilities to process Digital Terrain Model (DTM) data, have provided modellers with new platforms for data management and visualization.

The rapid diffusion of GIS in society has the potential to make various hydrological models more transparent and enable the communication of their operations and results to a large group of users. The growing literature on the integration of GIS with hydrological modelling attests the recognition of such mutual benefits (DeVantier and Feldman, 1993; Maidment, 1993, 1996; McDonnell, 1996 & Moore, 1996).

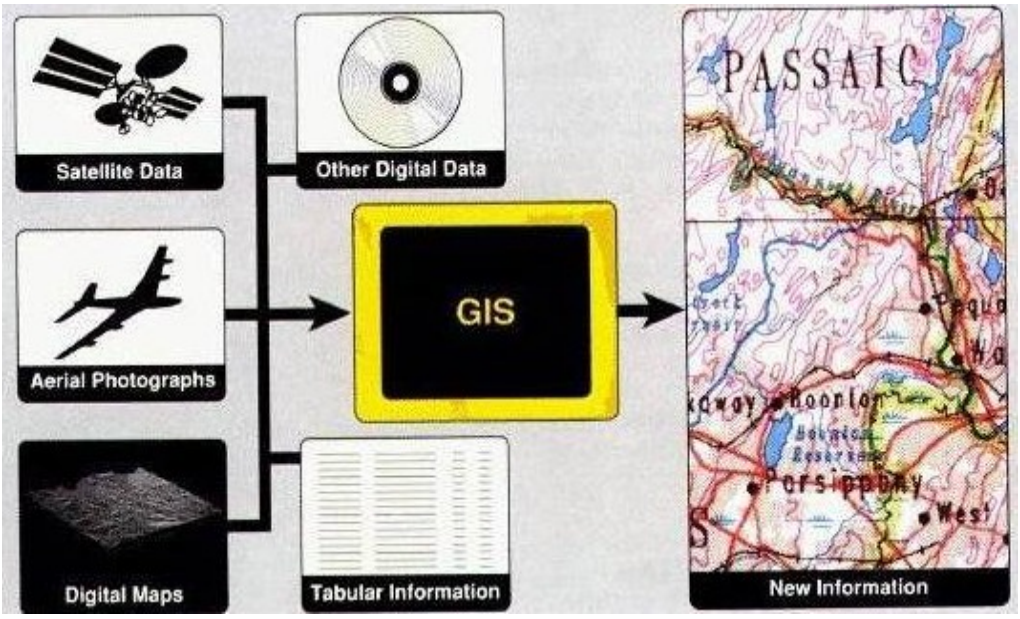

Figure 2.8: Data Integration and Data Management through GIS.

For many applications GIS, remote sensing, or both in combination are the most important aspects of GIS since the only real point of working with geographic information systems is to solve substantial real-world problems. GIS is perhaps best considered a methodology or collection of tools which, when applied, can bring great benefit. Remote sensing and GIS can contribute a great deal to our study of patterns and processes on the surface of the earth and to create decision support systems.

It is possible to classify GIS applications as traditional, developing, and new. Traditional GIS application fields include military, government, education, and utilities. The developing GIS application fields of the mid 1990s include a whole raft of general businesses like, banking and financial services, transportation logistics, real estate, and market analysis. New application areas, which are probably due for take-off in the next decade, include small office/home office and personal or consumer applications (Reddy, 2008). This simple classification, although useful in itself, hides a complexity of approaches to applying GIS. More specifically, a different way of examining trends in GIS application is to look at the diffusion of GIS use. Grimshaw (1994) has provided different levels at which GIS can be used within organizations. The levels are operational, tactical, and strategic.

The abuse of the analytical subsystem of a GIS is the result of a lack of understanding of the nature of the spatial data contained in the subsystem. Beyond the problems of GIS abuse, there is a common belief that GIS is the panacea for all geographical problems. In many cases the user will be obliged to combine GIS tools with statistical analysis software, input-output modelling

tools providing enhanced mathematical computations, geostatistical packages designed for advanced spatial analysis or sub-surface modelling called GIS applications development and customisation of softwares with respect to user's requirements (Reddy, 2008).

The application of watershed models requires the efficient management of large spatial and temporal datasets, which involves data acquisition, storage, and processing of modelling inputs as well as the manipulation, reporting, and display of results. These management requirements are usually met by integrating watershed simulation models and GISs, generating the capacity to manage large volumes of data in a common spatial structure.

Original attempts to link GIS to hydrological modelling began in the mid 1970s (Correia et al., 1998). Not until the early 1990s when GIS increased its functionality did hydrology really take advantage of this technology. GIS expanded the possibilities of hydrological modelling since it can handle a large amount of data. The main function of GIS in hydrology is to assist in the management of land and water resources (Meijerink et al., 1994). For example, the parameters of the hydrological models are related to soil characteristics and land use. Soil characteristics can be derived from the existing hydrogeological and soil maps. Land use maps can be generated by aerial photography or satellite imagery.

2.2.2 Limitations of GIS in Hydrological Modelling

Several differences between GIS and hydrological models limit the effectiveness of the coupling between them (Frey, 2004). GIS is made for the processing of a vast amount of data, while hydrological models are rather concerned by very precise and detailed analysis of a small area. This difference makes that GIS is insufficient to process hydrological data. Hydrological models are time-varying, particularly for surface water flow, and GIS has no explicit representation of time in its data structure, this is why GIS is mainly used for data input and output. GIS and hydrological models do not use the same idea on relationship among data. In a GIS, a relation is a simple association between two sets of data using a key item common to them. In hydrological models, a relation is usually expressed as a complex mathematical function.

Romanowicz et al. (1993) pointed that the limitations of this coupling attempt from a hydrological point of view. DeVautier and Feldman (1993) presented a complete review of GIS-based hydrological modelling approaches. Correia et al. (1997) also addressed this topic. The major weakness of GIS is that the time temporal processes are not easily accommodated.

To circumvent this limitation it is possible to couple the GIS with a peripheral computer on which the hydrological and hydraulic models run. Results from these models can be transferred back to the GIS and then the spatial operations can proceed in this system. This approach has been proved to be a suitable approach for hydrological models being used (XSRAIN and OMEGA)

and the hydraulic model (HEC-2) which used for flood mapping (Correia et al., 1998). There is also a trend among commercial GIS towards a better interface with a wider range of data types and a closer integration within a single software system of what were once separate software capabilities, such as hydrological modelling in ArcMap.

2.2.3 Spatial Hydrological Models

Hydrological modelling is a powerful technique of hydrological system investigation for both research hydrologists and practicing water resources engineers involved in the planning and development of integrated management of water resources (Seth et al., 1999). Hydrological models are defined as mathematical representations of the flow of water and its constituents in some parts of the land surface or subsurface environment (Maidment, 1993). Environmental modelling of this kind provides numerous benefits: (i) it explains the physical world; (ii) it provides decision support to resources and hazard management (Moore et al., 1993); and (iii) it guides experimentation and research for presenting complex ideas in an accessible manner (Burrough, 1997). Hydrological models can be considered as stand-alone programs with data loaded via the import and export facilities within the model itself without the help of any GIS package, or as coupled to a GIS system through an interface solely designed for that purpose.

2.2.3.1 Stand-alone Models

The stand-alone programs depend on a particular computing platform or hardware configuration such as the Windows-based Watershed Modelling System (WMS reference, 1999) and GIBSI (Mailhot et al., 1997), the UNIX-based Modular Modelling System (MMS manual), or the DOS and UNIX-based PCRaster (Wesseling et al., 1996). They all run from an individual computer or from several computers on a local area network that is not necessarily connected to a global network, and are then made accessible to the public or to managers in geographically separate locations. One of the known and widely used models is HEC-1 from the Hydrologic Engineering Center (HEC) of the US Army Corps of Engineers (USACE), which provides a variety of options for simulating precipitation-runoff processes. A new interactive version, which replaces the command-line-oriented program HEC-1 (flood hydrograph model) is HEC-HMS (Hydrologic Modelling System). This stand-alone rainfall runoff modelling program has been implemented under both UNIX (Sun Solaris) and Windows operating system. It has a GUI, integrated hydrological analysis components, data storage and management capabilities, and graphics and reporting facilities. Furthermore, a significant amount of data must be gathered to perform hydrological analysis using HEC-1 (Nelson et al., 1994). HMS is designed to be independent of any commercial GIS, so it has no explicit ties to any of them. The highly flexible HEC-HMS allows the watershed to be modeled in a distributed manner, accepts data in time increments of minutes to hours,

and runs easily on a PC platform (USACE, 2010). For these reasons it has been applied in this thesis.

Another program that is well known and can be used as stand-alone is the WMS (Nelson et al., 1995). It is a graphics-based, comprehensive hydrological modelling environment that addresses the requirements of rainfall runoff computer simulations (DeBarry et al., 1999). The last example is the TOPMODEL which is classified as a distributed to semi-distributed model. A number of applications of this model have been presented (Beven, 1997 & Obled et al., 1994). It is not intended to be a modelling package, but rather a set of conceptual tools that can simulate the hydrological behaviour of a watershed (Beven, et al., 1995).

2.2.3.2 GIS and Hydrological Model Coupling Method

Most current hydrological models that take advantage of a GIS link to other programs to perform the hydrological analysis. The coupling of hydrological and hydraulic models with GIS is a very fruitful way of studying different scenarios. This coupling still raises difficulties because relations seem weak in GIS compared to hydrological models. GIS is not capable of handling the complex physical laws that control hydrological processes. However, this limitation can be circumvented by doing part of the hydrological and hydraulic calculations in a different system that is linked to GIS. The way that hydrological analysis is done using GIS is often referred to as either loosely or tightly coupled with variations in between. Four different approaches have been developed to integrate the GIS: GIS embedded within a hydrological model, a hydrological model embedded within a GIS, loose coupling and tight couplings between a hydrological model and GIS (Manson, 2003). Those four approaches have their own advantages and disadvantages.

GIS embedded with a hydrological model has the advantage of giving developers more freedom to design their own system in which the coupling strategy and the use of the hydrological component is not dependent or limited by the GIS data structure. The limitation, however, is that the visualization and data management capabilities are not enough compared to the stand-alone GIS. Furthermore, programming efforts required to achieve this coupling strategy are seen as intensive and occasionally redundant. Some examples of this approach include a variety of the HEC series of models developed by the US Army Corps of Engineers, the LDMS (Low-Dimensional Modelling System) as well as the MODFLOW (3D finite-difference ground-water Flow Model; Sui & Maggio, 1999).

The approach in which hydrological models are embedded with a GIS takes advantage of the suite of collection, storage, analysis and visualization capabilities of commercial stand-alone GIS packages. In this approach, the hydrological functionality is often criticized and does not often conform to the conventional hydrological modelling. This is especially true in the case of issues

relating to model calibration and validation where often models of this type must be calibrated outside by the existing model (Sui & Maggio, 1999). One example of this includes the Environmental Systems Research Institute's (ESRI's) ArcHydro. In the loose coupling approach, GIS is primarily used to organize data. Loose coupling is commonly done by performing initial analysis in the GIS, converting this information into a useable form for hydrological modelling, performing the hydrological analysis, and finally transferring the information back to the GIS for display (Hellwegger & Maidment, 1999). Comparing with the tightly coupled analysis, loosely coupled analysis is more common because the former needs complex interface. In the tight coupling approach, data analysis is integrated in one program, either the hydrological model or GIS, which has a link to the other program to perform limited operations (VerWest, 2002).

Attempts to couple GIS with hydrological and hydraulic models started in 1975, when the HEC worked on the integration of HEC-I in GIS using a grid-based method. The result of this effort was HEC-SAM (Spatial Analysis Methodology). In this approach, GIS served simply as a database to feed the hydrological model (Males & Grayman, 1992). The Windows program HEC-GeoHMS has been developed, which is used in this thesis. HEC-GeoHMS is an ArcMap 9.3 GIS extension specifically designed to process geospatial data for use with HEC-HMS. It allows users to visualize spatial information, delineate watersheds and streams, extract physical watershed and stream characteristics, perform spatial analyses, and create HEC-HMS model input files (Figure 2.9). HEC-GeoHMS uses the ArcMap Spatial Analyst Extension tool to develop a number of hydrologic modelling inputs. Analysing digital terrain information, HEC-GeoHMS transforms drainage paths and watershed boundaries into a hydrologic data structure that represents watershed response to precipitation.

Because of the above mentioned reason, the loose coupling approach is the most popular method; there exist numerous examples based on it. For example, the GRASS GIS package was linked with TOPMODEL to examine the effects of soil heterogeneity in a small watershed. TOP MODEL is a relief-based surface water model developed in 1979 (Beven & Kirkby, 1979). This semi-distributed model makes directly use of detailed DTM data. Some popular GIS-based hydrological models can be found in Singh (1995) & Shamsi (2002).

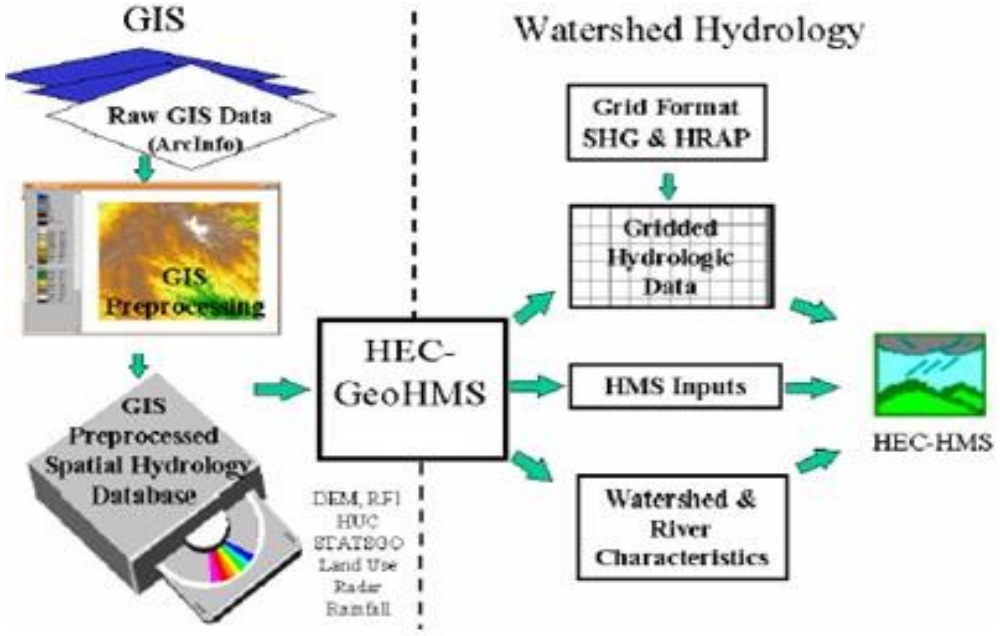

Figure 2.9: Example of Linking GIS & Hydrologic Models (from USACE, 2010).

2.2.4 Watershed Delineation

Watershed or catchment is a topographically delineated area drained by a stream system; that is the total land area above some point on a stream or river that drains past that point. The watershed is a hydrologic unit often used as a physical biological unit and a socioeconomic-political unit for the planning and management of natural resources (Peter et al., 2003). Watershed delineation is the process of identifying the drainage area of a point or set of points, it is one of the most commonly performed activities in hydrological and environmental analyses (Djokic et al., 1997). The basic data requirement for watershed delineation is a DTM. It provides good terrain representation from which the watersheds can be derived automatically using GIS technology. The techniques for automated watershed delineation have been available since the mid-eighties and have been implemented in various GIS systems and customer applications (Garbrecht & Martz, 1999).

Watersheds have been utilized as a basic unit in water resource analysis because they contain components that are interrelated and can be viewed as a single interactive ecological system. When choosing a method to present a

surface, it is important to consider its end use. The ideal structure for a DTM may be different when it is used for a distributed hydrological model or to determine the topographic attributes of the landscape. Techniques for extracting drainage networks from a DTM has been described by many researchers including Olivera et al. (2002) & Tarboton et al. (1991). The commercial software (HEC-HMS) which has been used in this study accepts only grid-type DTM as input, as will be discussed in Chapter 4.

2.3 Flood Characteristics

2.3.1 Flood Definitions and Meaning

A meaningful definition of floods should not only incorporate the notions of inundation and damage, but also move beyond the restrictive definitions of river floods given, for example, by Chow (1956). Flood is natural or man-made disaster caused by flooding when water table has reached the river bank and the severity of this disaster depends on conditions and size of flood (Chow, 1980). Flood happen when the rate of water flow has become more intense than the river could hold, it would spread all over urban, agricultural and forest area. Therefore, flood is more danger than flooding. This coincides with the concept of flooding defined as water flowing or trapping in various areas without area owner's consent (Mangsilp, 2007). If damages resulted from flooding, it should be called flood (Strahler & Strahler, 1983). Flood is a relatively high flow which overtaxes the natural channel provided for the runoff (Leopold et al., 1964). It is water flowing in strong current until causing loss of lives and assets. In other words, floods result from more water than streams and rivers could hold. Most floods happened at lower watersheds with movement of water from high to low areas of watershed (Brook et al., 1991).

Problems related to flooding have greatly increased over recent decades because of population growth and the subsequent development of extensive infrastructures in close proximity to rivers. Increased frequency of extreme rainfall events, characteristic for the changing climate, can also potentially contribute to this problem (Al-Sabhan et al., 2003).

2.3.2 Floods as Hazards

2.3.2.1 Flooding as a Natural Hazard

Because of its devastating nature, flooding poses serious hazards to lives and livelihoods in many parts of the world. According to the Federal Emergency Management Agency (FEMA) of the United States, flooding is one of the most common and widespread of all natural disasters.

Based on Smith & Ward (2008), natural hazards result from the potential for extreme geophysical events, such as floods, to create an unexpected threat to human life and property. When severe floods occur in areas occupied by humans, they can create natural disasters which involve the loss of human life and property plus serious disruption to the ongoing activities of large urban and rural communities. Although the terms 'natural hazards' and 'natural disasters' emphasise the role of the geophysical processes involved, these extreme events are increasingly recognised primarily as the 'triggers' of disaster, which often have more complex origins including many social and economic factors.

A flood in a remote, unpopulated region is an extreme physical event, of interest only to hydrologists. Entirely natural floodplains can be drastically

changed but not damaged by the events which create them. Indeed, most floodplain ecosystems are geared to periodic inundation. Terms such as flood risk and flood losses are, therefore, essentially human interpretations of the negative economic and social consequences of natural events. As with other human value-judgments, different groups of people have been found to differ significantly in their selection and definition of the risks from flooding (Green et al., 1991). In addition, the flood risk in any given locality may be increased by human activity, such as unwise land-use practices related to deforestation or urban development. Equally, the flood risk may be reduced by flood control structures or by effective emergency planning. The real risk from floods stems from the likelihood that a major hazardous event will occur unexpectedly and that it will impact negatively on people and their welfare.

Flood hazards result from a combination of physical exposure and human vulnerability to geophysical processes. Physical exposure reflects the type of flood events that can occur, and their statistical patterns, at a particular site, whilst human vulnerability reflects key socio-economic factors such as the number of people at risk on the floodplain or low-lying coastal zone, the extent of flood defense works and the ability of the population to anticipate and cope with hazards. It is the balance between these two elements, rather than the physical event itself, which defines natural hazard and determines the outcome of a natural disaster.

In Figure 2.10, variations of a river stage through time are plotted in relation to the band of social and economic tolerance available at a hypothetical location. As long as the river flows close to the average, or expected level, there is no hazard and the discharge will be perceived as a resource because it supplies water for useful purposes, such as irrigation or water transport. However, when the river flow exceeds some predetermined threshold of local significance and extends outside the band of tolerance, it will cease to be beneficial and be perceived as a hazard. Thus, very low or very high flows will be considered to create a drought hazard or a flood hazard respectively. The impact of the hazard will, in part, be determined by the magnitude of the event (expressed by the peak deviation beyond the damage threshold on the vertical scale) and the duration of the event (expressed by the length of time the threshold is exceeded on the horizontal scale). But the true significance of flood disaster will primarily depend on the vulnerability of the local community. Rivers often overflow their banks without creating a significant hazard and such hydrologically defined 'flood flows' may create little economic damage and produce no response from the emergency services. Indeed, like many other natural hazards, low-magnitude-high-frequency floods provide gains as well as losses to the community at risk.

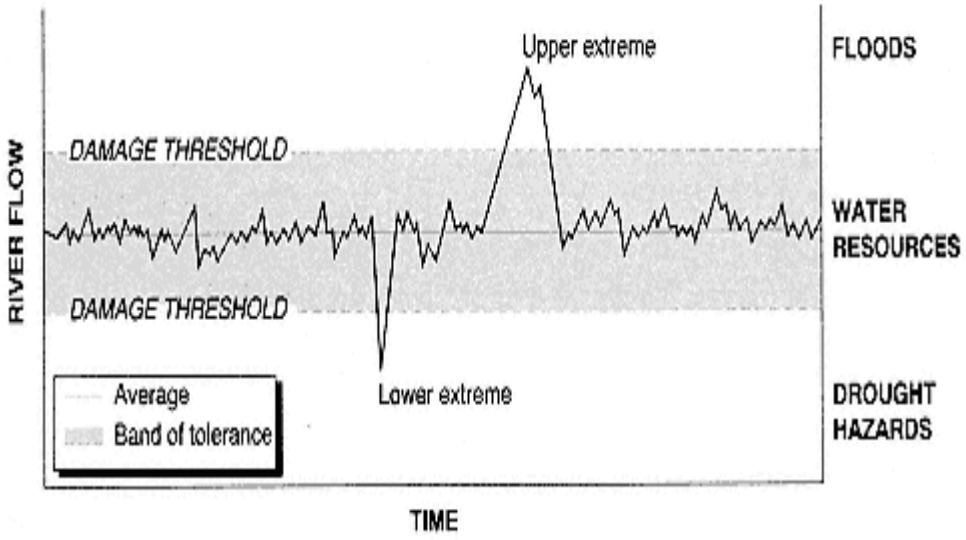

Figure 2.10: Sensitivity to Flood Hazard Expressed in Relation to the Variability of River Discharge and the Degree of Socio-conomic Tolerance at a Site (Modified after Hewitt and Burton, 1971).

Another important attribute of flood risk is the relative unpredictability of the event. Unexpectedness, combined with the difficulty of issuing precise warnings of location and timing, is a major cause of flood disaster, especially with flash floods. On the other hand, many rivers exhibit regular floods which, especially in large drainage basins, will rise slowly and predictably in a seasonal 'flood pulse', thereby offering an opportunity for an efficient loss-reducing response. Most important of all from the standpoint of effective loss mitigation, floods recur in well-identified topographical settings which can be accurately mapped and can either be defended against by engineering works or mitigated by other response strategies.

An example of one of the natural devastative flood events which happened in Europe in the last two decades is the Saxony flood in Germany. Martin Socher (2007) mentioned that in August 2002 torrential rains in Bohemia and the Ore Mountains of up to 340 mm per day (highest ever recorded values in daily precipitation for Germany) caused floods in the Elbe River and its tributaries unprecedented in written history in Saxony. In Saxony alone 21 fatalities occurred, 25,300 houses were damaged including important public buildings like hospitals, schools, and nurseries, 200 of them were destroyed. The transport infrastructure was disastrously damaged including 750 km of roads, 540 km railway network and 180 bridges. Around 18,000 individual damages at reservoirs, dykes, weirs, river embankments and other hydraulic structures occurred. In total the damage added up to more than six billion € not including

indirect losses of the private economic sector. Figure 2.11 shows examples of the damages caused in Saxony by the flood event in 2002.

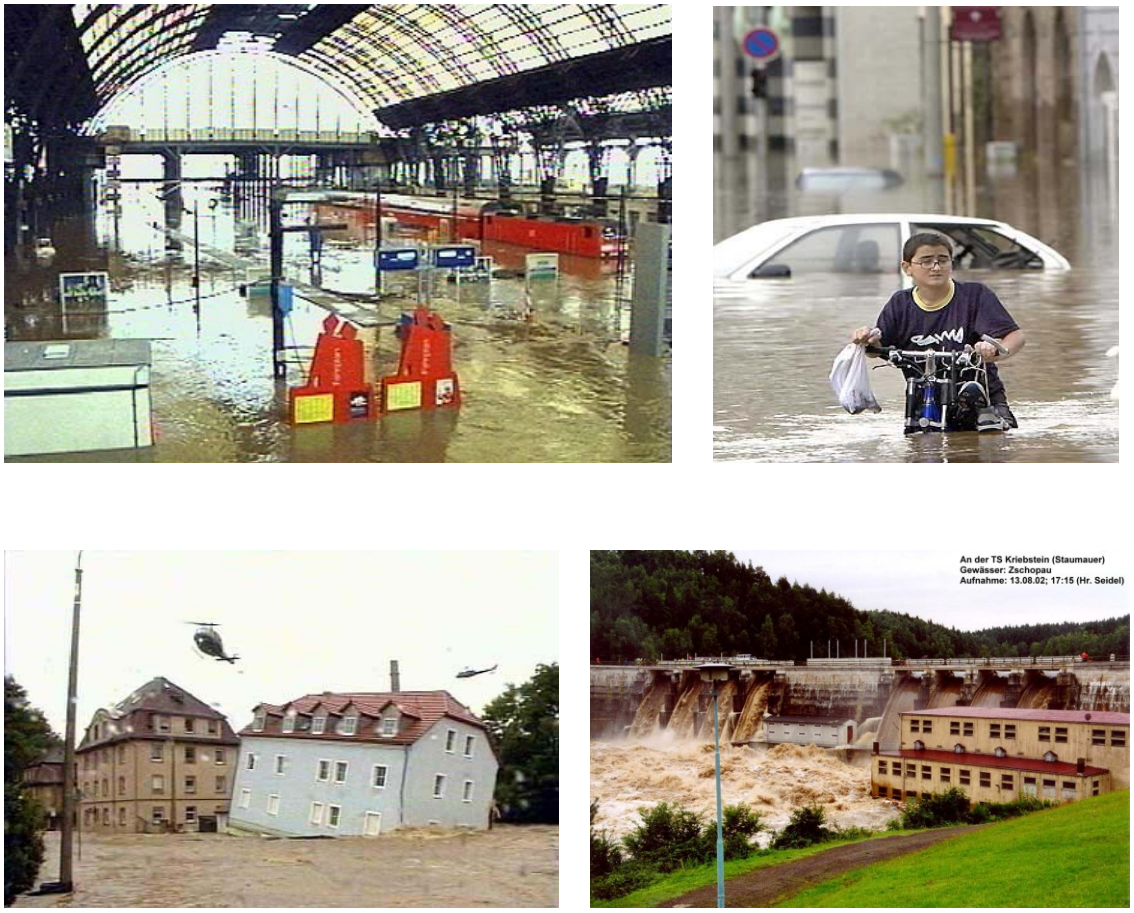

Figure 2.11: Examples of the Damages Occurring during the Saxony Flood Event 2002 (Socher, 2007).

2.3.3 Types of Flooding

Flooding can be divided into different categories according to their duration: (i) Slow-Onset Floods, (ii) Rapid-Onset Floods, and (iii) Flash Floods.

2.3.3.1 Slow-Onset Floods

Slow-Onset Floods usually last for a relatively longer period; it may last for one or more weeks, or even months. Hence, it can lead to lose of stock, damage to agricultural products, roads and rail links.

2.3.3.2 Rapid-Onset Floods

Rapid-Onset Floods last for a relatively shorter period; they usually last for one or two days only. Although this kind of flood lasts for a shorter period, it can cause massive damages and pose great risk to life and property as people usually have less time to take preventative action during rapid-onset floods.

2.3.3.3 Flash Floods

Flash Floods may occur within minutes or a few hours after heavy rainfall, tropical storm, failure of dams or levees or releases of ice jams. They cause the greatest damages to society.

Flooding can also be divided into different categories according to their location: (i) River Flood, (ii) Coastal Floods, (iii) Arroyos Floods and (v) Urban Floods.

2.3.3.4 River Floods

This is the most common type of flooding. Floods in river valleys occur mostly on floodplains or washlands as a result of flow exceeding the capacity of the stream channels and overspilling the natural banks or artificial embankments. Sometimes inundation of the floodplain, or of other flat areas, occurs in wet conditions when an already shallow water-table rises above the level of the ground surface. This type of water-table flooding is often an immediate precursor of overspill flooding from the stream channels.

2.3.3.5 Coastal Floods

Coastal Floods usually occur along coastal areas, including estuaries and deltas, involve the inundation of land by brackish or saline water. Brackish-water floods result when river water overspills embankments in coastal reaches as flow into the sea is impeded by high-tide conditions.

Overspill is exacerbated when high-tide levels are increased above normal by storm-surge conditions or when large freshwater flood flows are moving down an estuary.

2.3.3.6 Arroyos Floods

An arroyo is a dry riverbed which tends to fill with water in the rainy season. When there are storms approaching these areas, fast-moving river will normally form along the gully and cause damages, as they are prone to flash-flooding and erosion. An equivalent is the occasional flooding of wadis in desert areas.

2.3.3.7 Urban Floods

When metropolitan areas experience heavy rainfall, unless the city has a sufficient drainage system, streets will flood because most of them are usually paved. Also the lack of absorption materials like trees and grass which lead to urban floods.

2.3.4 Causes of Floods

Most river floods result directly or indirectly from climatological events such as excessively heavy and/or excessively prolonged rainfall. In cold-winter areas, where snowfall accumulates, substantial flooding usually occurs during the period of snowmelt and ice-melt in spring and early summer, particularly when melt rates are high. Floods may also result from the effects of rain falling on an already decaying and melting snowpack. An additional cause of flooding in cold-winter areas is the sudden collapse of ice jams, formed during the break-up of river ice. According to Mangsilp (2007) there are two major causes of flooding:

2.3.4.1 Direct Cause

The direct causes of flood are summarised in Table 2.4.

Table 2.5: Direct Causes of Flood.

Cause		Events
Prolongated heavy rainfall	It caused by different events such as: Tropical Cyclones include clusters of low pressure that developed into tropical storm and Monsoon which is traditionally defined as a seasonal reversing wind accompanied by seasonal changes in precipitation.	In November 2006, heavy rain caused large parts of Afghanistan to flood. The official death toll was set on 80, and it took more than two days to reach some of the most severely flooded villages.
Sloping terrain	It would cause severe flood. Flood that has happened this way would be so sudden.	
High tidal	It is happened at highest elevation, so called, highest tide is when sea water also support river water which caused the reduction or stop water flow and unable to drain into the sea.	Hurricane Ike is a costliest hurricane which make landfall in Galveston Island, Texas, USA. It made landfall on Sep. 2008. Its effects were crippling and long-lasting. Ike's effects included deaths and widespread damage.
Earthquake/ Volcanic outburst	Results from earthquake or volcano ruption under the water have affected some parts of earth surface extensively. Some parts of earth surface would be pushed higher while some parts collapsed and caused waves along the shorelines.	The Indian Ocean earthquake was an undersea megathrust earthquake that occurred on Dec. 2004 with an epicenter off the west coast of Sumatra, Indonesia.
Dam collapse	It caused by a sudden flood might create extensive damage, especially in the surrounding of the break.	Record flooding caused failure of the Lake Delhi Dam in Iowa, USA on July 2010. Up to 300 houses around the lake were flooded.

2.3.4.2 Indirect Cause

Man-made flood cause, flood caused by collapsing dams, has resulted from rapid growth and increasing numbers of population in urban areas. With the city expansion, increasing construction would obstruct water passage and block drainage area.

2.3.5 Flood Applications in Remote Sensing

The application of satellite data to flood mapping began with the launch of the first remote sensing satellite Landsat-1 in the early 1970's (Hallberg el al., 1973 & Morrison and White, 1976). Spatial and temporal patterns of inundation areas can be inferred from multi-temporal satellite images: visible/infrared (IR) or SAR sensors are used to delineate floodplains (Hess et al., 2003; Mertes et al., 1995; Smith, 1997 & Toyra et al., 2001). In addition, the potential of satellite radar altimetry for monitoring water levels of large rivers has already been demonstrated (Birkett, 1998; de Oliveira et al., 2001 & Maheu et al., 2003). Birkett et al. (2002) undertook an extensive validation study of water levels derived from Topex / Poseidon radar altimeter over the entire Amazon basin and used satellite radar altimetry to estimate elevation profiles and water surface gradients along the Amazon mainstream.

Remote sensing considered as a very effective tool for flood management in different ways; it introduces detailed mapping that is required for the production of hazard assessment maps and for input to various types of hydrological models, it develops also a larger scale view of the general flood situation within a river basin with the aim of identifying areas at greatest risk and in the need of immediate assistance. Remote sensing and GIS techniques have successfully established their applications in following areas of flood management such as flood inundation mapping, flood plain zoning and river morphological studies.

2.3.5.1 Flood Inundation Mapping

Flood mapping during the flooding and flood plain mapping after the flood recedes is essential. One of the important information required is the nature and extent of the damage caused by floods in the flood prone areas.

Satellite remote sensing provides synoptic view of the flood-affected areas at frequent intervals for assessing the progression and recession of the flood inundation in short span of time which can be used for planning and organizing the relief operations effectively. Remote sensing can effectively be used for mapping the flood-damaged areas. For mapping purposes, a pre-flood scene and a peak flood image would be compared to delineate the inundated area. Flood inundation maps can be used to (i) define spatial extent of flood inundation, (ii) identify the worst flood affected areas, and (iii) evaluate impact of

flooding on environmental concerns, such as, coastlines, forests, open space etc.

2.3.5.2 Flood Plain Zoning

Flood hazard zone mapping can be used as a means of non-structural flood control planning of the flood plain and for making policy decisions to regulate the flood plain development activities. Using historic satellite data combined with hydrological and close contour data, a flood hazard zone map can be prepared for flood prone basins.

2.3.5.3 River Morphological Studies

River morphology is concerned with the structure and form of rivers including channel configuration, channel geometry, bed form and profile characteristics. Various flood control structural measures such as construction of embankments, channel improvements, raising of villages, selective dredging etc. have been implemented in past to reduce the impact of the flood disaster on human life and property. It is essential to monitor the embankments regularly to identify the vulnerable reaches. Conventional methods of river survey time consuming and expensive. Most of the flood prone rivers in India change their course after every flood wave eroding river banks. Satellite remote sensing based morphological studies are quite useful to identify the changes in river course over a time period and also identifying the erosion prone areas along the river course. Moreover, it considered a powerful tool to evaluate the efficacy of flood management structures.

The river configuration and flood control works maps can be effectively used to identify the vulnerable river reaches and status of the flood control embankments/spurs so that necessary measures can be taken accordingly to avoid breaches. The bank erosion maps can be used for planning bank protection works. The study of river configuration will be useful to understand the behavior of the river and can be used for laying physical models.

Chapter 3: Tools and Methods

In this chapter, a description of the study area, the used data sets and their sources, the applied instruments and softwares, and the general layout of the implemented methodology are presented.

3.1 Study Area

The Gottleuba Catchment, approximately 400 sqkm in size, located south of Pirna (Saxony, Germany) is investigated (Figure 3.1). The central coordinates are 50° 52' 30" N and 13° 45‘ 30" E, with approximately 22 km width and 18 km length. Pirna is located southeast of Dresden near the Elbsandsteingebirge in the Elbe Valley, where the nearby rivers Wesenitz from the north and Gottleuba from the south drain into the Elbe. Pirna is also called ''Tor zur Sächsischen Schweiz '' (''Gate to the Saxon Switzerland''). The Sächsische Weinstraße leads from Pirna over Pillnitz, Dresden, and Meißen to Diesbar-Seußlitz was dedicated in 1992. In August 2002 the city suffered great damage in the widest-spread flooding in Europe for many decades.

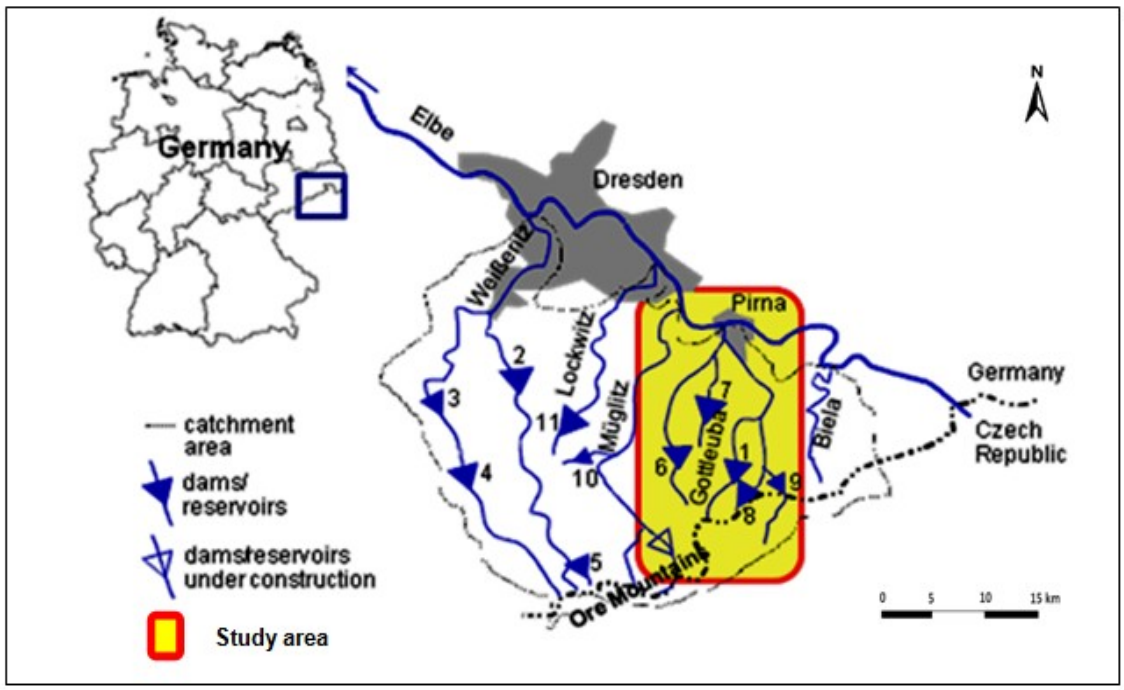

Figure 3.1: Gottleuba Catchment (Saxony, Germany), (Socher, 2007).

According to the management report issued by the ''Sächsisches Landesamt für Umwelt, Landwirtschaft und Geologie'' (LfULG, 2004), the flood was caused by rainfall which was exceptional in terms of intensity, duration and areal distribution. More than 200 mm of rain fell in large parts of the Osterzgebirge in just three days. That is between two to three times as much as the average rainfall for the entire month of August. However, the one-day values for rainfall in the peak precipitation area, which was rather small, were very close to the

physically possible maximum. Because of its geological condition and the moisture it already contained, the soil was incapable of absorbing much water and was quickly saturated. As a result, it could neither hold water, nor delay discharge in any significant way. Consequently, 60 to 90 per cent of the precipitation ran off in many areas with a very short period of time. This led to discharge rates far beyond any known values in almost all of the investigated watercourses.

Gottleuba River is one of the five Elbe tributaries of the River Elbe in the ''Ore Mountains''. Table 3.1 lists the precipitations in their catchments. In Saxony the typical mean rainfall value is about 660 mm per year. In 2002 the highest precipitation value near the source of the Müglitz and Weißeritz Rivers, was recorded. In addition, high precipitation and humidity values were measured at the time before the event. The event caused massive damage in the river valleys.

Table 3.1: Intensity of Precipitation during 24 and 72 Hours (LfULG, 2004).

River	Precipitation at 12/08/2002 (mm)	Precipitation from 11/08/2002 to 13/08/2002 (mm)
Biela	150	191
Gottleuba	182	231
Müglitz	237	296
Lockwitz	194	245
Weißeritz	220	265

3.2 Data Sources

It is important to critically screen the data in order to meet the needs of the methods applied in this thesis. Spatial data come in different formats, such as resolutions, intended uses etc.. Based on the objectives and methodology of this thesis, the main data required are DTM, landuse and land soilmaps, TSX data, ALOS PALSAR data, water storage data, hydrological data, and meteorological data.

3.2.1 DTM

A high-resolution Airborne Laser Scanning (ALS) - derived DTM (2m) is recommended for the hydrological application in this study to improve the spatial resolution of the delineated watershed. The DTM data (ATKIS-DGM2) with high resolution were provided from the *Staatsbetrieb Geobasisinformation und Vermessung Sachsen* (GeoSN), Germany. The ATKIS-DGM2 describes the ground surface by spatial coordinates of a representative set of ground points. From each grid point the position and the elevation can be determined with a grid spacing of 2 meters with height accuracy of + / - 0.2 m (www2) as shown in Figures 3.2 & 3.3. The surface points, such as buildings and vegetation are not included in this model. ATKIS (Authoritative Topographic-

Cartographic Information System) is a product of the Working Committee of the Surveying Authorities of the States of the Federal Republic of Germany, AdV.

```
4530000   5660292   169.18
4530000   5660294   169.04
4530000   5660296   168.95
4530000   5660298   168.85
4530000   5660300   168.78
4530000   5660302   168.70
4530000   5660304   168.65
4530000   5660306   168.53
```

Figure 3.2: General Extract from ASCII File of ATKIS-DGM2.

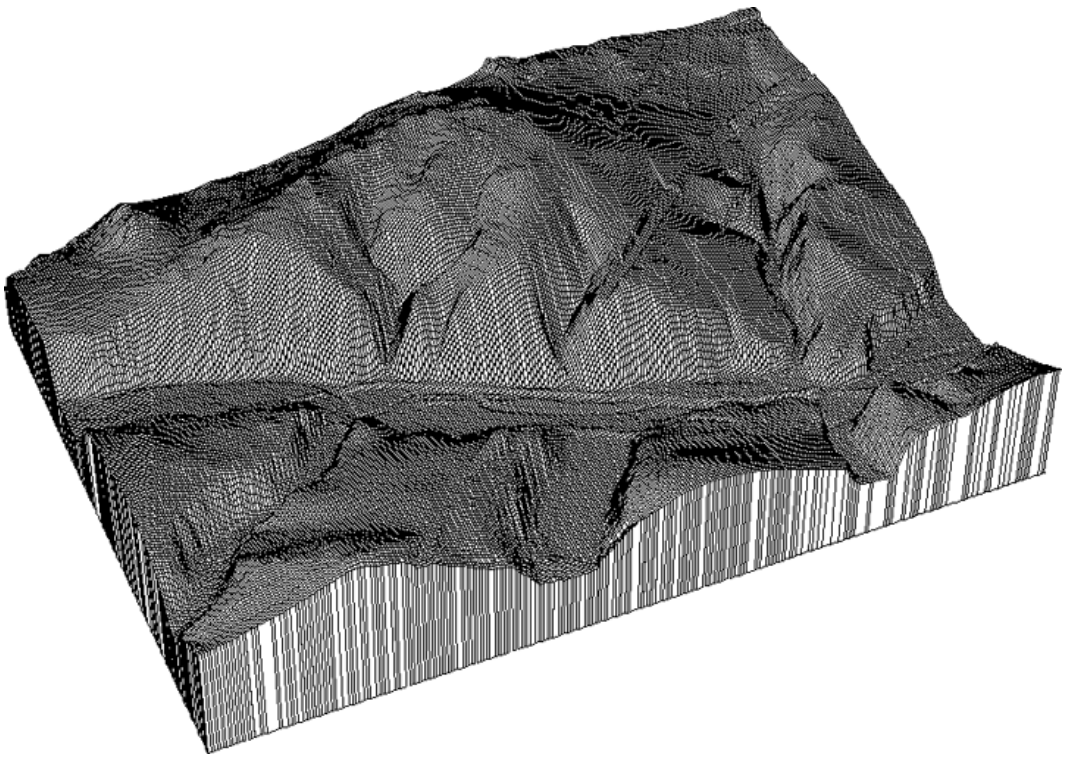

Figure 3.3: General Extract from Grid File of ATKIS-DGM2.

3.2.2 Landuse Map

The landuse data were obtained from the GeoSN. The acquired data are ‘‘Biotoptypen- und Landnutzungskartierung (BTLNK)‘‘. The BTLNK data were produced through within a project between the *Staatsbetrieb Geobasisinformation und Vermessung Sachsen* and the *Saxon State Ministry of the Environment and Agriculture* in 2005. They provide information about the actual status of the landscape features of the Free State of Saxony, Germany. The obtained landuse is illustrated in Figure 3.4.

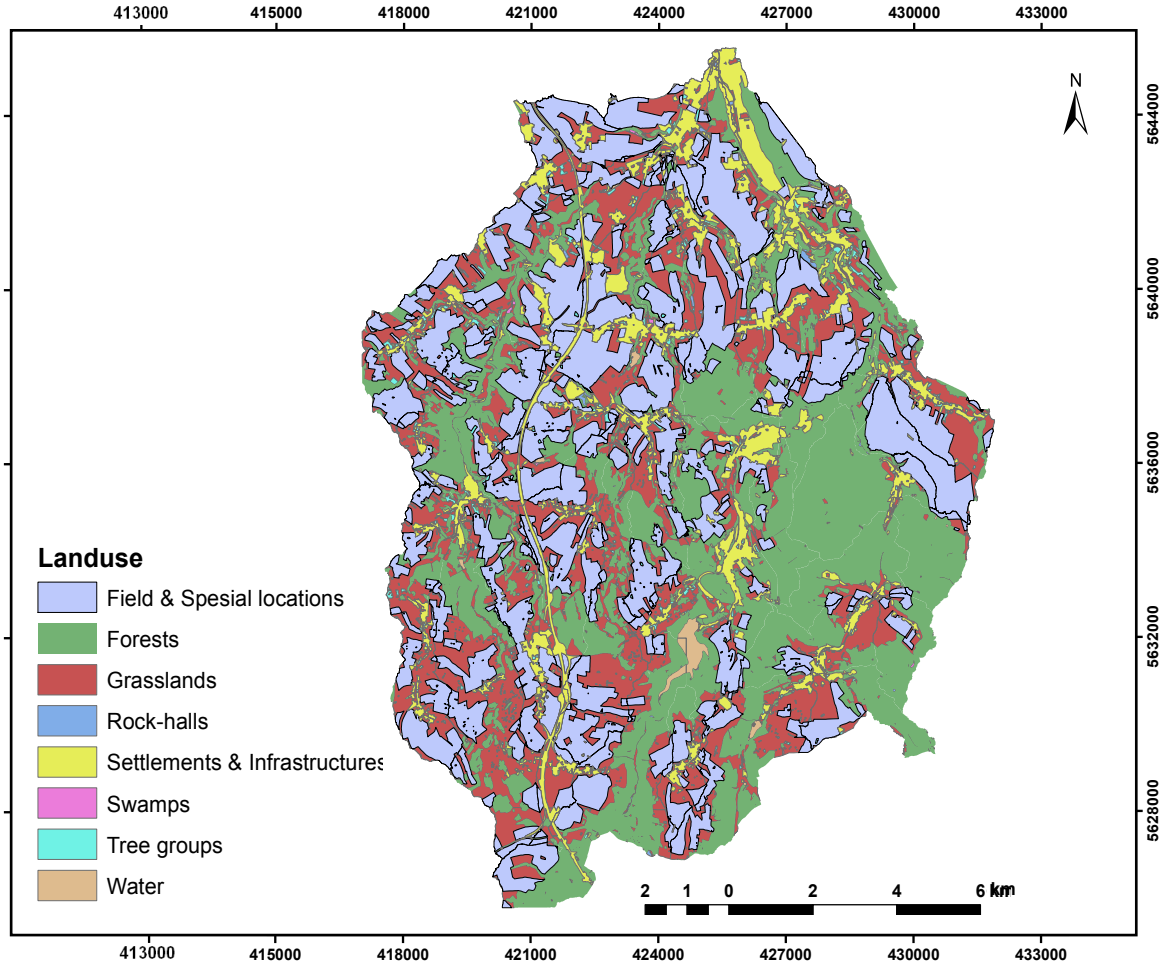

Figure 3.4: Landuse Map of Gottleuba Catchment.

3.2.3 Soil Map

The soilmap data were obtained from GeoSN. The acquired data are Bodenkonzeptkarten (BKkonz). The BKkonz is a general map based on older data. It was derived and combined from agricultural and forest site maps. The units of the BKkonz represent contours of regional agricultural and forest in the field location types. The assignment of the pedological contents was carried out by experts. The encoding is essentially on the basis of the German Soil

Mapping Instructions (4th Edition, Hanover 1994). The obtained soilmap is shown in Figure 3.5.

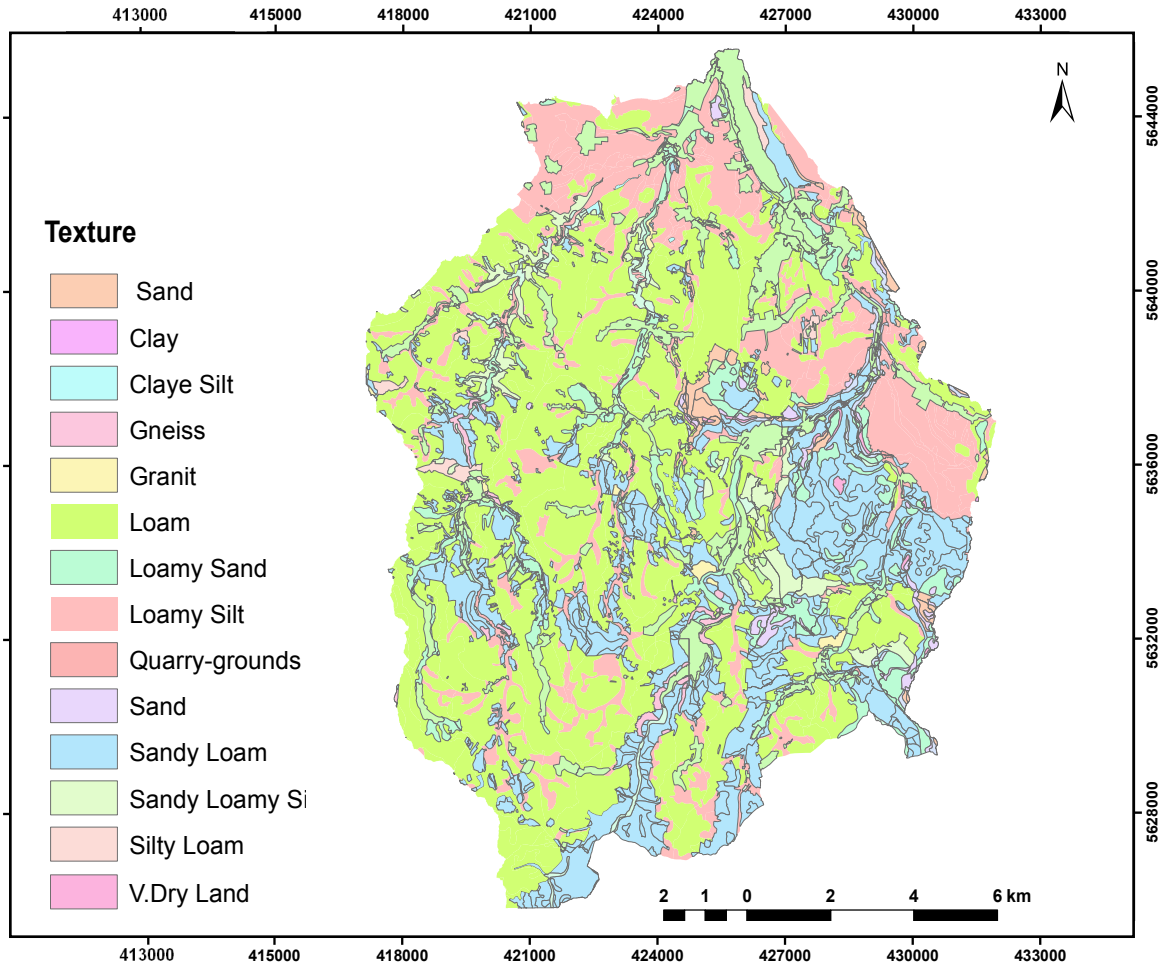

Figure 3.5: Soilmap of Gottleuba Catchment.

3.2.4 Spaceborne SAR Data

3.2.4.1 TerraSAR-X

On 31.05 and 17.06.2010 two TSX images were acquired by DLR in Stripmap mode with a pixel size of 3 m. The absolute radiometric accuracy in Stripmap mode is specified to be 0.71 dB. The main characteristics are shown in Table 3.2. The obtained TSX image of 31.05.2010 and its location are shown in Figure 3.6.

Table 3.2: Main Characteristics of TSX Images.

Sensor	Freq.	Date	Time UTC	Inc. angle	Pol.	Orbit direction
TSX	9.65 GHz	31.05.210	16:51	43°	HH	Ascending
		17.06.210	16:43	31°	HH	Ascending

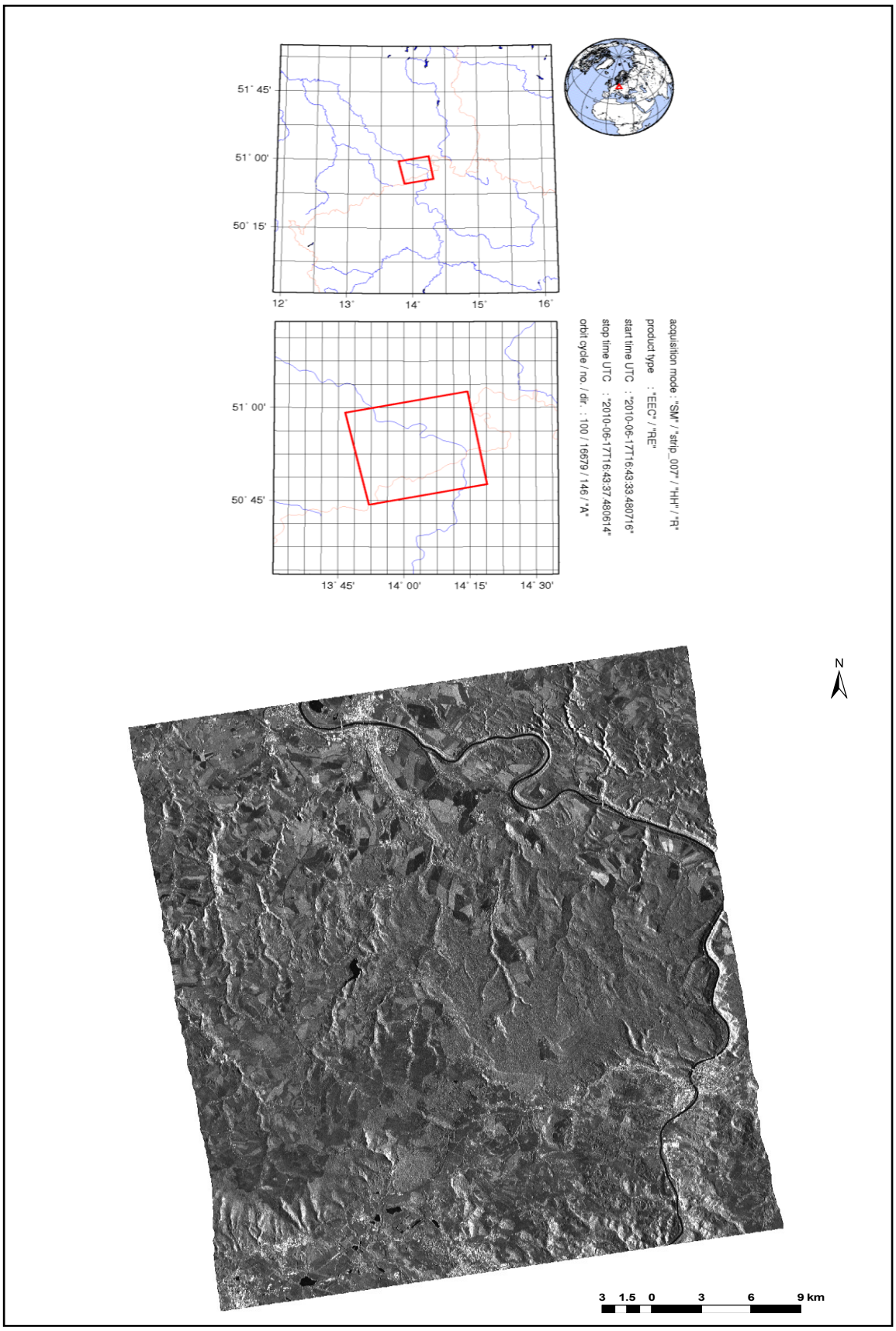

Figure 3.6: TSX Image Acquired on 31.05.2010.

3.2.4.2 ALOS PALSAR Data

On 31.05.2010 at 21:21 UTC one ALOS PALSAR image with 12 m pixel size was acquired from the Earth Observation Link (EOLi). EOLi is the ESA's client for Earth Observation Catalogue and Ordering Services. Within the period between 31.07.2009 until 09.08.2010 six orders were placed as demonstrated in Figure 3.7, only two of them were confirmed. The first image was acquisitioned on 31.05.2010 and delivered on 23.07.2010 covering the right part of the study area, and the other image was acquisitioned on 17.06.2010 and delivered on 19.08.2010 with a wrong location. Several attempts were carried to make EOLi correct this error from their side, or to order another alternative image without success. Therefore, only one ALOS PALSAR image was applied in this thesis in addition to the two TSX images. The acquisition mode of the obtained ALOS PALSAR image (1.27 GHz) is Fine Beam Double Polarisation (FBD) HH+HV, with an Incidence angle is 34° and an ascending orbital direction. The ALOS PALSAR image acquired on 31.05.210 and its location are shown in Figure 3.8.

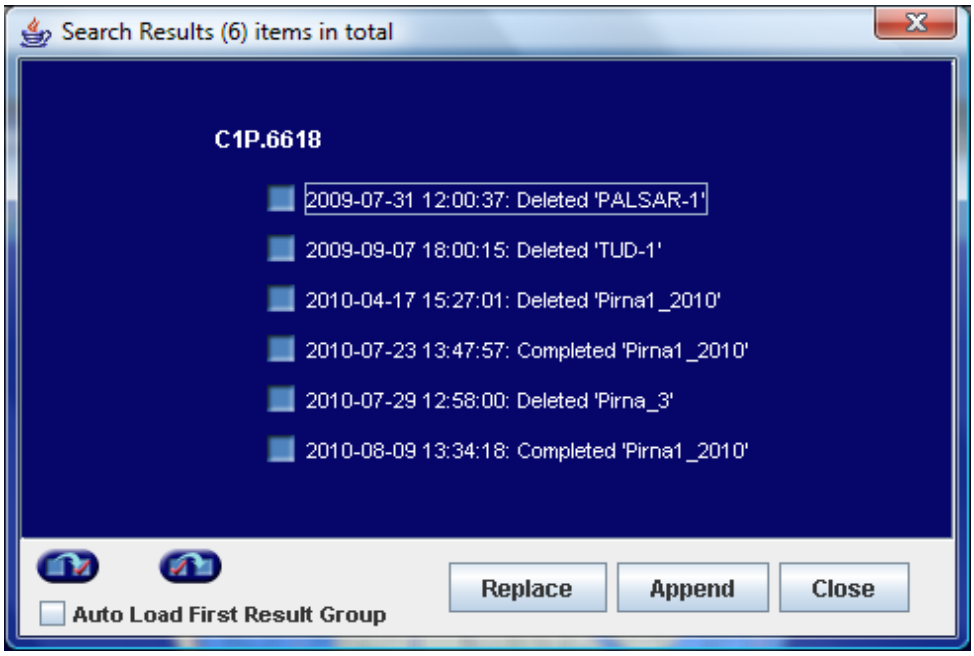

Figure 3.7: ALOS PALSAR Orders History.

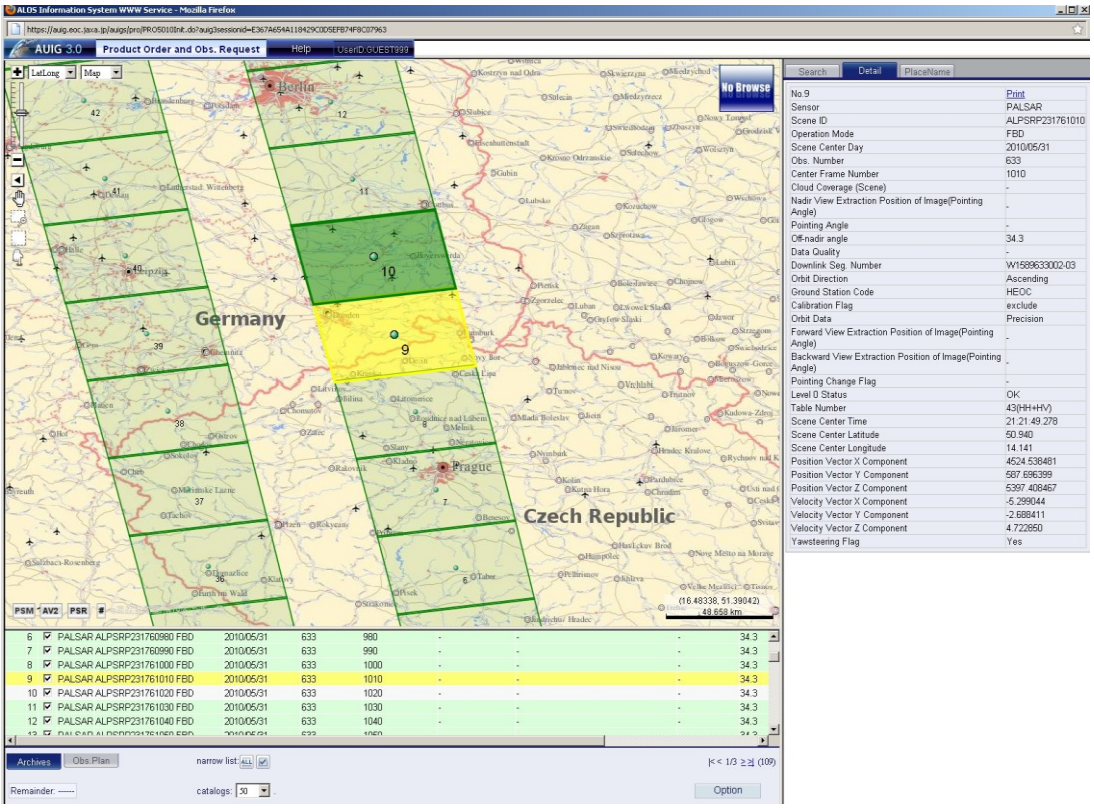

Acquired image

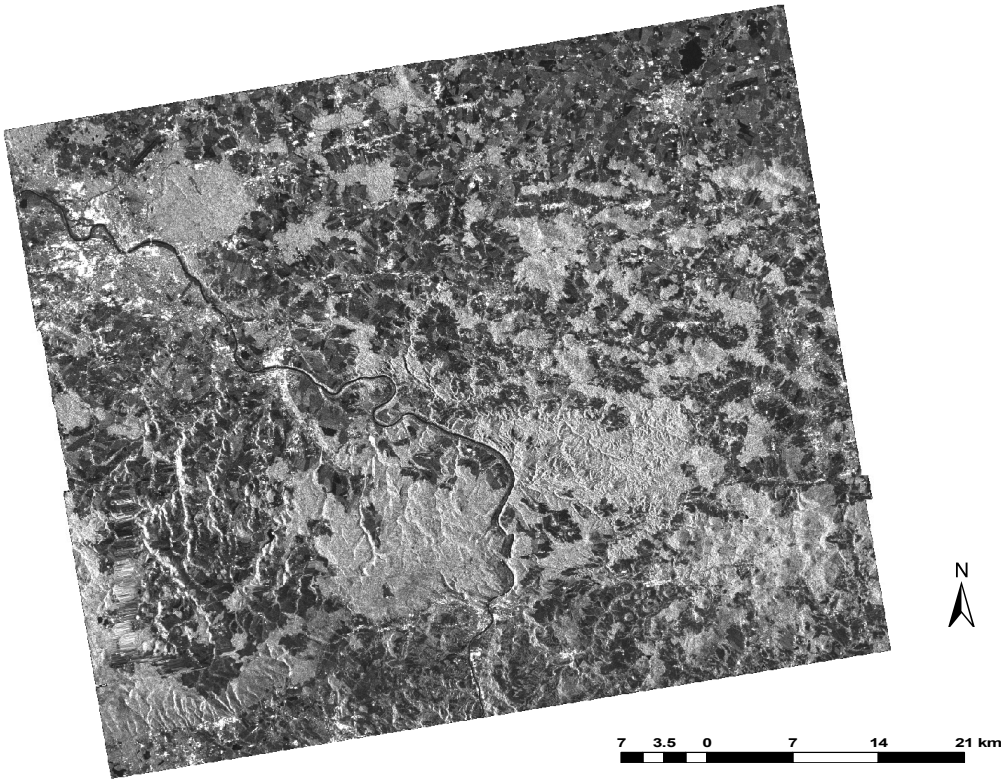

Figure 3.8: ALOS PALSAR Image Acquired on 31.05.2010.

3.2.5 Storage Data

Gottleuba catchment contains five reservoirs: HRB Liebstadt, HRB Friedrichswalde / Ottendorf, TS Gottleuba, HRB Mordgrundbach, and HRB Buschbach. The position of each reservoir, storage data, the max outflow and water elevations were obtained from the *Landestalsperrenverwaltung des Freistaates Sachsen* (LTV) in Pirna, Germany. The main characteristics of these reservoirs are given in Table 3.3 and Figures 3.9 to 3.13.

Table 3.3: Main Characteristics of Gottleuba Catchment Reservoirs.

Reservoir	UTM-WGS 84- Zone 33		Constr. Year	Q max m³/s
	X	Y		
1. HRB Liebstadt	419203	5633826	1967	16
2. HRB Friedrichswalde / Ottendorf	423377	5638470	1970	7
3. TS Gottleuba	424779	5632327	1976	35
4. HRB Mordgrundbach	426298	5629976	1966	5
5. HRB Buschbach	428465	5630960	1963	8.5

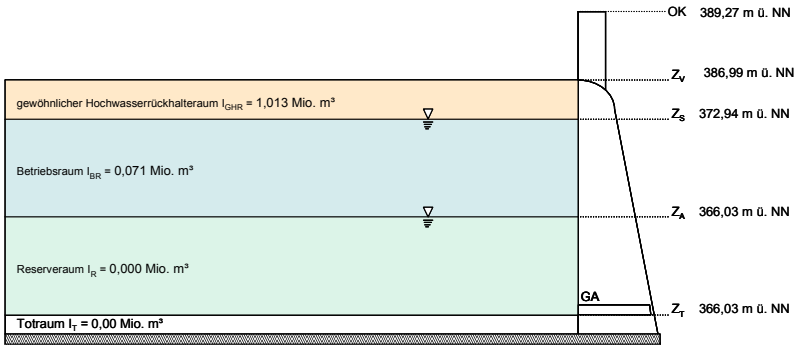

Figure 3.9: HRB Liebstadt Reservoir.

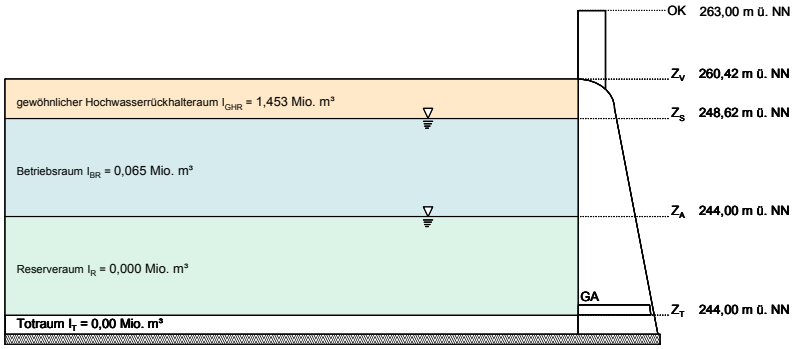

Figure 3.10: HRB Friedrichswalde / Ottendorf Reservoir.

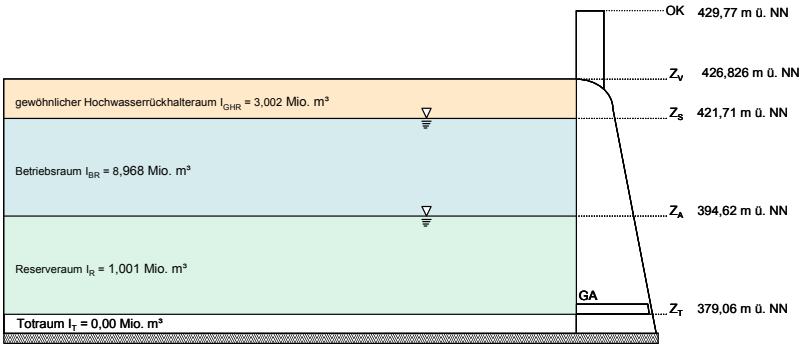

Figure 3.11: TS Gottleuba Reservoir.

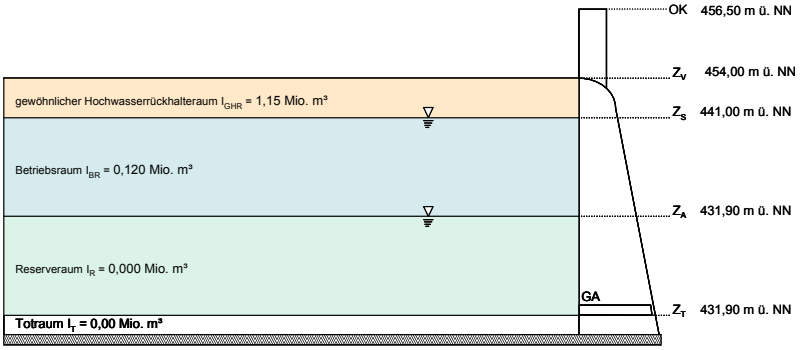

Figure 3.12: HRB Mordgrundbach Reservoir.

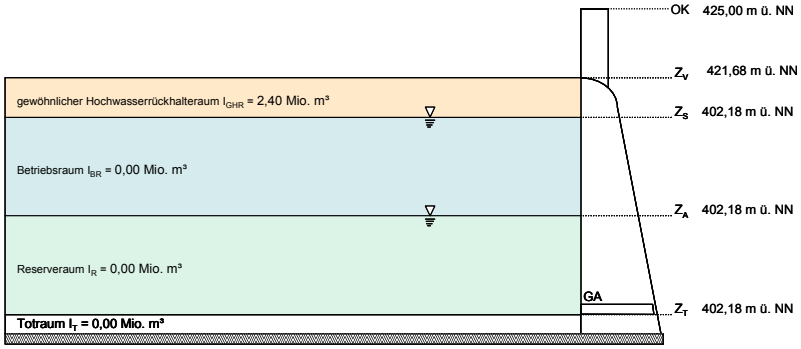

Figure 3.13: HRB Buschbach Reservoir.

3.2.6 Hydrological and Meteorological Data

Discharge data is required for model validation and verification based on the Saxon flood event of 2002. Historical and recent discharge data were obtained from the LfULG. The other additional required data sets are precipitation, global radiation, relative humidity, wind speed, maximum and minimum air temperature were acquired from for the Department of Meteorology, Technical University of Dresden. These data sets extracted and interpolated as daily gridded data of 500m x 500m within the project of *Statistische Untersuchungen regionaler Klimatrends in Sachsen* (CLISAX). The CLISAX record has its origin in the monitoring networks of the *German Weather Service* (DWD) and the Czech. Precipitation map from 11 to 13 August 2002 in Germany is shown in Figure 3.14.

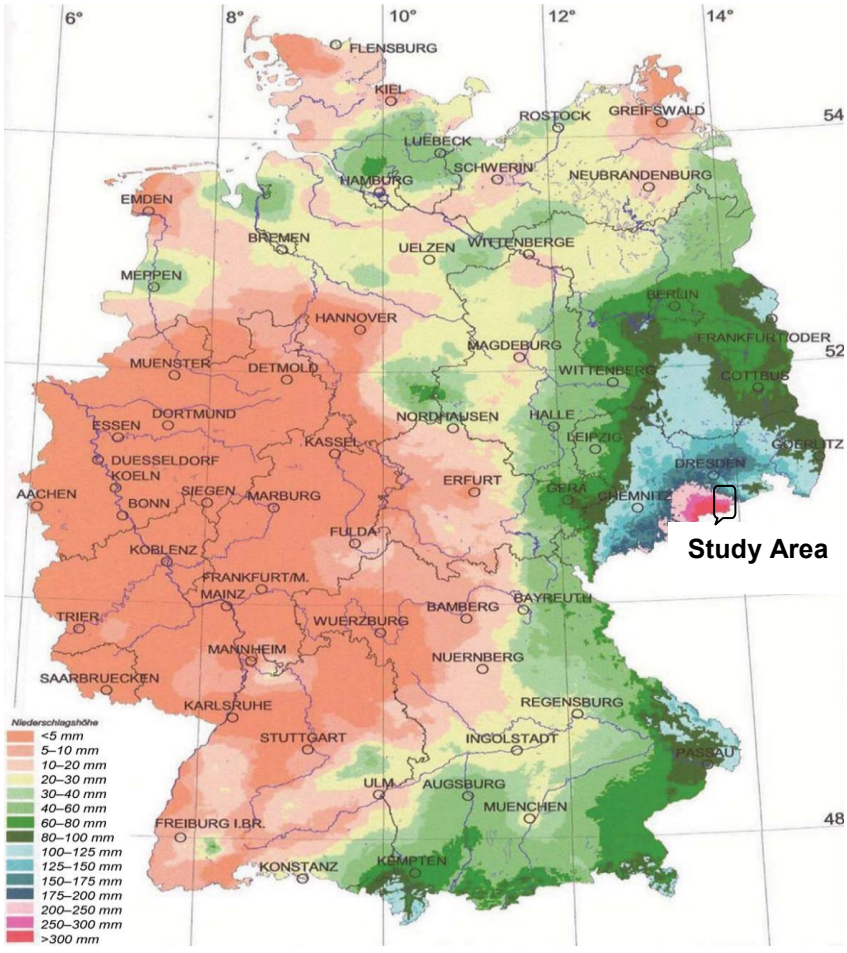

Figure 3.14: Areal Distribution of Precipitation in Germany from 11 to 13 August 2002, (DWD).

3.3 Applied Instruments and Software

3.3.1 Instruments

Field measurements of the volumetric soil moisture were carried out using a Time Domain Reflectometry (TDR - HH2 Moisture Meter) Figure 3.15. The sensor converts the measured dielectric properties into water content over the full range, 0 – 80%, using calibration tables (WET Sensor User Manual, 2005).

Figure 3.15: TDR - HH2 Moisture Meter.

3.3.2 Software

3.3.2.1 ERDAS IMAGINE 9.2

IMAGINE is a remote sensing software with raster graphics editor capabilities, designed by ERDAS for geospatial applications. It has been primarily developed for geospatial raster data processing and allows to prepare, display and enhance digital images for mapping with GIS or in CADD software. It performs advanced remote sensing analysis and spatial modelling to create new information (www3).

3.3.2.2 ASF MapReady 2.3.6

ASF MapReady (Alaska Satellite Facility) is a program for converting SAR data into a GIS-ready image format (GeoTIFF). Also, the SAR data can be geocoded, and/or terrain corrected.

3.3.2.3 ArcMap 9.3

ArcMap is the main component of the ArcGIS of the ESRI suite of geospatial processing programs, and it is used primarily to view, edit, create and analyse geospatial data. ArcMap allows to explore data within a data set, to symbolising features accordingly, and to create maps. In addition, it is possible to create and manipulate data sets to include a variety of information.

3.3.2.4 HEC-HMS 3.4

HEC-HMS is designed to simulate the precipitation-runoff processes of dendritic watershed systems; and applicable to a variety of geographic areas for solving the widest possible range of problems. This includes large river basin water supply and flood hydrology as well as small urban or natural watershed runoff. The program is a generalised modelling system capable of representing many different watersheds (www4).

3.3.2.5 HEC-GeoHM 4.2.93

HEC-GeoHMS uses ArcMap and the Spatial Analyst extension to develop a number of hydrologic modelling inputs for the HEC-HMS. HEC-GeoHMS analyses the digital terrain information and transforms the drainage paths and watershed boundaries into a hydrological data structure that represents the watershed response to precipitation (www5). The applied version of HEC-GeoHMS requires ArcGIS 9.3 with the Spatial Analyst extension.

3.3.2.6 Arc Hydro Tools 1.3

The Arc Hydro Tools (AHT) are a set of public domain utilities developed jointly by the Center for Research in Water Resources of the University of Texas at Austin, and ESRI. They provide functionalities for terrain processing, watershed delineation and attribute management (www6). The Arc Hydro Tools 1.3 require ArcGIS 9.2/9.3 with the Spatial Analyst extension and the Water Utilities Application Framework (ApFramework).

3.3.2.7 BROOK90 ver 4.4e

The BROOK90 software is designed for evaporation, soil water and stream flow simulation. BROOK90 simulates the water budget on a unit land area at a daily time step and is applicable to all land surfaces. Input of daily precipitation and maximum and minimum temperatures is required, and daily solar radiation, vapor pressure, and wind speed are desirable (www7).

3.4 Research Methods

DTM data are widely applied to delineate watershed boundaries and stream networks. A GIS provides a flexible environment to enter, analyse, and display digital data from various sources necessary for feature identification, change detection, and database development. In the present study, GIS will be employed to organise and process elevation data.

The methodology of this research consists of three main parts, which are summarised in Figure 3.16. The first part describes how to delineate the Gottleuba watershed boundaries and its drainage networks using RS and GIS tools. The second part clarifies the use of SAR techniques to derive the soil moisture content corresponding to the degree of saturation in the near surface soil layer. In the last part the extracted watershed characterisation, meteorological data and the hydrological parameters including the derived soil moisture will be applied to drive the runoff model by means of automated hydrological processing (HEC-HMS) model.

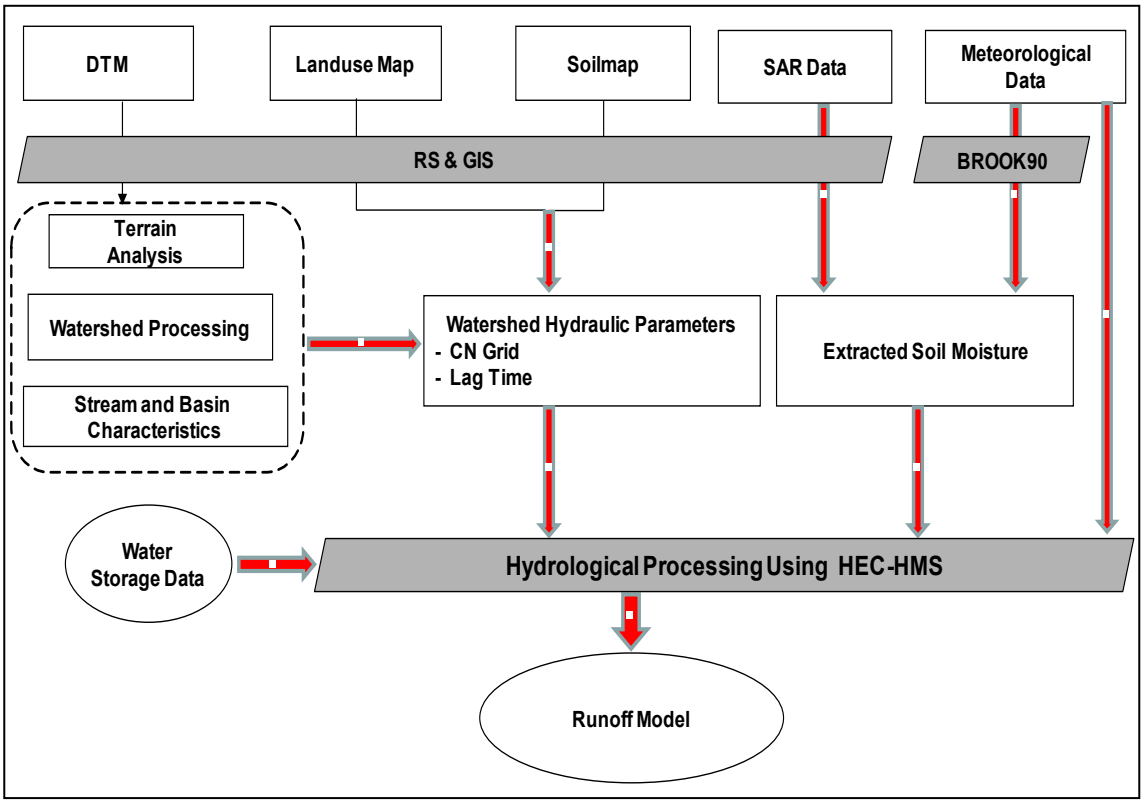

Figure 3.16: Methodology Scheme.

Chapter 4: Procedure of Application

In this chapter, the generation of the Gottleuba Watershed, the hydrologic parameters estimation, the extraction of the surface soil moisture content from spaceborne SAR data, and the setting-up of the hydrological model to implement the rainfall runoff transformation process are presented in details.

4.1 Watershed Generation

The functions for hydrological analysis materialised in different software packages are relatively similar. The Geospatial Hydrologic Modelling HEC-GeoHMS and AHT extensions of ArcMap are popular software packages. They use ArcMap and its Spatial Analyst extension to input a number of data for hydrological modelling. The HEC-GeoHMS and the AHT analyse the digital terrain information and transform the drainage paths and watershed boundaries into a hydrological data structure that represents the watershed response to precipitation. The HEC-GeoHMS can also transform the drainage paths and watershed responding to precipitation.

4.1.1 Terrain Preprocessing

Terrain Preprocessing uses a DTM to identify the surface drainage pattern. Once preprocessed, the DTM and its derivatives can be used for efficient watershed delineation and stream network generation (AHT, Tutorial, 2009).

The first step in watershed delineation is the DTM reconditioning using the drainage network topographic dataset and the high resolution ALS-DTM 2m in the AHT.

4.1.1.1 DTM Reconditioning

This function modifies a DTM by super imposing linear features onto it (burning/fencing). It is an implementation of the AGREE method developed Center for Research in Water Resources at the University of Texas at Austin. By DTM reconditioning the degree of agreement between stream networks delineated from the DTM and the input vector stream networks can be increased (AHT, Tutorial, 2009). The output is a reconditioned AGREE-DTM.

4.1.1.2 Filling the Sinks

The second step in the watershed delineation is to “hydrologically correct” the raw DTM by filling sinks. The Fill Sinks function fills the sinks in a grid. If cells with higher elevation surround a cell, the water is trapped in that cell and cannot flow. The Fill Sinks function modifies the elevation value to eliminate these problems as shown in Figure 4.1. The resulting grid is essentially a smoothed DTM in which extreme topographic differences are filled in (Hydro DTM).

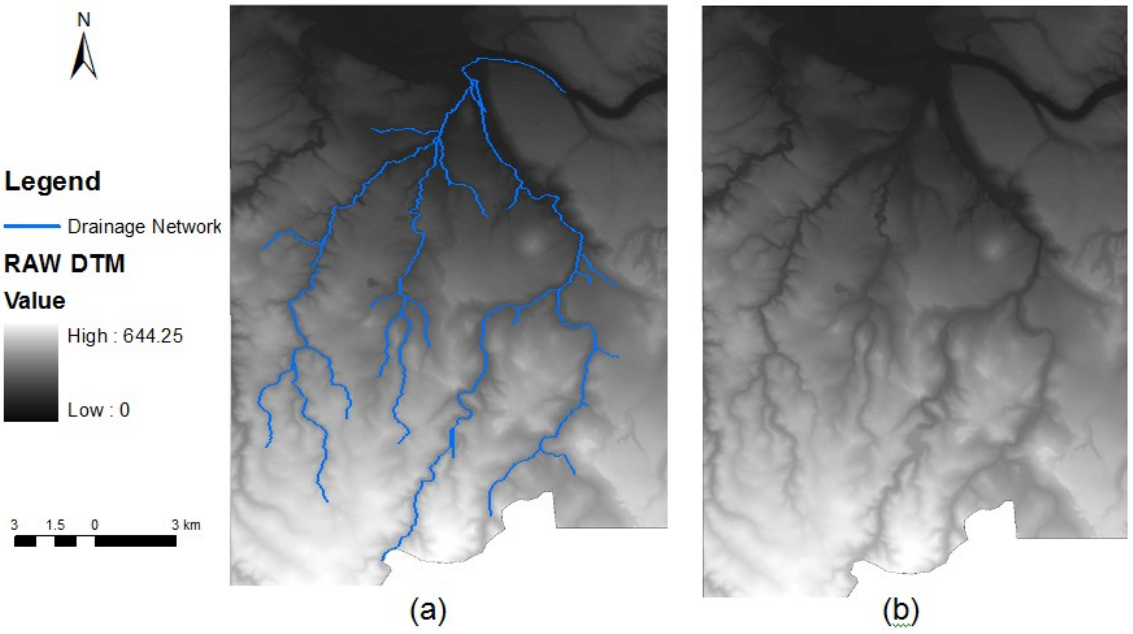

Figure 4.1: a) Raw DTM and Drainage Network Topographic Dataset, b) Fill Sink AGREE-DTM (Hydro DTM).

4.1.1.3 Flow Direction

This process computes the flow direction for the Hydro DTM. The values in the cells of the flow direction grid indicate the direction of the steepest descent from that cell. Water flows to one of its neighbouring according to the direction of the steepest descent. Flow direction takes one out eight possible values. The eight-direction pour point algorithm (D-8) assigns the flow direction code to each cell, based on the steepest downhill slope as defined by the Hydro DTM, (see Figure 4.2).

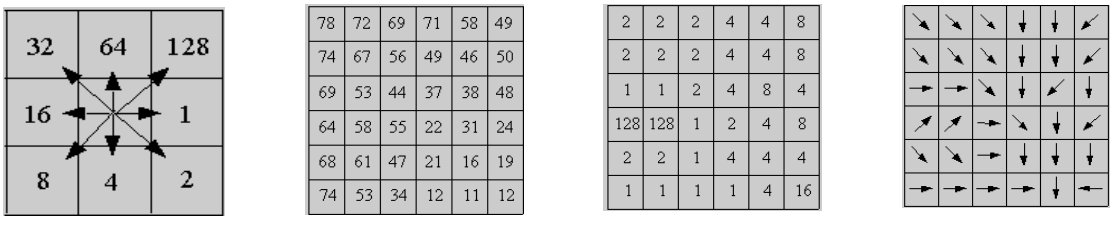

a) Coding for flow directions | b) Hydro DTM | c) Flow direction grid | d) Representation of flow directions

Figure 4.2: Raster-Based Functions for Terrain Analysis for Hydrological Purposes (www8).

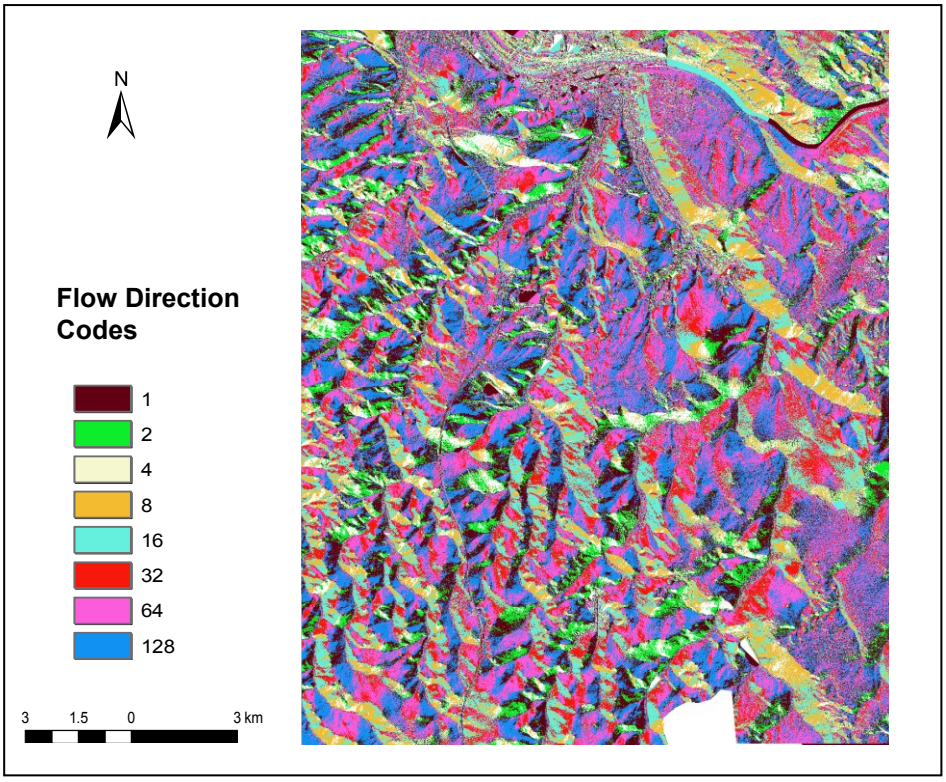

Figure 4.3: Flow Direction of Gottleuba Catchment.

For distributed hydrological models which require a square grid to support physiographic data and rely on a continuous drainage network where each grid cell must be directly connected to one, and only one, of its neighbouring cells, the eight flow directions (D8) represent a valid approach to model the watershed drainage structure (Tribe, 1992). Figure 4.3 shows the flow network direction of the Gottleuba catchment.

4.1.1.4 Flow Accumulation

Flow accumulation is the process of measuring the drainage area in units of grid cells. The flow accumulation grid that contains the accumulated number of cells upstream of a cell, for each cell in the input grid is computed (Figure 4.4). The resulting raster essentially indicates the drainage network.

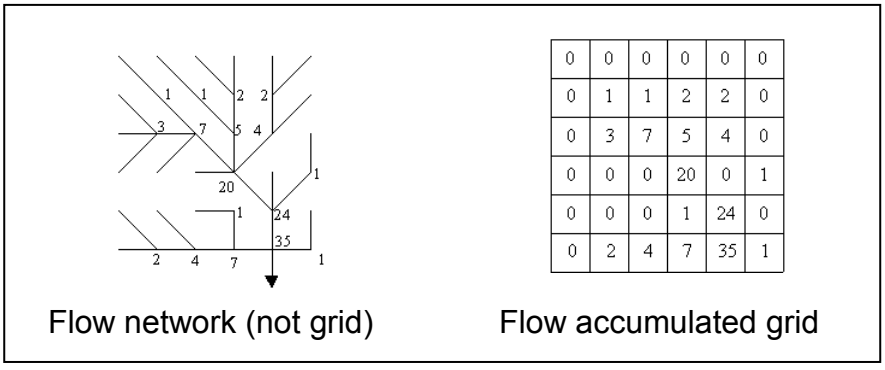

Figure 4.4: Flow Accumulation Procedure (www8).

4.1.1.5 Stream Definition

This step computes a stream grid which contains a value of "1" for all the cells in the input flow accumulation grid that have a value greater than the given threshold. All other cells in the stream grid contain no data.

4.1.1.6 Stream Segmentation

The purpose of this task is to create a grid of stream segments that have a unique identification. Either a segment may be a head segment, or it may be defined as a segment between two segment junctions. All the cells in a particular segment have the same grid code that is specific to that segment.

4.1.1.7 Catchment Grid Delineation

This is to create a grid in which each cell carries a value (grid code) indicating to which catchment the cell belongs. The value corresponds to the value carried by the stream segment or sink link that drains that area, defined in the input stream segment link grid (Stream Segmentation) or sink link grid (Sink Segmentation).

4.1.1.8 Raster to Vector Conversion

The grids of stream links and watersheds are vectorised to obtain stream lines and watershed polygon datasets. The three processes Catchment Polygon Processing, Drainage Line Processing and Adjoint Catchment Processing convert the raster data developed so far to vector format.

Catchment Polygon Processing

This function converts a catchment grid it into a catchment polygon feature.

Drainage Line Processing

Drainage Line Processing converts the input Stream Link grid into a Drainage Line feature class.

Adjoint Catchment Processing

This function generates the aggregated upstream catchments from the Catchment feature class. For each catchment that is not a head catchment, a polygon representing the whole upstream area draining to its inlet point is extracted. This feature is used to speed up the point delineation process.

Figures 4.5 and 4.6 show the use of the previous three processes to delineate the Gottleuba Catchment and the drainage network.

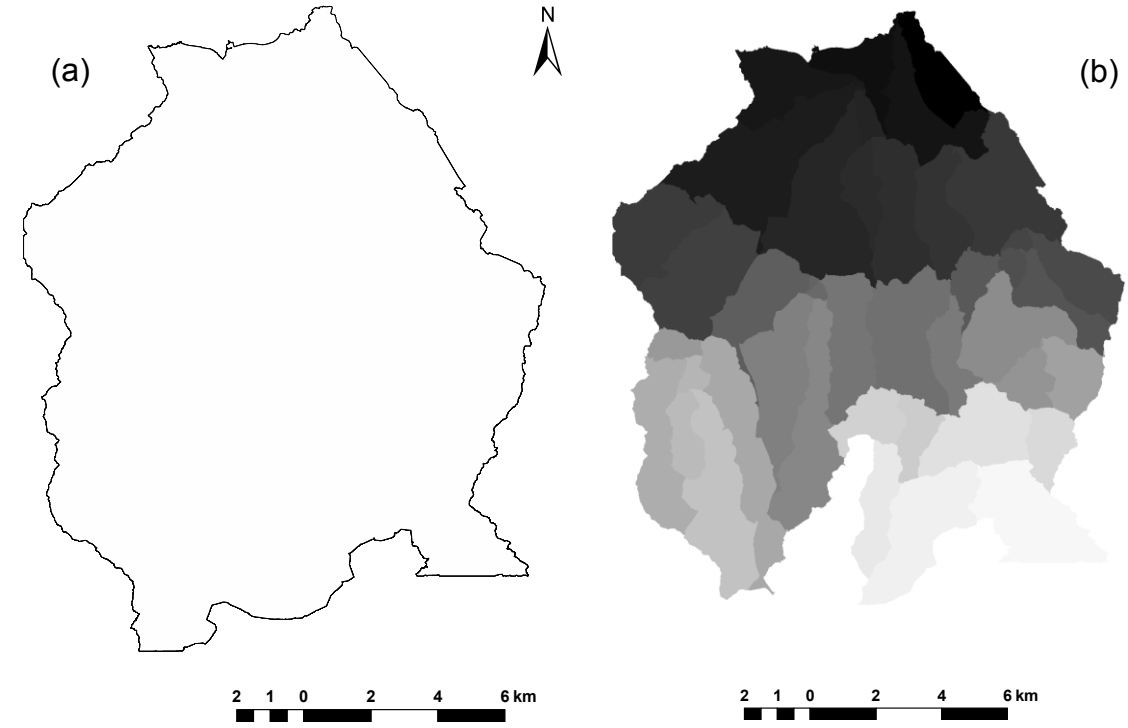

Figure 4.5: a) the Gottleuba Adjoint Catchment, b) the Extracted Sub-Catchments in Raster Format.

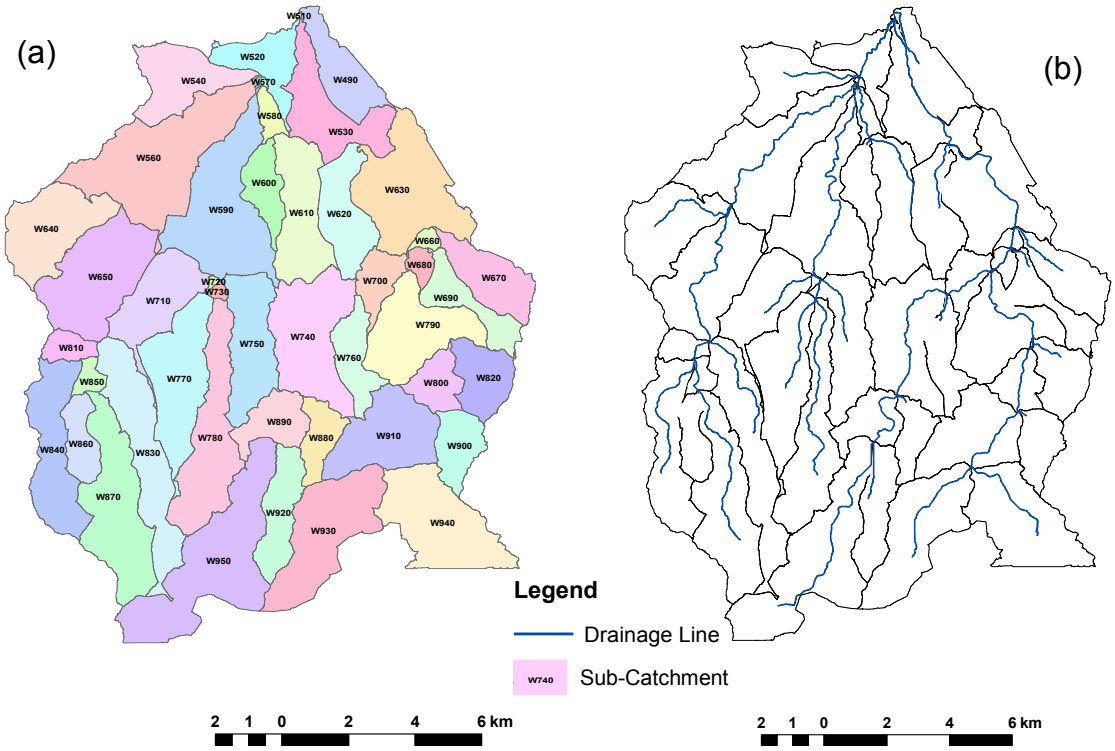

Figure 4.6: a) Delineated Sub-basin Polygons, b) Stream Network after Vectorisation.

4.1.1.9 Drainage Point Processing

This function allows generating drainage points associated with individual catchment Figure (4.7).

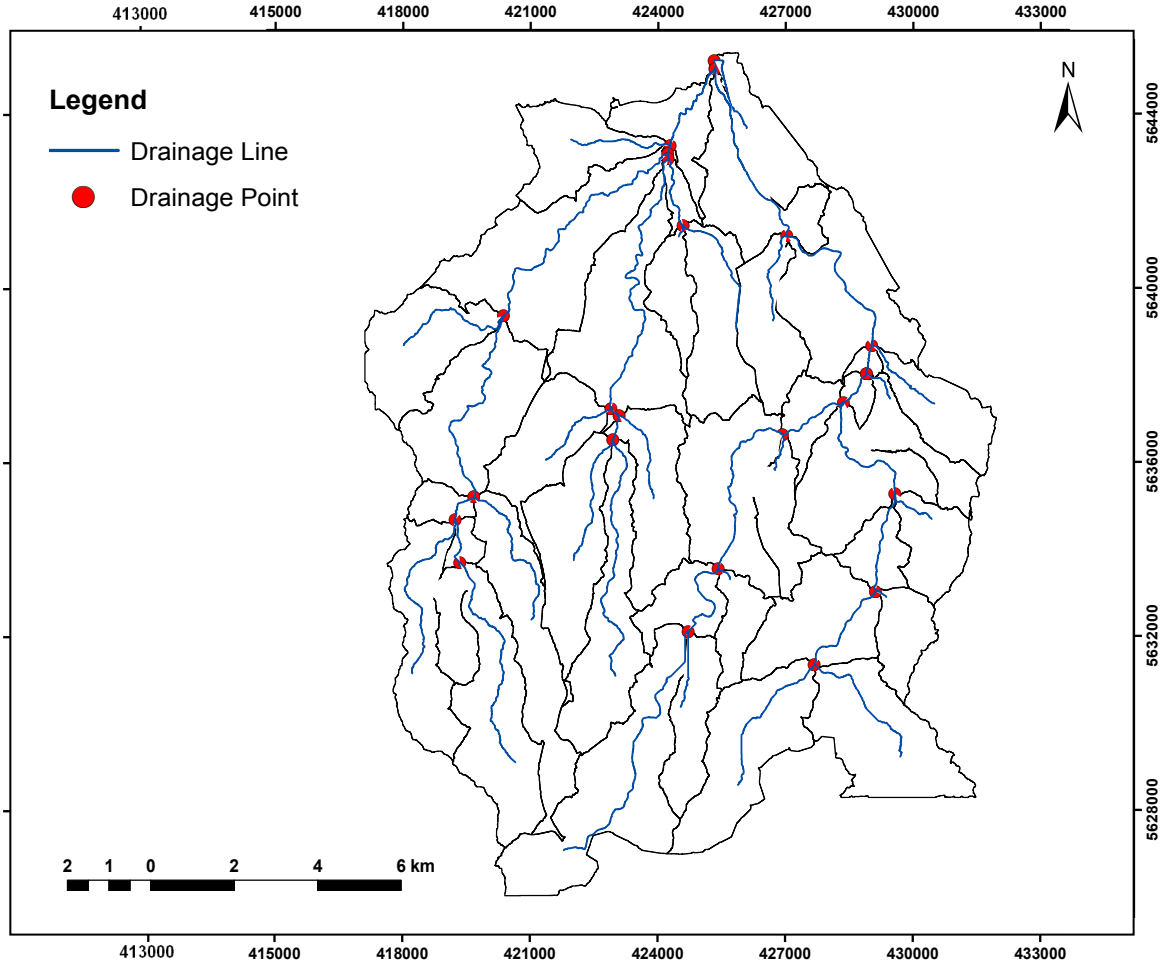

Figure 4.7: Delineated Drainage Points.

4.1.2 Watershed Processing

4.1.2.1 Watershed Outlet Determination

This aim of this process is to locate the outlet of the watershed, which is located at the junction of the Gottleuba River and the Elbe (mouth of the Gottleuba Catchment).

4.1.3 Stream and Basin Characteristics

The basin characteristics determine the physical parameters of streams and sub-basins. The main basin characteristics are:

1. River length.

2. River slope.
3. Basin slope.
4. Longest flow path.
5. Basin centroid.
6. Basin centroid elevation.
7. Centroidal flow path.

The extracted physical parameters were converted into attribute data and listed as shown in Table 4.1. The basin characteristics are illustrated in Figure 4.8.

Table 4.1: Physical Characteristics of Stream Network.

Attributes of Gottleuba River

HydroID	NextDownID	DrainID	Slp	ElevUP	ElevDS	RivLen
2	-1	50	0.00615	115.97	115.89	13
3	2	51	0.00645	117.51	115.97	238.83
4	2	50	0.00527	128.8	115.97	2432.57
5	3	52	0.0078	140.15	117.51	2902.94
6	5	54	0.01177	173.16	140.15	2804.54
7	5	57	0.00199	140.56	140.15	206.51
8	7	57	0.01061	141.88	140.56	124.43
9	8	58	0.01614	175.95	141.88	2111.43
10	3	53	0.00524	145.8	117.51	5398.82
11	9	60	0.02101	182.97	175.95	334.09
12	7	56	0.01205	228	140.56	7254.73

Record: 1 Show: All Selected Records (0

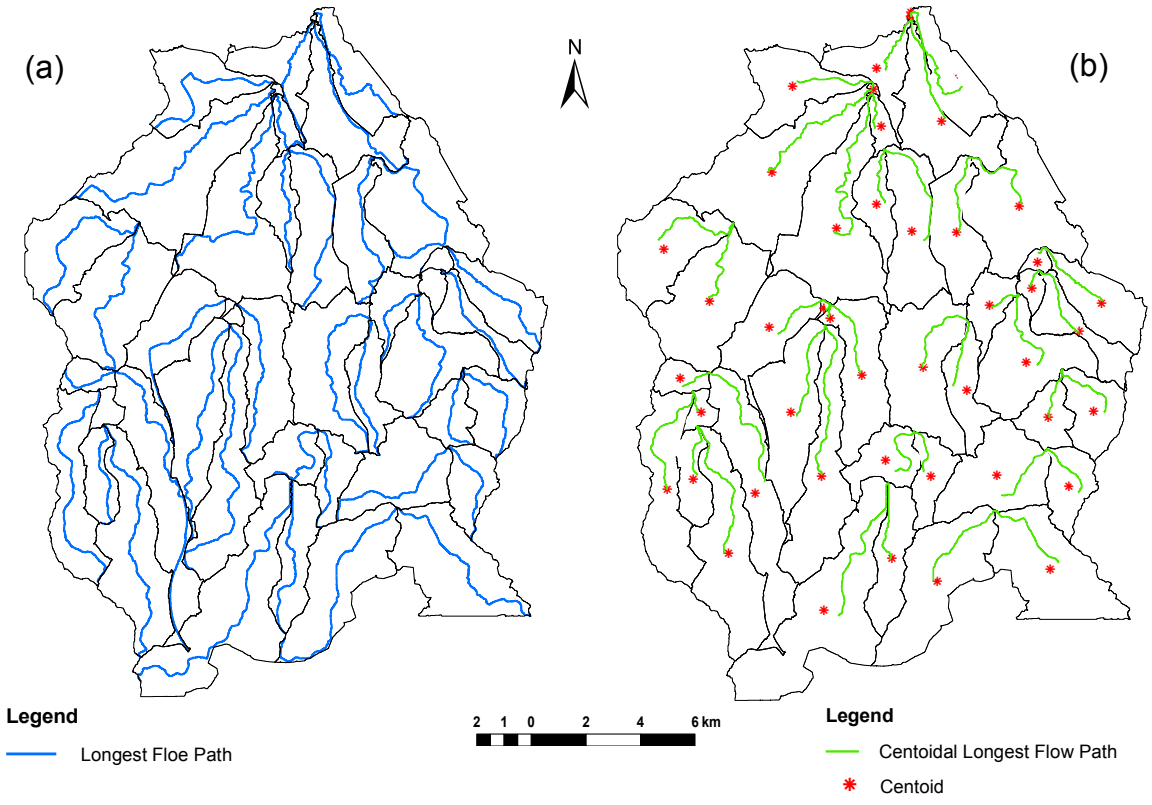

Figure 4.8: Longest Flow Path (a), and Centroid Points along Longest Flow Path (b).

4.2 Estimation of Hydrological Parameters

4.2.1 Curve Number

The Curve Number (CN) provides a simple and robust means of estimating excess rainfall (King et al., 1999), which is a dimensionless watershed parameter, ranging from 0 to 100. A CN of 100 represents the limiting condition of a perfectly impermeable watershed with zero retention and thus all the rainfall becoming runoff. A CN of zero conceptually represents the other extreme, with the watershed abstracting all rainfall with no runoff regardless the amount of rainfall (Gumbo et al., 2001). Curve numbers have been calibrated, evaluated, and assigned for many sets of measured runoff data and are known to be generally reliable over a wide range of geographic, soil, and land management conditions.

The Soil Conservation Service (SCS-CN) method which has been applied in this research is a simple, widely used and efficient method to determine the approximate amount of runoff from a rainfall even in a particular area. Runoff CN is a key factor in determining runoff in the hydrological modelling based on the SCS-CN, method (USDA, 1986). Although the method is designed for a single storm event, it can be scaled to find average annual runoff values. The statistical requirements for this method are very low: rainfall amount and curve number. The curve number is based on the area's Hydrologic Soil Group (HSG), landuse, treatment and hydrological condition. Runoff curve numbers are a set of standard empirical curves that are used to estimate storm water runoff.

There exist two ways to calculate runoff, the composited and distributed method. The composited method finds the area-weighted average curve number and the basin averaged curve number is used to calculate the runoff. The distributed method calculates the runoff for each hydrological runoff group in the drainage basin and adds the runoff. Originally, when paper and pencil or calculators were the common tools for calculation, the composited method was used because there are fewer computational steps. With the advent of GIS and spread sheets, the distributed method is nearly as easy to use once the formulas for the drainage basin are developed. The two methods do not produce the same runoff result because the relationship between runoff and curve number is not linear (Grove et al, 1998). The average curve number for a basin tends to be closer to the lower curve numbers in the basin than to the higher curve numbers. The U.S. Natural Resources and Conservation Service standard approach is the composited method. The general equation for the SCS-CN method is shown in Equation (1).

$$\mathbf{Q} = \frac{(\mathbf{P} - \mathbf{0.2\,S})^2}{(\mathbf{P} + \mathbf{0.8\,S})} \qquad (1)$$

$$\mathbf{S} = \frac{\mathbf{1000}}{\mathbf{CN}} - \mathbf{10} \qquad (2)$$

where: S = the potential maximum retention in meters,
P = rainfall depth in millimeters, and
Q = runoff depth in millimeters.

The parameter CN in Equation (2) is a transformation of S, and it is used to perform interpolating, averaging, and weighting operations more linear. With the nomogramme shown in Figure 4.9 the amount of runoff can be found once the rainfall amount and the curve number are known.

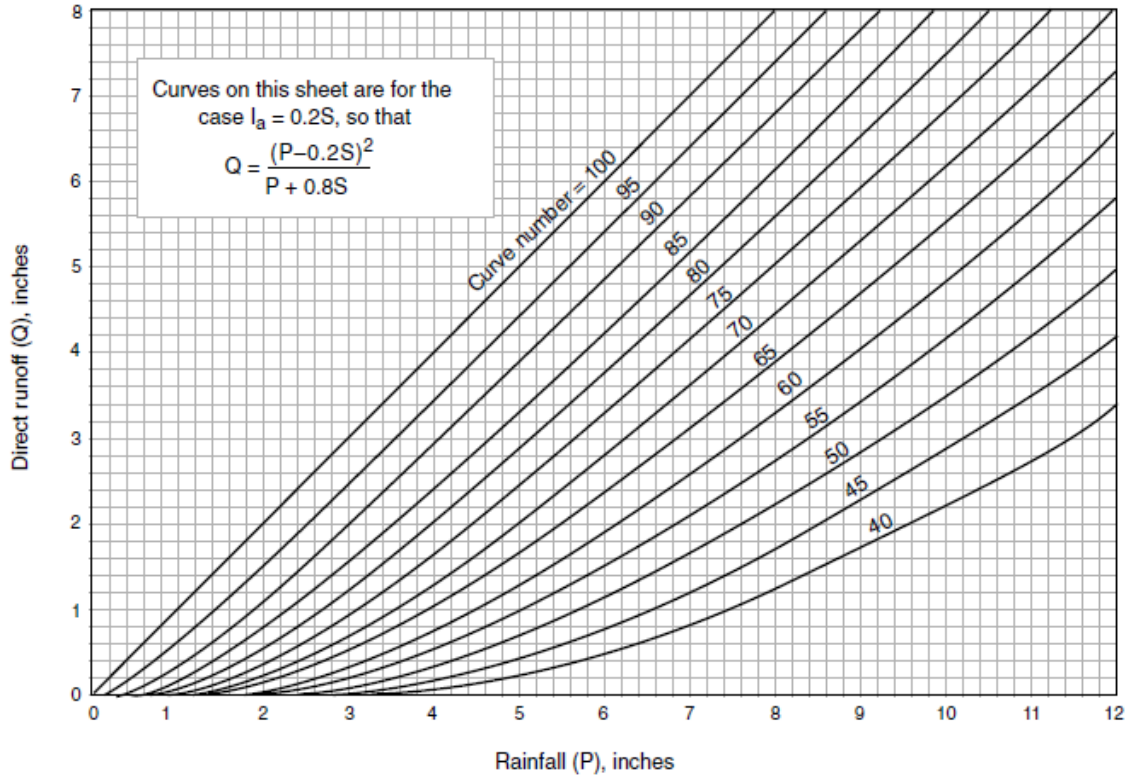

Figure 4.9: Range of CN's and Rainfall Chart (from Technical Release 55 (TR 55)).

4.2.1.1 Hydrological Soil Groups

Soilmap and landuse were required as spatial characterisations to define the CN values which were applied in the Rainfall Runoff Model. Table 4.2 illustrates the CN values based on HSG and landuse description. Using a GIS the original soilmap (Figure 3.5) was reclassified based on the SCS-CN method as a HSG; A, B, C and D to their stormwater runoff potential from low for ‘‘A’’ soil type to high ‘‘D’’ soil type based on the physical soil characteristics following the USDA (1985) method. The reclassified soilmap is shown in Figure 4.10.

Group A

Soils have low runoff potential, and high infiltration rates even when thoroughly wetted (greater than 0.30 in/hr). They consist mainly of deep, well to excessively drained sands or gravels. This group also includes sand, loamy sand, and sandy loam that have experienced urbanisation but have not been significantly compacted.

Group B

Soils have moderate infiltration rates when thoroughly wetted (0.15- 0.30 in/hr). They consist mainly of moderately deep to deep, moderately well to well-drained soils with moderately fine to moderately coarse textures. This group also includes, silt loam and loam that have experienced urbanisation but have not been significantly compacted.

Group C

Soils have low infiltration rates when thoroughly wetted (0.05-0.15 in/hr). They consist mainly of soils with a layer that impedes downward movement of water and soils with moderately fine to fine texture. This group also includes sandy clay loam that has experienced urbanization but has not been significantly compacted.

Group D

Soils have high runoff potential. They have very low infiltration rates when thoroughly wetted (0-0.05 in/hr). They consist mainly of clay soils with high swelling potential, soil with permanent high water tables, soils with clay pans or clay layers at or near the surface, and shallow soils over nearly impervious material. This group also includes clay loam, silty clay loam, sandy clay, silty clay and clay that have experienced urbanisation but have not been significantly compacted.

Table 4.2: Description and Curve Numbers (from TR-55).

Landuse Description	Cover Description		Curve Number for HSG			
	Cover Type and Hydrologic Condition	Impervi-ous Areas %	A	B	C	D
Agricultural	Row Crops - Straight Rows + Crop Residue Cover - Good Condition		64	75	82	85
Commercial	Urban Districts: Commercial and Business	85	89	92	94	95
Forest	Woods - Good Condition		30	55	70	77
Grass/Pasture	Pasture, Grassland, or Range -Good Condition		39	61	74	80
High Density Residential	Residential districts by average lot size: 118 acres or less	65	77	85	90	92
Industrial	Urban district: Industrial	72	81	88	91	93
Open Spaces	Open Space (lawns, parks, golf courses, cemeteries, etc.) Fair Condition (grass cover 50% to 70%)		49	69	79	84
Parking and Paved Spaces	Impervious areas: Paved parking lots, roofs, drive ways, etc. (excluding right-of-way)	100	98	98	98	98
Water/ Wetlands		0	0	0	0	0

The hydraulic condition is based on combination factors that affect infiltration and runoff, including (a) density and canopy of vegetative areas, (b) amount of year-round cover, (c) amount of grass or close-seeded legumes, (d) percent of residue on the land surface (good >= 20%), and (e) degree of surface roughness. In Table 4.2, the land cover Forest in good condition means that the woods are protected from grazing, and litter and brush adequately cover the soil. The Grass/Pasture is in good condition when more than 75% ground is covered by grass and lightly or only occasionally grazed.

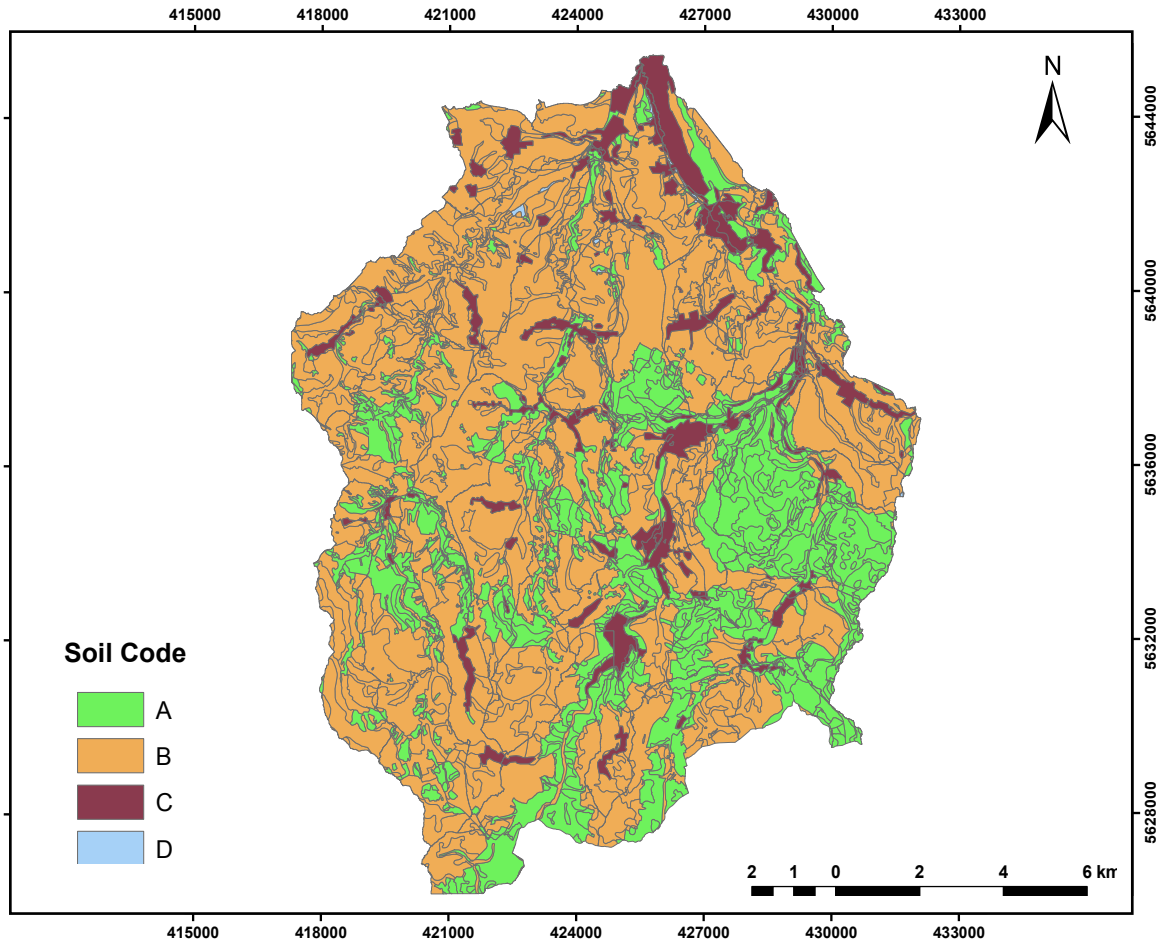

Figure 4.10: Reclassified Soil Map of Gottleuba Catchment.

For a watershed with sub-basins of different soil types and land cover types, a composite curve number *CNc* is determined (Equation 3) by weighting the CNs for the different sub-areas in proportion to the total land area associated with each A_i (i= 1,2 , 3, ... n).

CNc = CN1 (A1/Atotal) + CN2 (A2/Atotal) + ……. + CNn (An/Atotal) (3)

By using the presented landuse classes in Figure 3.4 and the reclassified soil map in conjunction with SCS-CN, the curve number grid (Figure 4.11) were created by means of the HEC Geo-HMS extension in ArcMap.

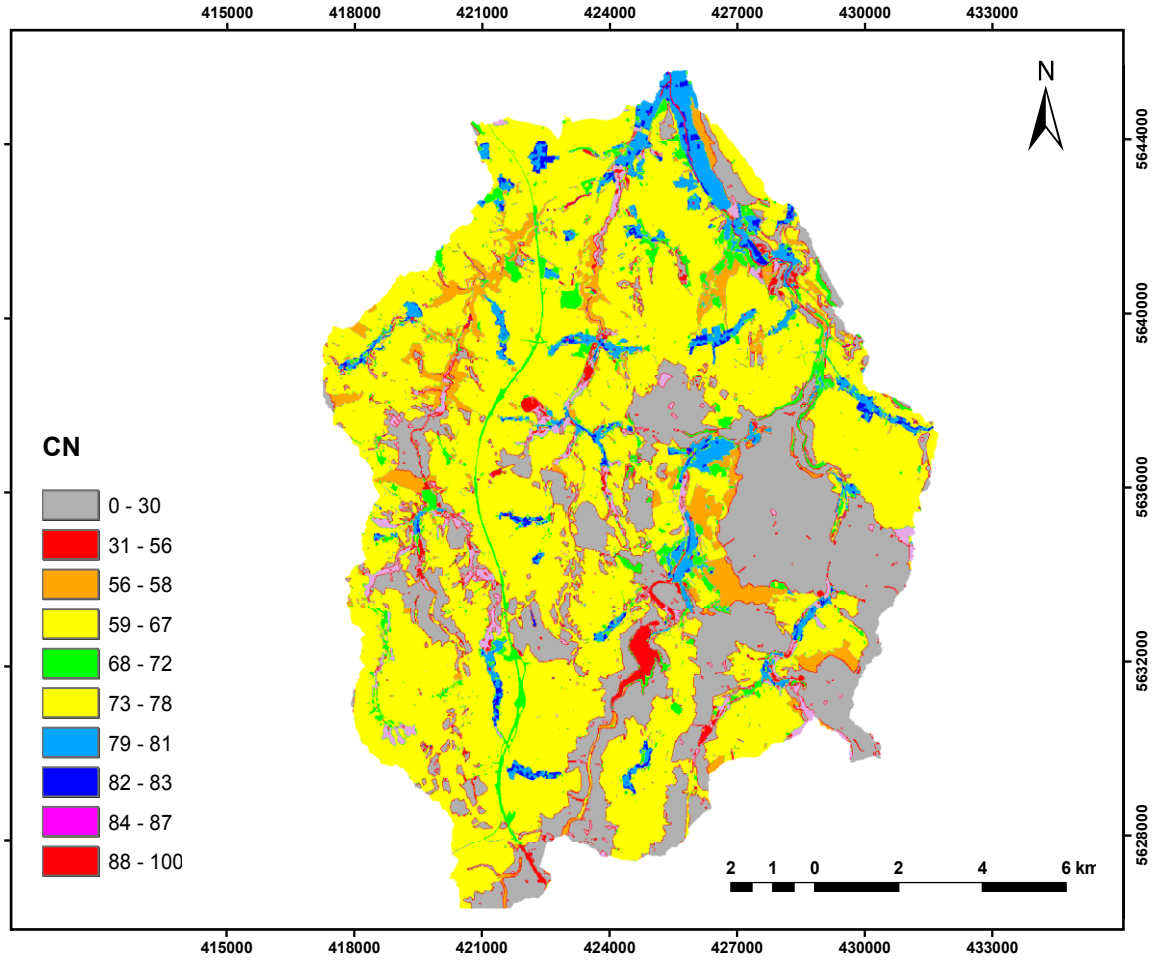

Figure 4.11: Extracted CN Grid Values.

4.2.2 Lag Time

Watershed lag time (L_t) is the time from the midpoint of rainfall excess to the peak of the unit hydrograph (ASCE, 2006) as shown in Figure 4.12.

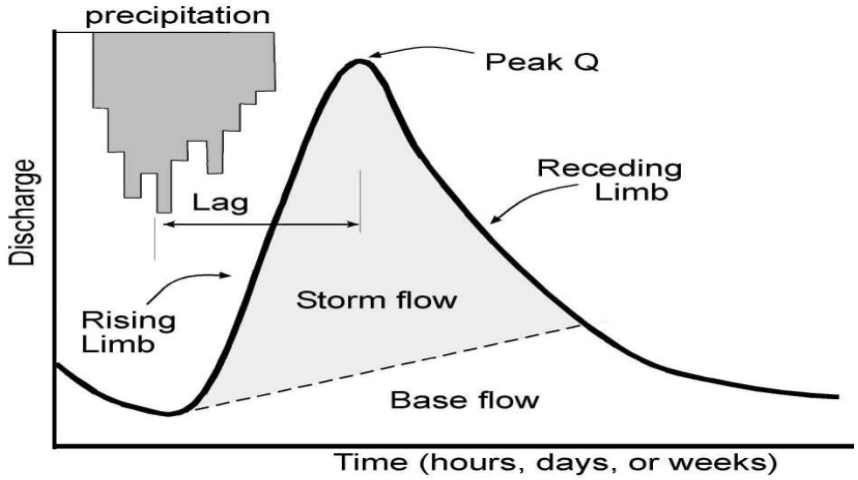

Figure 4.12: Hydrograph (from ASCE, 2006).

The unit hydrograph represents the time distribution of runoff as a result of one inch of effective rainfall uniformly distributed over a basin for a specified duration, (ASCE, 1996). Equation (4) illustrates that the lag time parameter is a function of the hydraulic length, the potential maximum retention, and watershed slope. Table 4.3 shows the BasinLag field in the sub-basin feature class populated with numbers that represent basin lag time in hours. Also Figure 4.13 shows the feature values of the sub-basin Lag time.

$$L_t = L^{0.8} \frac{(S+1)^{0.7}}{1900\ (w_s)^{0.5}} \qquad (4)$$

where: L_t is the lag time parameter,
L is the watershed hydraulic length,
w_s is the average watershed slope, and
S is the potential maximum retention calculated from Equation (2).

Table 4.3: Attribute Values of the Hydrologic Parameters of Gottleuba Subbasins.

Attributes of Gottleuba-Subbasins

Shape *	GRIDCODE	Shape_Length	Shape_Area	BasinCN	BasinLag	HydroID	DrainID
Polygon	2	15492	3688064	67.83	1.17	50	50
Polygon	3	1076	25716	81.7	0.2	51	51
Polygon	4	16776	3164868.000001	76.71	1.62	52	52
Polygon	5	22884	5358256.000001	73.44	2.07	53	53
Polygon	6	16680	4645180.000001	76.58	1.58	54	54
Polygon	8	29024	11094312	73.74	2.05	56	56
Polygon	9	2312	83448	70.05	0.28	57	57
Polygon	10	7216	863104	73.9	0.73	58	58
Polygon	11	26056	9430960	73.23	1.82	59	59
Polygon	12	11644	2379955.999999	73.1	0.99	60	60
Polygon	13	17640	5582496.000001	58.97	1.79	61	61
Polygon	14	15296	4298084	71.85	1.16	62	62
Polygon	15	24100	8571856	67.62	1.41	63	63
Polygon	16	16572	5971475.999998	72.59	1.12	64	64
Polygon	17	18468	7990784	62.7	1.41	65	65
Polygon	18	4484	428348	68.33	0.36	66	66
Polygon	19	13984	3852364	74.22	0.86	67	67
Polygon	20	5620	704380	49.2	0.71	68	68
Polygon	21	16740	2932880.000001	74.51	0.79	69	69
Polygon	22	11168	1983004	48.31	1.06	70	70

Record: 0 Show: All Selected Records (0 out of 45 Selected) Options

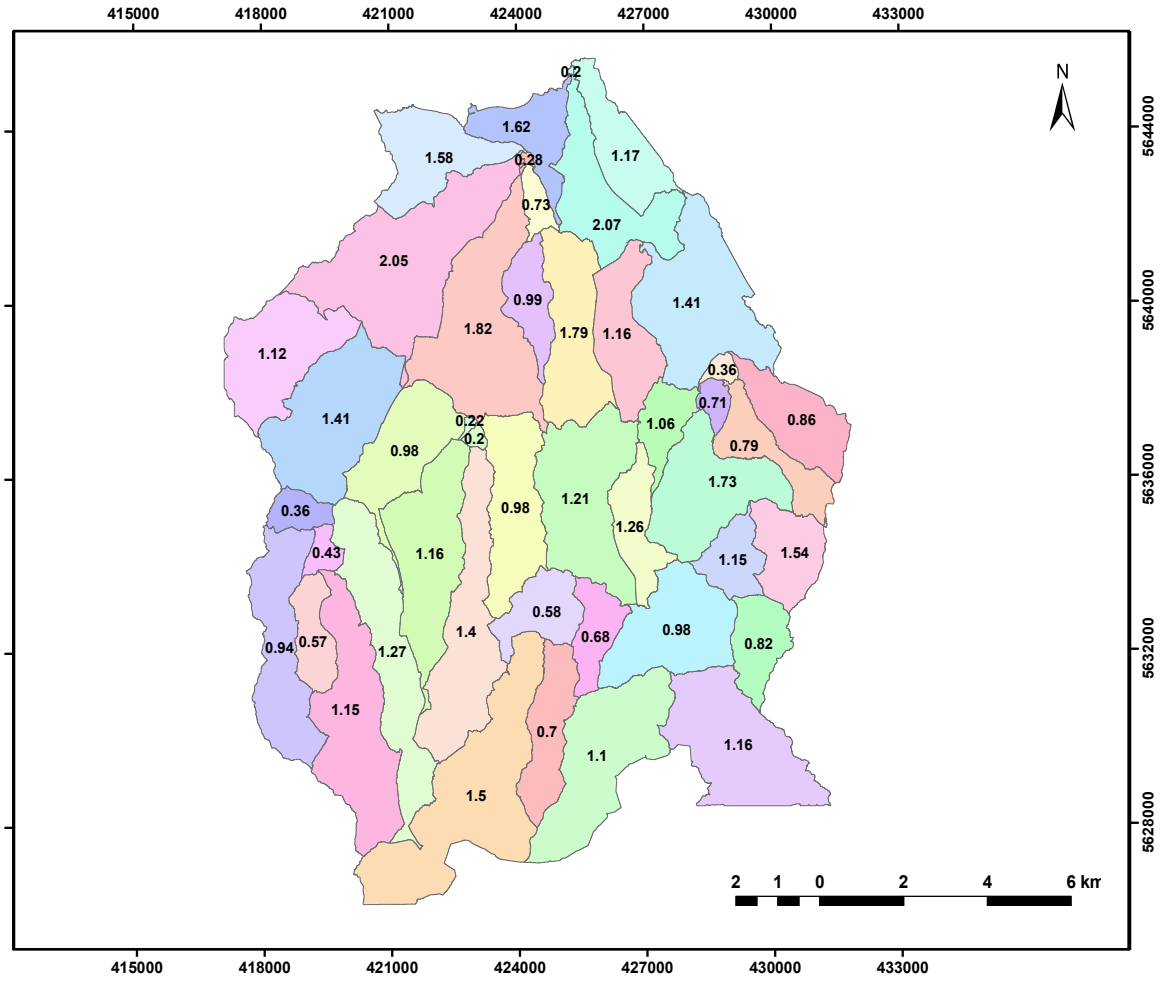

Figure 4.13: Extracted Sub-basin Lag Time Values.

4.3 Soil Moisture Extraction

Soil moisture is an important and very dynamic state variable of the hydrological cycle. The knowledge of its magnitude and dynamics is crucial for studying and modelling important processes at the earth surface. Therefore, the estimation of SM by means of remotely sensed observations is very attractive to domains like hydrology, agronomy or meteorology (Engman, 1991). In microwave remote sensing, the study of how the microwaves interact with the earth terrain has always been interesting for interpreting satellite SAR images (Albert et al. 2005). Microwave remote sensing holds great promise for hydrology because the primary physical property that affects the measurement is directly dependent on the amount of water present in the soil (Jackson & Schmugge, 1989).

Soil moisture plays a critical role in the surface energy balance at the soil-atmosphere interface and is a key state variable that influences the redistribution of the radiant energy and the runoff generation and percolation of water in soil. Local measurements of Soil Moisture Content (SMC) are strongly affected by spatial variability, besides being time consuming and expensive. Moreover, the use of hydrological models for extending the forecast of soil moisture over larger areas is not easy, and depends on the homogeneity of the selected areas and the information available about them (soil properties, i.e. hydraulic characteristics, and permeability, together with meteorological and climatological data, etc.).

The possibility of measuring soil moisture on a large scale from satellite sensors, with complete and frequent coverage of the Earth's surface is therefore extremely attractive. The sensitivity to SMC of the radar backscattering coefficient (σ°), measured at low microwave frequencies is a well-known phenomenon, already investigated by many scientists. Indeed, research activities carried out worldwide in the past have demonstrated that sensors operating in the low frequency portion of the microwave electromagnetic spectrum (P- to L-band) are able to measure the moisture of a soil layer, the depth of which depends on soil characteristics and moisture profile, and is of the order of some tenths of the wavelength. The most significant information was obtained by combining different frequencies, polarizations, and incidence angles (Dubois, 1995; Benallegue, 1995; & Macelloni, 1999).

4.3.1 Influences on the Radar Backscatter Signal

The backscatter signal is dependent on various elements: it is influenced by the radar properties itself, like wavelength, depression angle and polarisation, and terrain properties like the dielectric material properties, its surface roughness and the feature orientation.

The dielectric constant of a material has strong influence on electromagnetic energy, especially at radar wavelengths. If the moisture content of a material increases, the dielectric constant also increases which then results in a different

backscatter signal. High moisture produces a high backscatter which in turn leads to a bright image signature.

Radar could therefore be used for the estimation of soil moisture, but as it is influenced by other factors as well, this estimation tends to be difficult. Another influence is given by the roughness of an object in comparison with the wavelength of the radar beam. The backscatter signal is determined by the average surface roughness of a ground resolution cell. As a natural surface is a complex structure it is difficult to characterise them mathematically. In total three roughness categories are distinguished: smooth surface, intermediate roughness and rough surface. On a smooth surface the radar beam will be reflected to the opposite direction of the incidence angle (this is caused by the reflection law: incidence angle equals emergence angle). If no energy returns to the antenna, the area will be represented by a dark signature. At a surface with intermediate roughness part of the signal is reflected and the other part is scattered diffusely. At a rough surface the radar signal is diffusely scattered at all angles, which causes a strong backscatter signal and thus results in a bright signature. With the help of the Rayleigh criterion a relief can be considered to be smooth if it fulfills Equation (5).

$$h < \frac{\lambda}{8 \sin \theta} \qquad (5)$$

where: h represents the vertical relief.

As the roughness is dependent on the radar wavelength a surface can behave different for different radar systems. If we assume the same depression angle (40°) for radar systems in two different wavebands and the same vertical relief (1.4 cm), a surface could be considered as rough in an X-Band image, whereas it would have an intermediate roughness in a C-Band image, or even a smooth surface in an L-band image (Sabins, 1997). Radar waves can also penetrate a surface depending on their wavelength and the surface`s moisture content. Figure 4.14 illustrates the penetration depth of different radar bands at different surfaces. It is obvious that longer wavelength results in a higher penetration depth. With the increase of the SMC, the corresponding penetration depth will be decreased. Ulaby (1996) illustrated in the plots shown in Figure 4.15 an example of the variation of the penetration depth with the volumetric moisture content (m_v) at three microwave frequencies for a homogeneous loamy soil. For L-band (1.3 GHz), the depth decreases from 1 m at m_v = 1% down to 6 cm at 40%.

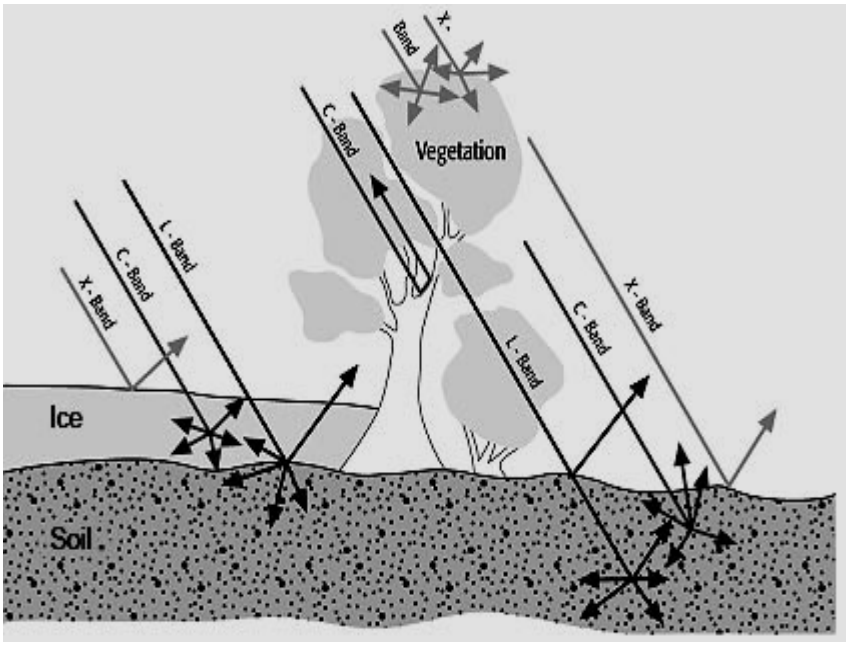

Figure 4.14: Penetration Depth of Different Radar Wavelengths (Martin, 2002).

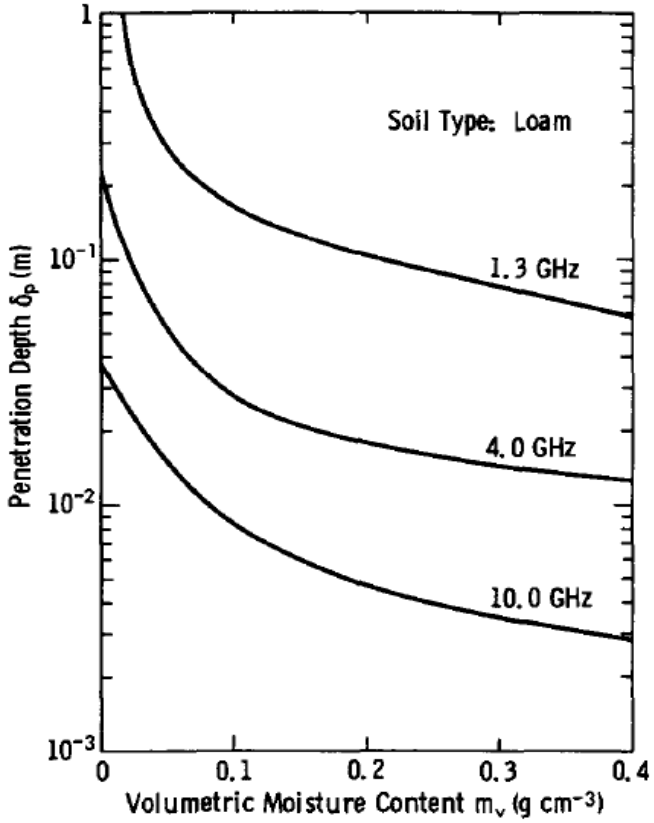

Figure 4.15: Penetration Depth as a Function of Moisture Content for Loamy Soil at Three Microwave Frequencies (Ulaby, 1996).

The SAR technique can be used to derive the soil moisture content corresponding to the degree of saturation in the near surface layer. Given that the presence of dense and high vegetation cover prevents X- and C-band radar signals (wavelengths between 3 and 6 cm) from reaching the ground (Fung, 1994), soil moisture mapping is often carried out exclusively on bare soils or zones with little vegetation cover (Baghdadi et al., 2008; Zribi et al., 2008). The arrival of the ALOS PALSAR (L-band) has been enabling soil moisture mapping based on SAR data to be extended from bare soils to soils with vegetation (depending on the density and height of the vegetation). The increasing number of SAR satellites and the short revisiting interval of new sensors (TerraSAR-X and Cosmo-SkyMed) now make it possible to map soil moistures with high temporal frequencies (daily to weekly; Baghdadi et al., 2008).

In the presented study the research for the retrieval of soil moisture focuses on the potentials of X and L bands, which are operational on TSX, and ALOS satellites. The radar signal at X-band is still sensitive to SMC but it is significantly influenced by vegetation and surface roughness, so that the estimation of spatial variations of moisture with the accuracy requested in many applications is still rather problematic and needs the use of correcting procedures.

4.3.2 Soil Moisture Estimation from SAR Data

As mentioned in section 3.2.4. Two TSX microwave remote sensing StripMap images were acquired on 31 May 2010 and 17 Jun 2010, by DLR. Another ALOS PALSAR image was acquired by ESA on 31 May 2010. From these images, the backscattering coefficients were determined and from simultaneous field works, the corresponding volumetric soil moisture was measured.

The backscatter coefficient (σ°) obtained by SAR sensors is related to the local topographic conditions, surface roughness and dielectric constant of the soil. The significantly high difference in the dielectric constant between water and dry soil and its variation is an indicator of soil moisture concentration. The coefficient σ° is composed of backscatter from vegetation (σ_v), and from soil (σ_s), and the attenuation caused by the vegetation canopy L_c.

This relationship can be expressed in Equations (6) & (7) based on Engman & Gurney (1990).

$$\sigma^\circ = \sigma_v + \sigma_s / L_c \qquad (6)$$

Parameter σ_s has a direct association with the m_v as:

$$\sigma_s = R_s S \; m_v \qquad (7)$$

where: R_s is the surface roughness, and
S is the soil-moisture sensitivity.

Although these terms may vary with the wavelength, polarisation and incidence angle of the radar beam, there is no satisfactory theoretical model suitable to estimate these terms independently. Therefore, an empirical relationship between the measured backscatter and soil moisture, which is approximately linear, is generally established.

4.3.2.1 TSX Radiometric Calibration

TSX Radar Brightness Calculations

The radar brightness β° is derived from the image pixel values or digital numbers (DN) applying the calibration factor K_S (Equation 8):

$$\beta^\circ = K_S \,.\, |\, DN \,| \qquad (8)$$

where K_S is the calibration coefficient for the TSX images (scaling gain value) and varies from 10E-6 to 10 E-4 depending on radar incidence angle (θ_i) and polarisation. It is also called calFactor and is given in the TSX data delivery package annotation file “calibration”. An extract of these data is shown in Figure 4.16.

```
    <polLayer>HH</polLayer>
    <beamID>strip_007</beamID>
    <DRAoffset>SRA</DRAoffset>
    <calFactor>1.19752740163255090E-05</calFactor>
  </calibrationConstant>
</calibration>
<noise layerIndex="1">
    <polLayer>HH</polLayer>
    <beamID>strip_007</beamID>
    <DRAoffset>SRA</DRAoffset>
    <noiseModelID>LINEAR</noiseModelID>
    <noiseLevelRef>BETA NOUGHT</noiseLevelRef>
    <numberOfNoiseRecords>3</numberOfNoiseRecords>
    <averageNoiseRecordAzimuthSpacing>1.99994897842407227E+00</averageNoiseRecord
```

Figure 4.16: Extract of the Annotation File of the TSX- StripMap Image Obtained on 17.06.2010.

The radar brightness is converted into dB using Equation (9):

$$\beta^{\circ}_{dB} = 10 \log_{10} (\beta^{\circ}) \quad (9)$$

Calculation of Sigma Naught

Backscattering from a target is influenced by the relative orientation of the illuminated resolution cell and the sensor, as well as by the distance in range between them. The derivation of Sigma Naught thus requires a detailed knowledge of the local slope (i.e. local incidence angle), as shown in Equation (10):

$$\sigma^{\circ} = (K_S \,.\, |DN|^2 - NEBN) \,.\, \sin\theta_{loc} \quad (10)$$

Where: K_S is the calibration and processor scaling factor given by the parameter calFactor, DN is the pixel intensity values, θloc is the local incidence angle. It is derived from the Geocoded Incidence Angle Mask (GIM), and NEBN is the Noise Equivalent Beta Naught which represents the influence of different noise contributions to the signal (Fritz & Eineder, 2008).

Equation (10) can be expressed in terms of Beta Naught, as shown in Equation (11):

$$\sigma^{\circ} = \beta^{\circ} \,.\, \sin\theta_{loc} - NESZ \quad (11)$$

NESZ is the Noise Equivalent Sigma Zero. Fritz & Eineder (2008) expressed the system noise in terms of Sigma Naught (Equation 12):

$$NESZ = NEBN. \sin\theta_{loc} \quad (12)$$

NESZ is specified to be between -19dB and -26dB. For this reason the noise influence can often be neglected, depending on the considered application.

In case NEBN is ignored, Equation (11) reduces to the Equations (13) & (14):

$$\sigma^{\circ} = \beta^{\circ} \,.\, \sin\theta_{loc} \quad (13)$$

$$\sigma^{\circ}_{dB} = \beta^{\circ}_{dB} + 10 \log_{10}(\sin\theta_{loc}) \quad (14)$$

Geocoded Incidence Angle Mask

The local incidence angle is the angle between the radar beam and the normal to the illuminated surface. The GIM provides information about the local incidence angle for each pixel of the geocoded SAR scene and about the presence of layover and shadow areas. The GIM product shows the same cartographic properties as the geocoded output image with regard to output projection and cartographic framing. The content of GIM is basically the local terrain incidence angle and additional flags indicating whether a pixel is affected by shadow and/or layover or not.

Extraction of the Layover and Shadow Identifiers

The shadow areas are determined via the off-nadir angle, which in general increases for a scan line from near to far range. Shadow occurs as soon as the off-nadir angle reaches a turning point and decreases when tracking a scan-line from near to far range. The shadow area ends where the off-nadir angle reaches that value again, which it had at the turning point.

Applying Equation (15) yields to the extraction of the Layover and Shadow (LS) information:

$$LS = GIM \bmod 10 \quad (15)$$

Extraction of the Local Incidence Angle

Equation (16) shows the relation between the local incidence angle in degrees and GIM.

$$\theta_{loc} = \frac{(GIM - LS)}{100} \quad (16)$$

By substitution using Equations (9), (15) and in Equation (14) the final equation of the backscattering determination is presented in Equation (17):

$$\sigma^{\circ}\,(dB) = 10 \log_{10}(K_S) + 10 * [\, 2 \log_{10}(DN) + \log_{10} \sin(\, GIM - GIM\ mod 10)/\, 100\,] \quad (17)$$

4.3.2.2 ALOS PALSAR Radiometric Calibration

The obtained ALOS PALSAR image on 31.05.2010 was geometrically terrain corrected as a necessary step to allow geometric overlays of the data and to remove effects of side looking geometry of SAR images. A comparison between Digital Ortho-Photos (DOP) with 20 cm spatial resolution obtained from GeoSN, and the ALOS PALSAR image is illustrated in Figure 4.17. The obtained TSX data were already corrected by the DLR.

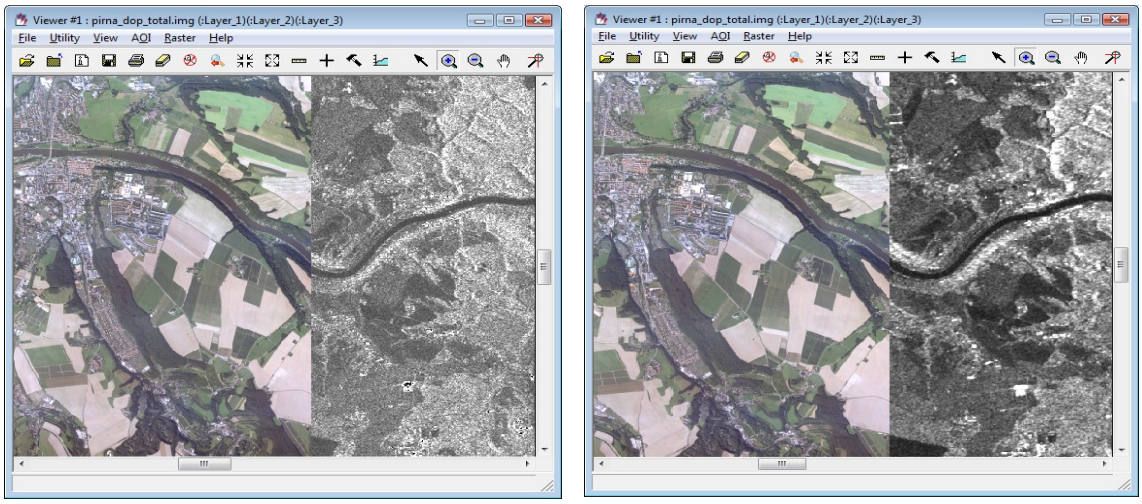

(a) (b)

Figure 4.17: Comparison between Corrected DOP and ALOS PALSAR Image. a) ALOS PALSAR Image before Geocoding and Terrain Correction, b) ALOS PALSAR Image after Corrections.

To perform a precise absolute calibration and derive σ°, a detailed knowledge of the local slope (i.e. θ_{loc}) is required. Since the information is frequently not available; a "flat terrain" is assumed during processing (based on the ellipsoid of WGS-84). The incidence angle correction (area normalisation) has been included in the processing, and therefore the final image intensity (i.e. the square of the digital number DN) is proportional to the normalised radar cross-section σ° of the illuminated scene.

The relationship between DN and σ° can be written as:

$$DN^2 = \sigma^\circ \cdot const \qquad (18)$$

The const factor is constant and it is hereafter referred as "absolute calibration constant" (K), which is derived from measurements over precision transponders.

The calibration constant is derived from the calibration factor (CF). For data processed with version 5.04 of the ALOS Data European Node (ADEN) Processor (installed on 11.03.09), a CF = –83 dB with accuracy of 0.64 dB was obtained.

Derivation of Sigma, Beta and Gamma Naught over Distributed Target

Calibrated angles σ°, β°, γ° can be calculated as:

$$\sigma^\circ_{i,j} = K.DN^2_{i,j} \qquad (19)$$

$$\beta^\circ_{i,j} = \frac{\sigma^\circ_{i,j}}{\sin(\propto_{i,j})} \qquad (20)$$

$$\gamma^\circ_{i,j} = \frac{\sigma^\circ_{i,j}}{\cos(\propto_{i,j})} \qquad (21)$$

i = 1,2,3,……...L & j = 1,2,3,……M

Where:

$DN_{i,j}^2$ = Pixel intensity value at image line *i* and column *j*
$\sigma^\circ_{i,j}$ = Sigma nought (backscattering coefficient) at image line *i* and column *j*
$\beta^\circ_{i,j}$ = Beta nought (brightness) at image line i and column j
$\gamma^\circ_{i,j}$ = Gamma nought at image line *i* and column *j*
$\propto^\circ_{i,j}$ = Incident angle at image line *i* and column *j*
L, M = Number of lines and columns in the image
K = Absolute calibration constant

The average backscattering coefficient for an area of interest can be derived as an average of $\sigma^\circ_{i,j}$ over N= N_a × N_r pixels within the distributed target as:

$$\sigma^\circ_{avg} = \frac{1}{N}\sum_{i=1}^{i=N_r}\sum_{j=1}^{j=N_a}\sigma^\circ_{i,j} \qquad (22)$$

To obtain sigma naught to dB the following equation is used:

$$\sigma^\circ\,(dB) = 20\log_{10}\sigma^\circ = 20\log_{10}(DN) + K\,(dB) \qquad (23)$$

Speckle Reduction and Preprocessing of SAR Data

The use of coherent radiation during the generation of SAR data causes a noise-like phenomenon known as speckle effect which reduces a meaningful interpretation. Several adaptive filters have been developed to reduce the speckle effect and to obtain the spatial structure and texture of the image content at the same time (Seiler et al., 2009). Quantitative measurements like the Equivalent Number of Looks (ENL; Equation 24), calculated for homogeneous test regions of the SAR images can be used for an evaluation of the speckle filter. High ENL values accomplish a high degree of speckle reduction (Wang et al., 2004), qualitative evaluation of the speckle filtered image by the user is also essential.

In order to determine which of the filters is most effective, six different ones were tested regarding their suitability for speckle reduction. Two techniques were applied to choose the suitable way of filtering either before or after the determination of σ°. Equation (17) was applied for TSX data in order to

calculate the backscattering coefficient; this equation transforms the DN into σ° in decibels.

$$ENL = Mean^2 / Variance \quad (24)$$

The ENL values show that the best result of the obtained TSX image on 31May 2010 were achieved by using the Median filter with a kernel size of 7*7 after the determination of σ° as demonstrated in Table 4.4.

Table 4.4: Comparison between Different Filters Using ENL for TSX Data.

Filter Name	Kernel Size	σ° before Filter	σ° after Filter
		ENL	
Lee-Sigma	3	17.43	12.92
	5	17.44	14.30
	7	17.45	15.16
Median	3	18.07	12.87
	5	23.03	14.79
	7	26.64	15.93
Frost	3	17.46	11.49
	5	20.07	12.13
	7	22.31	12.77
Local Region	3	15.60	11.75
	5	18.48	13.18
	7	21.78	14.49
Mean	3	15.12	13.09
	5	16.41	14.83
	7	18.82	15.81
Gamma Map	3	14.31	12.35
	5	17.49	13.86
	7	21.37	16.25

When applying the same procedure on the ALOS PALSAR image, the best result was achieved by using Mean filter with a kernel size of 5*5 after the determination of σ°. Although the ENL of this filter is less than the ENL of the Median Filter with a kernel size of 7*7, the user visual inspection of the speckle filtered image for Mean filter was better as shown in Figure 4.18.

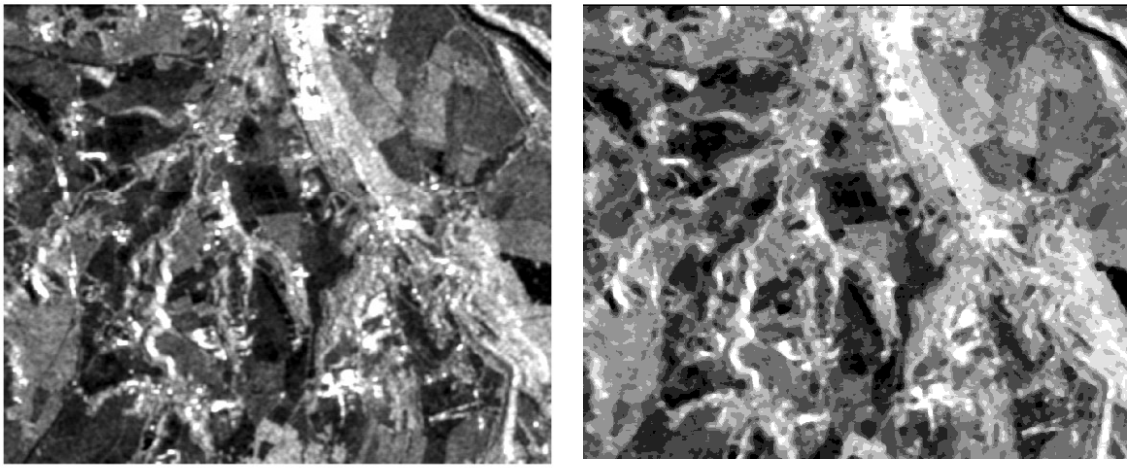

''Mean'' Filter with kernel size 5*5 ''Median'' Filter with kernel size 7*7

Figure 4.18: Comparison between Qualitative Evaluation of Speckle for Two Filtered Parts of ALOS PALSAR Image.

4.3.2.3 Field Measurements of the Soil Moisture

Within a volume of soil the two physical parameters that describe the surface area are the specific surface area and the bulk density of the soil (Jackson, 1989), therefore the volumetric soil moisture was measured. It is equal to the multiplication of the gravimetric soil moisture by the dry soil bulk density.

During the SAR data acquisition, field measurements of the volumetric soil moisture were carried out simultaneously using the TDR - HH2 Moisture Meter. The field measurements were made on both bare and ploughed fields. Also for vegetation fields (grasslands and corn fields) measurements were performed. Eight to twelve measurements were taken at each tested field location at 0 – 5 cm soil depths and subsequently averaged. Figure 4.19 illustrates the measured soil sample distribution and the applied TDR device. Photographs of some tested fields and the used equipments are given in Appendix 2.

The measured TDR volumetric soil-moisture values were obtained on 31.05.2010 and ranged between 14.1 % and 47.3 % with standard deviations of 1.02 to 3.24. For the data collected on 17.06.2010, the range of the TDR-measured soil-moisture values was between 11.2 % and 25.3 % with a standard deviation from 1.1 to 2.11.

In order to validate the TDR measurements, on 31.05.2010 10 soil samples were collected from the field. Subsequently, the volumetric soil moisture was determined at the laboratory of the Institute of Geography at the Dresden University of Technology. Table 8 in Appendix 1 illustrates the calculated m_v and

corresponding TDR measured values. The results show that the Route Mean Square Error (RMSE) is 0.98 % which indicates highly precise TDR measurements.

The soil moisture content may be expressed by weight as the ratio of the mass of water present to the dry weight of the soil sample, or by volume as a ratio of volume of water to the total volume of the soil sample. To determine any of these ratios for a particular soil sample, the water mass must be determined by completely drying the soil and measuring the soil sample mass after and before drying. The water mass (or weight) is the difference between the weights of the wet and oven dry samples. The criterion for a dry soil sample is the soil sample that has been dried to a constant weight in oven at temperatures between 100 – 110° C (105°C is typical).

The volumetric soil moisture was then obtained by multiplying the gravimetric soil moisture by the dry soil bulk density.

Gravimetric soil moisture (SM) can be calculated from:

$$\mathrm{SM} = \frac{W2 - W3}{W3 - W1} \qquad (25)$$

where: W1 = Weight of container,
W2 = Weight of moist soil + container, and
W3 = Weight of dried soil + container.

Bulk density can be calculated from:

$$\gamma_b = \frac{W3 - W1}{(3.14 * r^2 * h)} \qquad (26)$$

where: r = radius of the core, and
h = height of the core.

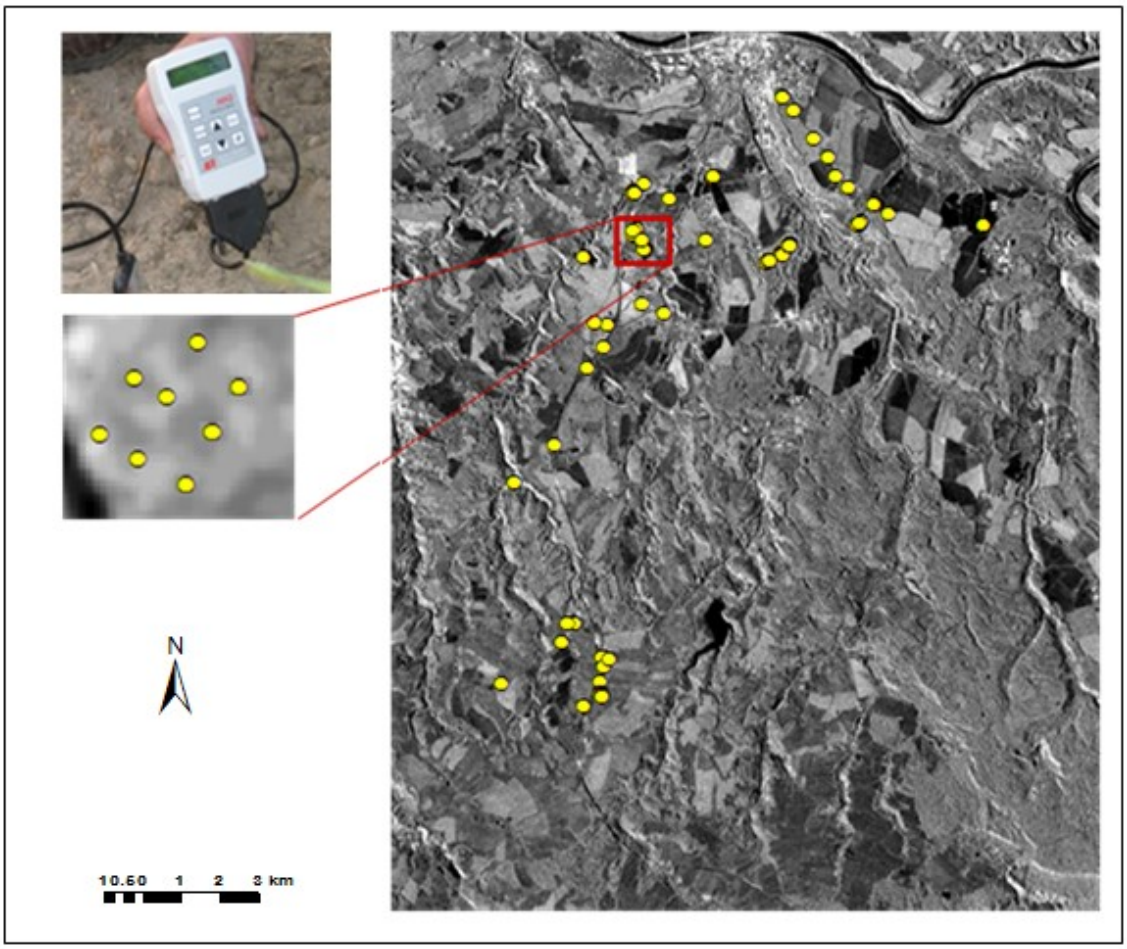

Figure 4.19: Distribution of the Measured Soil Samples.

By applying Equation (17) to the TSX images and Equation (23) to the ALOS PALSAR image using the Model Maker tool in ERDAS IMAGINE 9.2 the backscattering coefficients could be retrieved for each tested field.

The direct correlation between the in-situ measured soil moisture and the backscattering coefficient are listed in Tables 1 to 6 in Appendix 1. The relations between them were plotted using vertical box plots (Figures 4.20 to 4.22) which indicate vertically the different values of the field measurements at each field, and the horizontal axis indicates the average backscattering values of 3*3 pixel convolutions which were accomplished using the spatial enhancement tool of ERDAS IMAGINE 9.2. The regression equations and the coefficient of determination (R^2) of each plot are listed in Table 4.5.

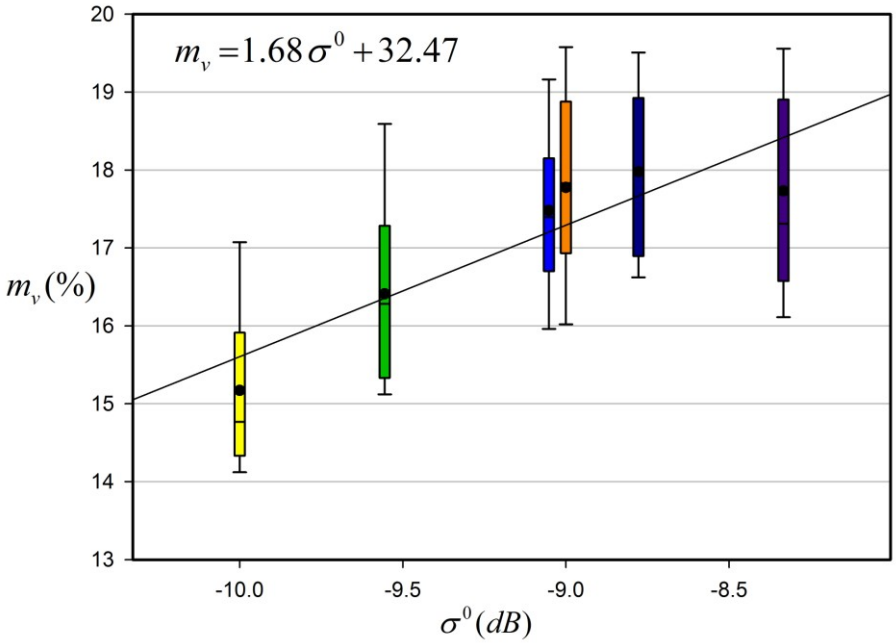

Bare Fields

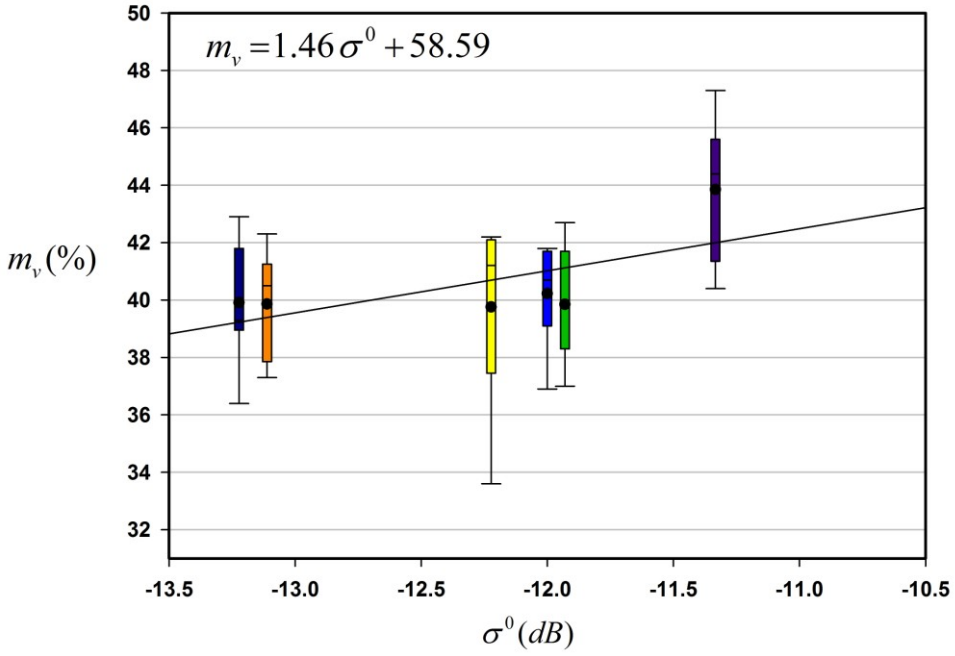

Vegetated Fields

Figure 4.20: Soil Moisture as a Function of σ˚ (TSX: HH polarisation, incidence angle 43˚) on 31.05.2010.

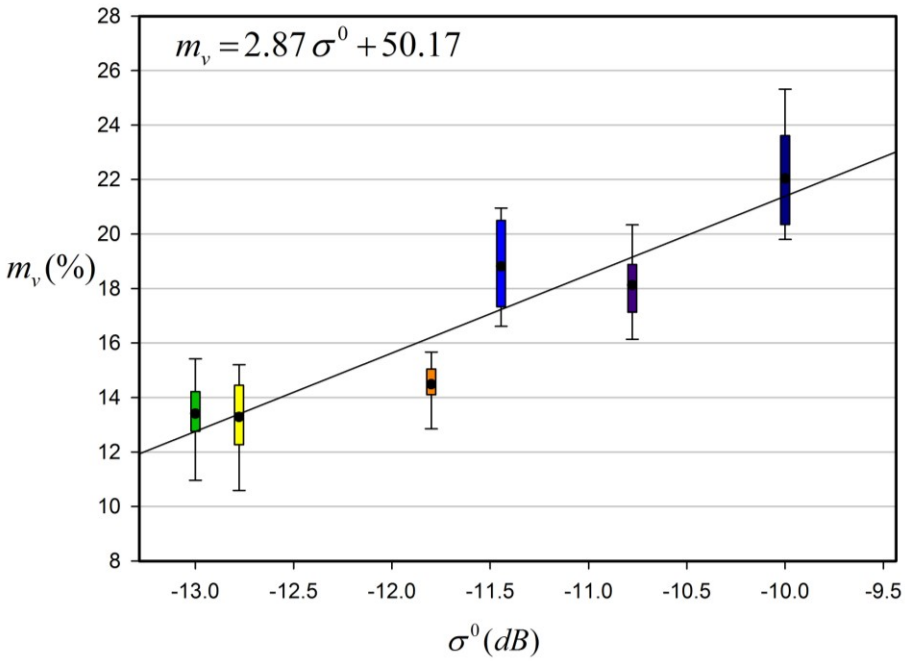

Bare Fields

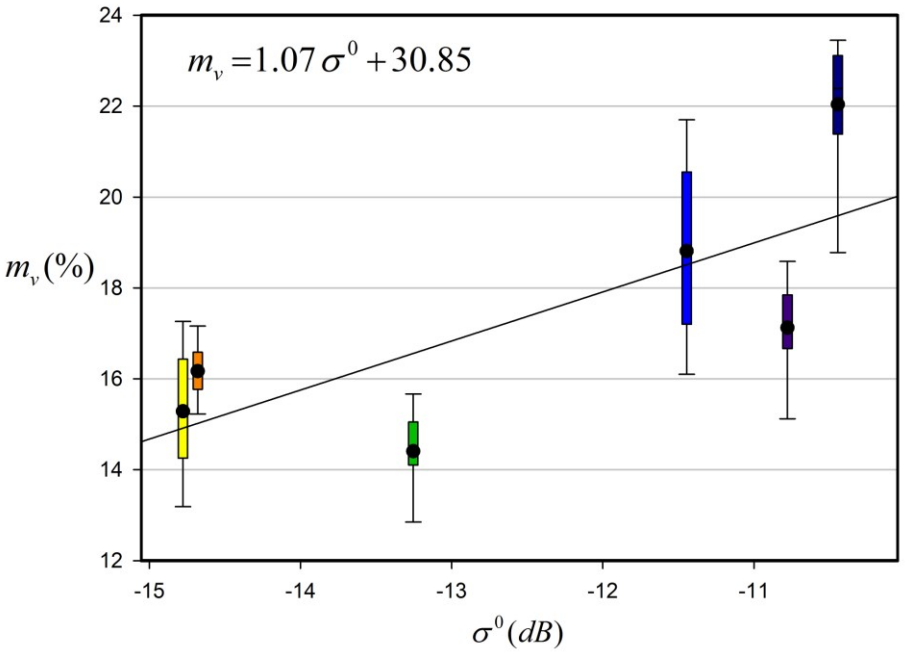

Vegetated Fields

Figure 4.21: Soil Moisture as a Function of σ˚ (TSX: HH Polarization-incidence angle 31˚) on 17.06.2010.

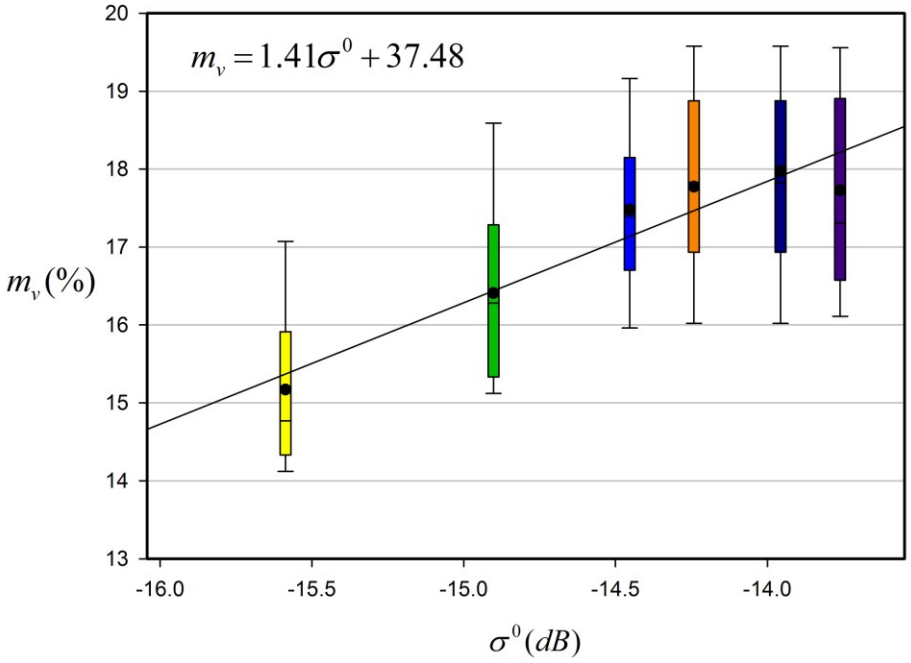

Bare Fields

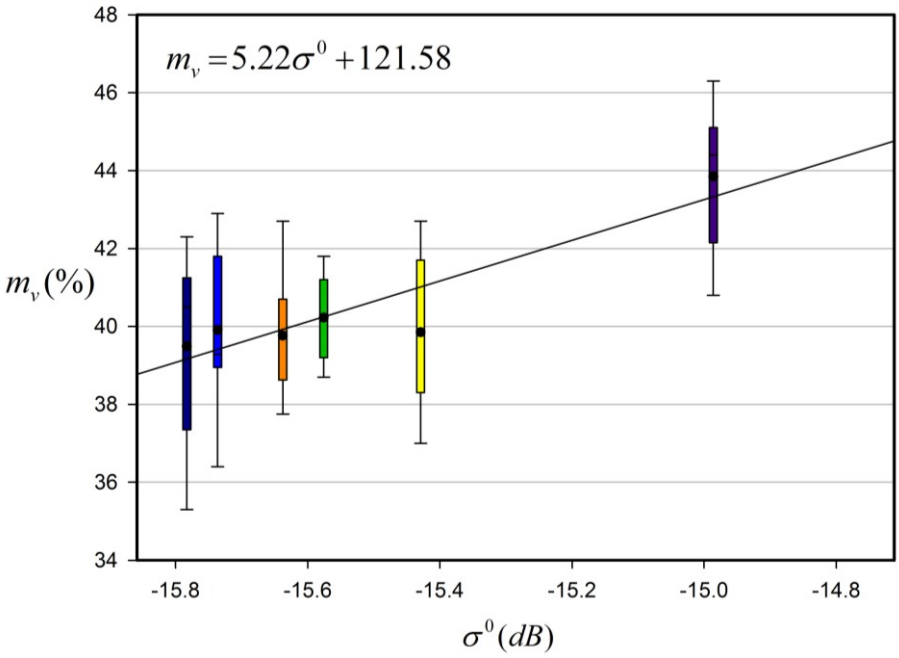

Vegetated Fields

Figure 4.22: Soil Moisture as a Function of σ˚ (ALOS PALSAR: HH polarisation, incidence angle 34˚) on 31.05.2010.

Table 4.5: Direct Correlation between the In-situ Measured Soil Moisture and Backscattering Coefficient.

Sensor	Date	Regression equations of baring fields	R^2	Regression equations of Grassland/crops	R^2
TSX	31.05.2010	$m_v = 1.68\ \sigma° + 32.47$	0.82	$m_v = 1.46\ \sigma° + 58.59$	0.44
	17.06.2010	$m_v = 2.87\ \sigma° + 50.17$	0.88	$m_v = 1.07\ \sigma° + 30.85$	0.56
ALOS PALSAR	31.05.2010	$m_v = 1.41\ \sigma° + 37.48$	0.91	$m_v = 5.22\ \sigma° + 121.58$	0.85

For further explanation of the content of this table see chapter 5.

4.3.2.4 Soil Moisture Map Retrieval

After preprocessing of the SAR data a pixel-wise soil-moisture mapping was performed for both bare and vegetated soils. Based on the field survey and the obtained land cover maps (source: Agrargenossenschaft Osterzgebirge Börnersdorf e.G), the various land cover types were detected and subsequently soil-moisture maps were produced. The obtained soil maps were merged into one single map in ArcGIS as shown in Figures 4.23 to 4.25. The white zones represent the buildings, reservoirs, lakes, swamps, and most of all forests. These zones were excluded during the soil moisture extraction process. Since these missing parts are required as a data entry of the soil moisture for each sub-basin in the hydrological modelling, their soil moisture values were calculated from the nearest-neighbour pixels in each corresponding sub-basin and subsequently averaged. An example is shown in Figure 4.26.

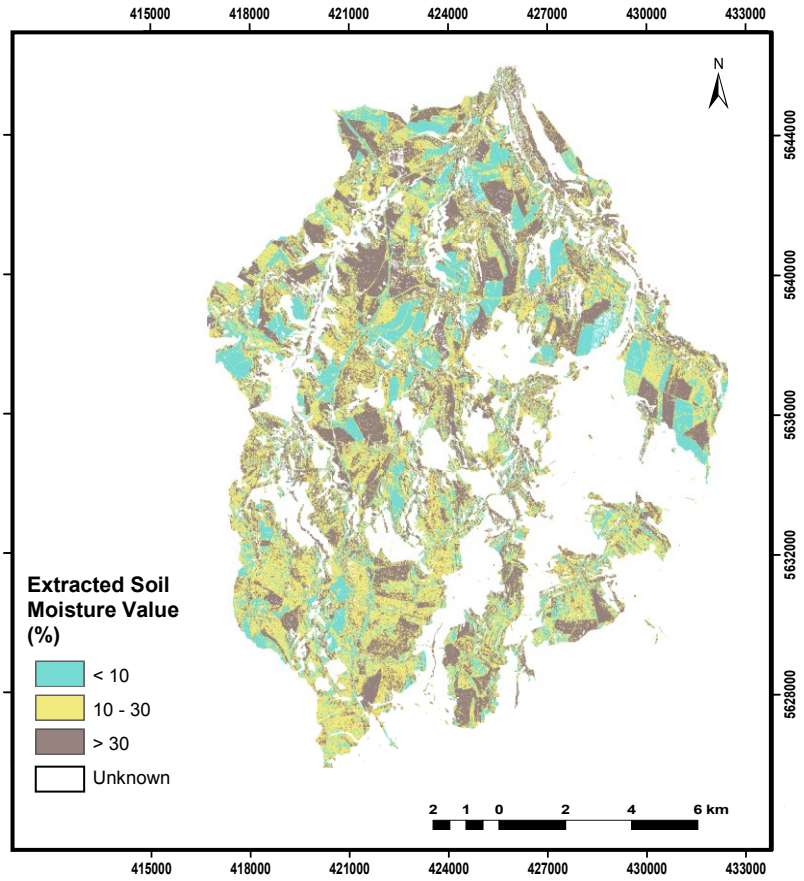

Figure 4.23: Soil Moisture Extracted from TSX Image Acquired on 31.05.2010.

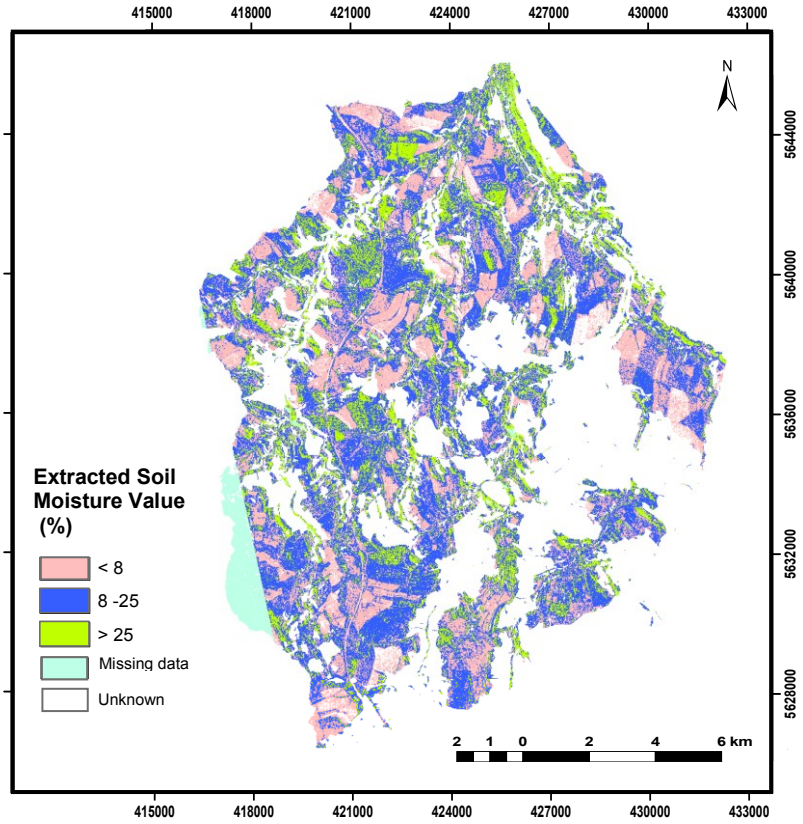

Figure 4.24: Soil Moisture Extracted from TSX Image Acquired on 17.06.2010.

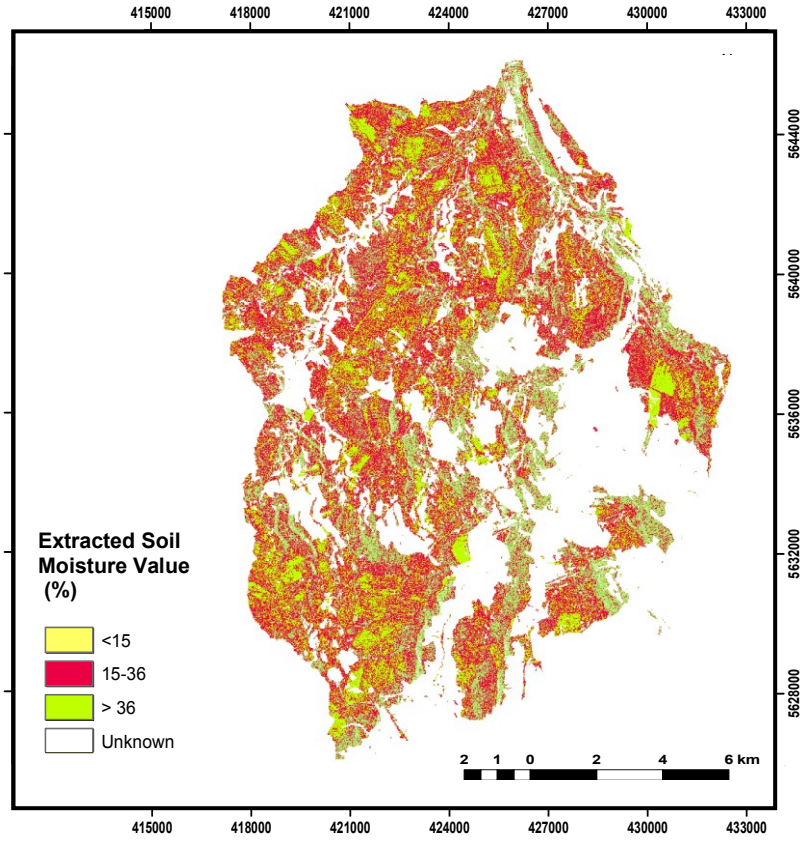

Figure 4.25: Soil Moisture Extracted from ALOS PALSAR Image Acquired on 31.05.2010.

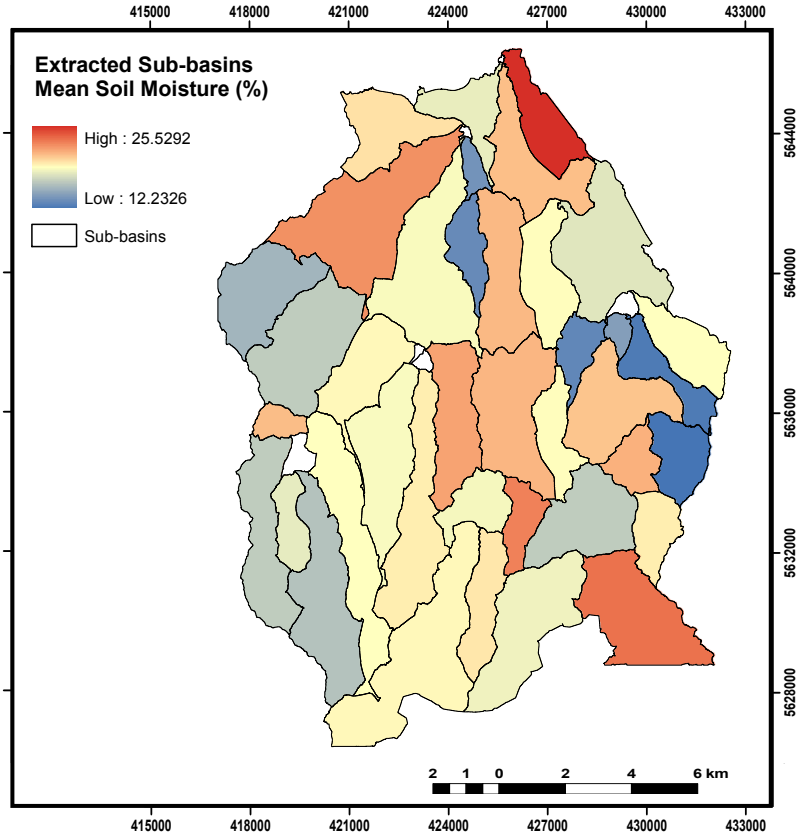

Figure 4.26: Mean Values of Soil Moisture Extracted from TSX Image Acquired on 31.05.2010 of Gottleuba Subbasins.

4.4 Hydrological Modelling

First, the extracted hydrological characteristics from the DTM of the Gottleuba catchment were integrated with the extracted spatial data from the SAR images in order to generate the hydrological parameters which are used to calculate the runoffs for different periods.

The HEC-HMS software was applied to generate the rainfall runoff model. It is designed to simulate the precipitation-runoff processes of dendritic watershed systems, and applicable in a wide range of geographic areas for solving the widest possible range of problems. This includes large river-basin water-supply and flood hydrology, and small urban or natural watershed runoff (HEC-HMS User's Manual).

The HEC-HMS model's main inputs are precipitation and watershed model. The output is streamflow discharge (Figure 4.27). The HEC-HMS is composed of several different modelling components that make up the entire watershed model including: (a) basin model which contains the elements of the basin, their connectivity, and runoff parameters, (b) meteorological model which contains the rainfall and evapotranspiration data, (c) loss method (infiltration model) that calculates runoff, (d) storage model, (e) the routing function that accumulates modelled flow from each of the distributed sub-basins, creating a streamflow hydrograph and (f) the control specifications which contain the start/stop timing and calculation intervals for the run. There are several different methods available for each modelling component.

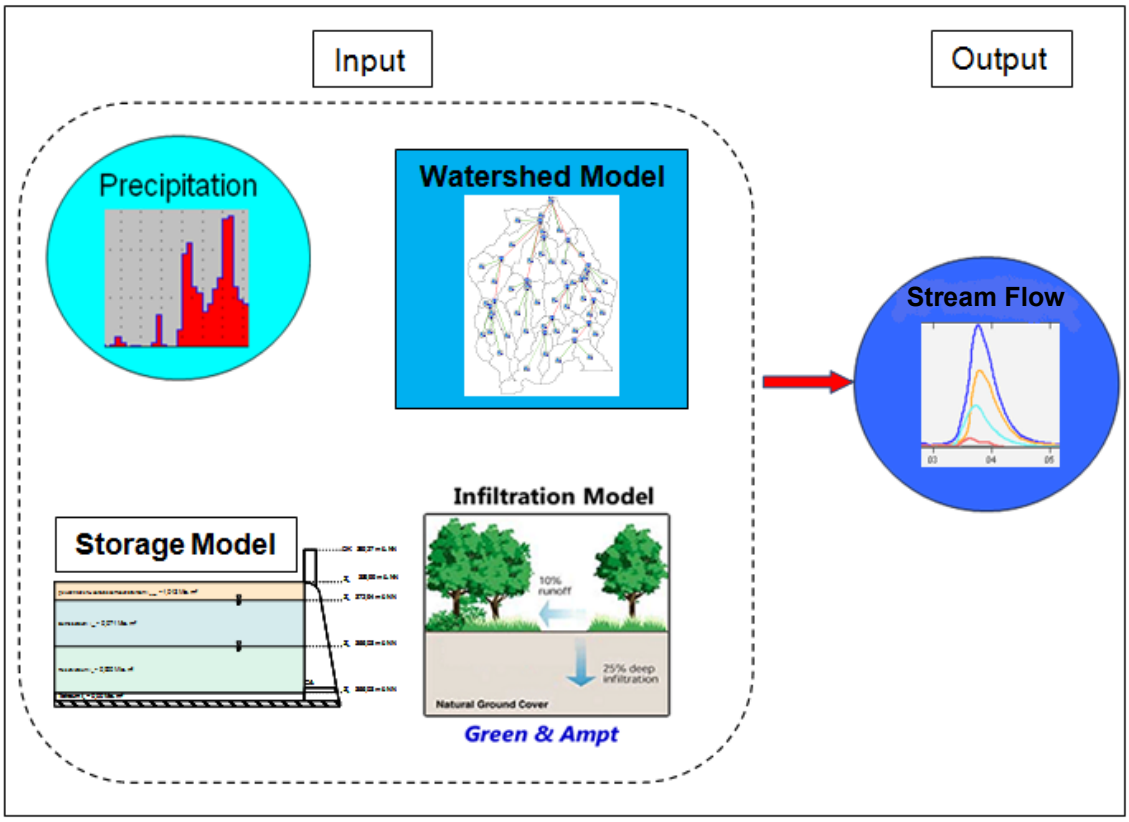

Figure 4.27: HEC-HMS Main Components.

The output from HEC-HMS was plotted as a hydrograph (flow vs. time plot) and the peak flow for model elements was also calculated for junctions, reaches and reservoirs. The next sections present the components of the HEC-HMS selected for this study.

4.4.1 Basin Model Setup

As illustrated in the previous sections 4.1 and 4.2, HEC-GeoHMS was used to prepare the input shape files for use in the HEC-HMS model. This preparatory function derived the necessary geometric features (slope, length, area, centroid location) from the topographic data base. The preprocessing of GIS data is necessary for the physical model, since the model calculates the hydrologic output on a grid level; subsequently a schematic network with the basin elements (nodes, links, junctions, etc.) and their connectivity were created. This scheme (illustrated in Figure 4.28-a) was imported into the HEC-HMS as input file for the basin model setup (Figure 4.28-b). The processing of these input files allows the delineation of the watershed boundaries and sub-basin boundaries. HEC-HMS quantifies lengths of the rivers, longest flow paths, slopes, centroid locations and lengths to the centroids.

4.4.2 Impervious Area

A component of the runoff volume computed by the HEC-HMS model is the percentage of the impervious area. The impervious polygon layer was created by intersecting the landuse map GIS database with the sub-basin polygons. The percentage of the impervious surface area was extracted for each sub-basin polygon.

4.4.3 Runoff Transformation

The SCS Unit Hydrograph method was used for the transform function. The unit hydrograph is an average streamflow response derived from empirical data of numerous past events, and is a function of drainage area, sub-basin lag-time, and runoff precipitation (McCuen, 1982). The lag time is defined as the time between hydrograph peak and event rainfall “center of mass” (NOHRSC, 2005). For the lag-time calculations Equation (4) was used.

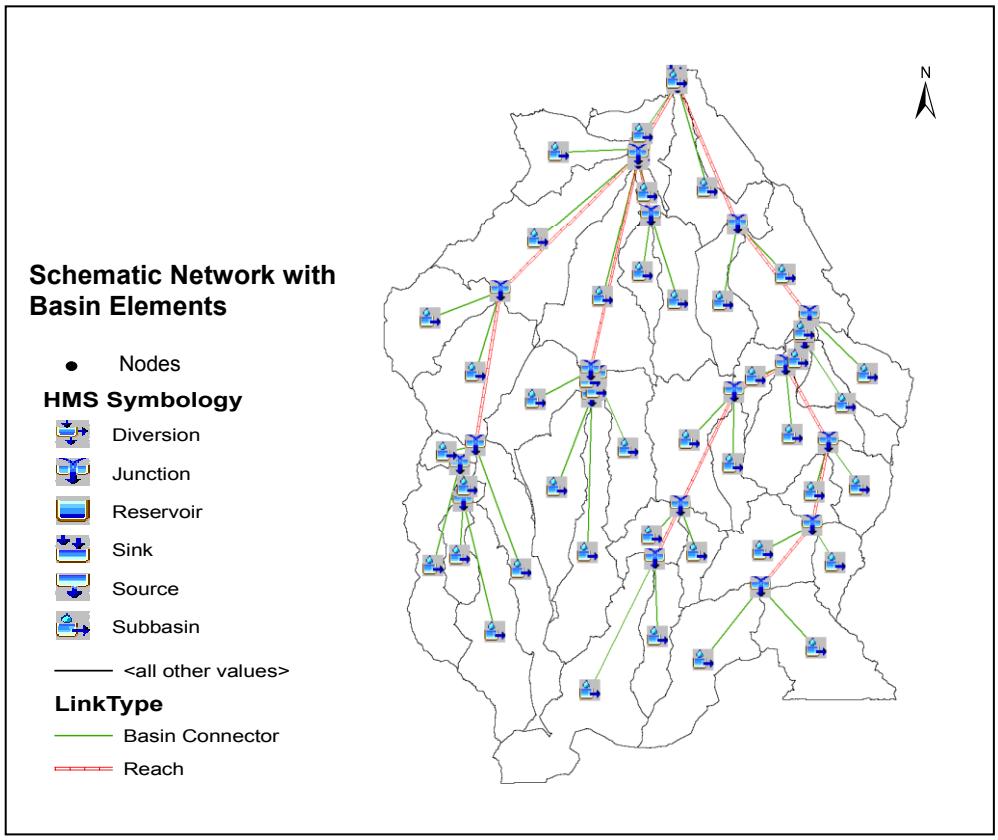

(a)

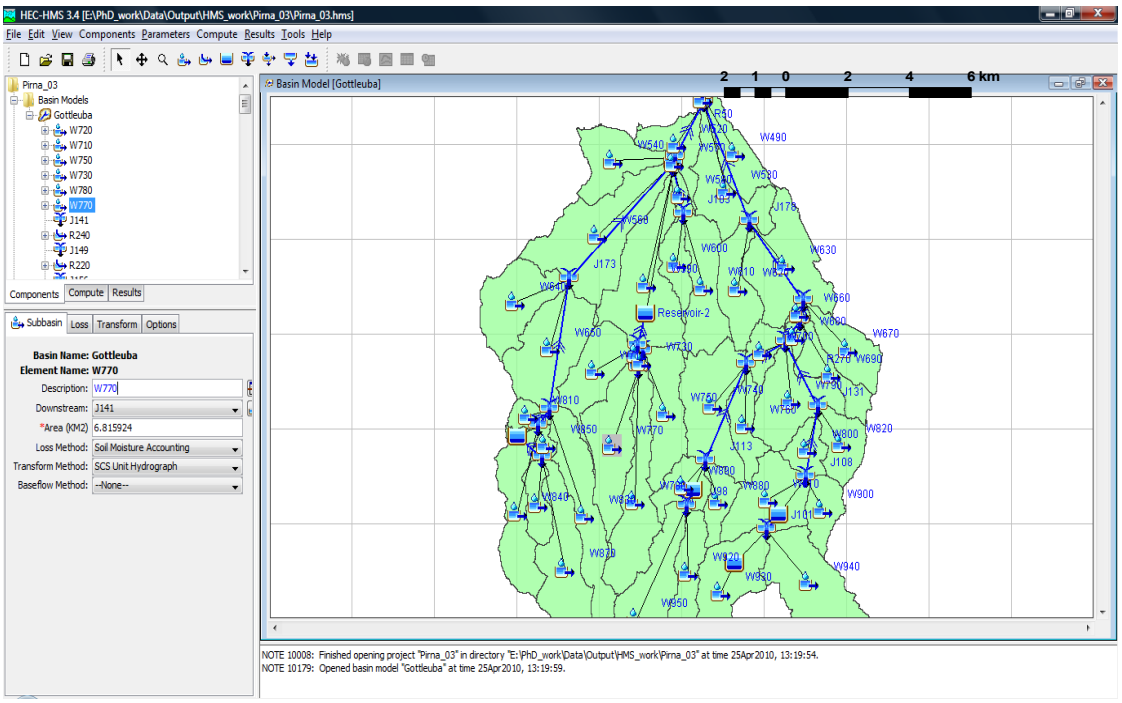

(b)

Figure 4.28: Schematic Network of Gottleuba Basin Elements; a) Obtained from HEC-GeoHMS, b) Imported into HEC-HMS.

4.4.4 Routing Method

The hydrologic routing from sub-basin outlets was performed using the widely applied Muskingum Method. The Muskingum Routing Method uses a simple conservation of mass approach to route flow through the stream reach. However, it does not assume that the water surface is level. By assuming a linear, but non-level, water surface it is possible to account for increased storage during the rising side of a flood wave and decreased storage during the falling side (USACE, 2010). By adding a travel time for the reach and a weighting between the influence of inflow and outflow it is possible to approximate attenuation. Ponce (1989) computed the outflow from a reach using the following formulas:

$$O_{t+\Delta t} = C_o\, I_{t+\Delta t} + C_1\, I_t + C_2\, O_t \qquad (27)$$

$$C_o = \frac{(\frac{\Delta t}{k}) - 2X}{2(1-X) + (\frac{\Delta t}{k})} \qquad (28)$$

$$C_1 = \frac{(\frac{\Delta t}{k}) + 2X}{2(1-X) + (\frac{\Delta t}{k})} \qquad (29)$$

$$C_2 = \frac{2(1-X) - (\frac{\Delta t}{k})}{2(1-X) + (\frac{\Delta t}{k})} \qquad (30)$$

where: O = outlet flow (m³/sec),
I = inflow (m³/sec),
S = storage volume (m³/sec),
X = dimensionless weighting factor (range from 0.0 to 0.5),
K = time constant or storage coefficient (hours), and
Δt = time interval.

Two parameters are required for the Muskingum routing routine. The Muskingum X parameter was set at the default value of 0.2 and the Muskingum K parameter was set at the default value of 1 hour. The X parameter works to simulate attenuation of streamflow volume, and the K parameter simulates a delay in streamflow as it moves through the channel.

The number of sub-reaches was entered. It affects attenuation where one sub-reach gives more attenuation, and increasing the number of sub-reaches decreases the attenuation.

4.4.5 Meteorological Model Setup

Within the CLISAX project the precipitation data sets were extracted and interpolated as daily gridded data of 500m x 500m. The CLISAX record has its origin in the monitoring networks of the DWD and the Czech. The obtained data were in ASCII format and converted into a raster format in ArcGIS. The precipitation records were determined for each of the sub-basins by intersecting the precipitation grid values with the sub-basins polygons. An example is shown in Figure 4.29. The extracted grid values were averaged for each sub-basin by using the statistical analyst tool of ArcGIS.

The rainfall data representing depth over time were provided as inputs to a meteorological component file in the model. This was used, with a control specification file, in order to provide the time steps for the model calculation of the rainfall runoff processes.

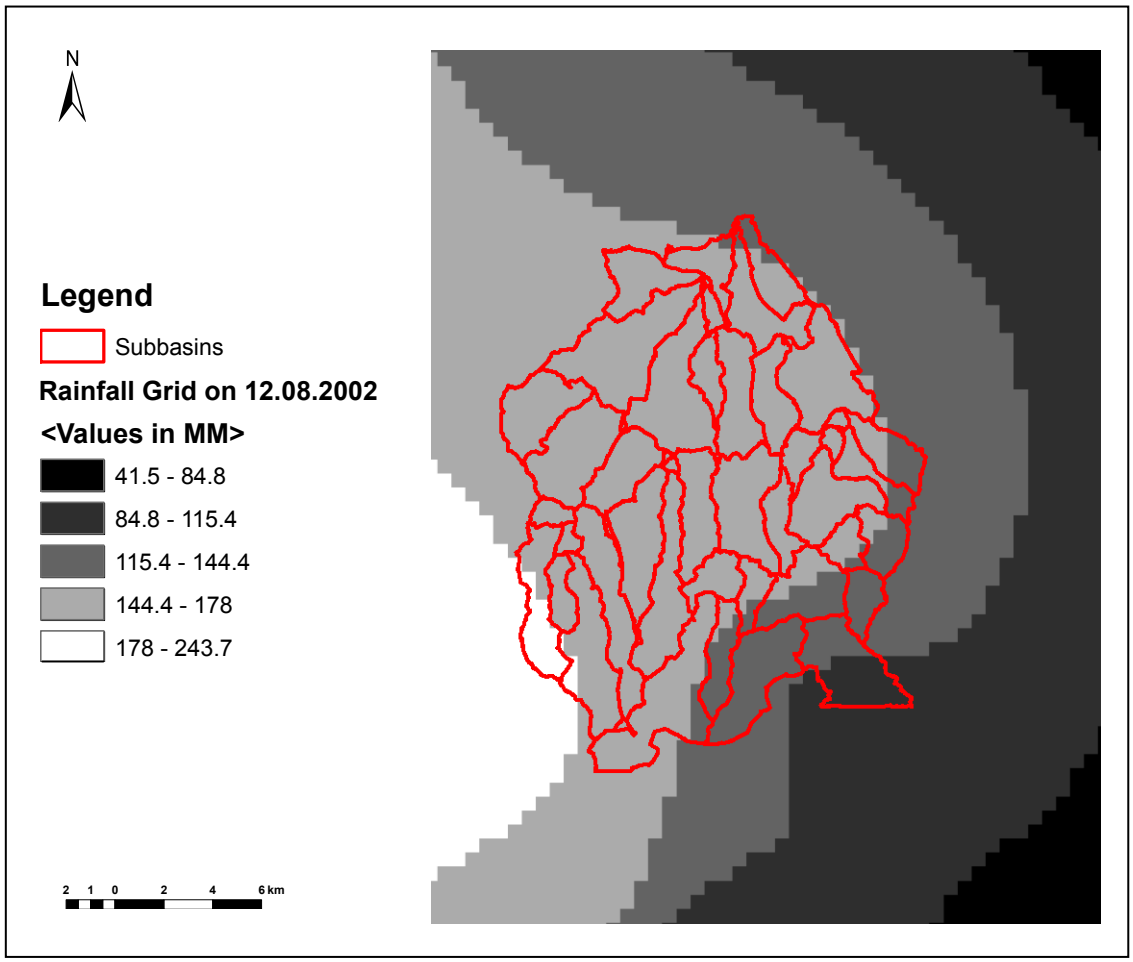

Figure 4.29: Gridded Precipitation Data on 12.08.2002.

4.4.6 Infiltration Model

HEC-HMS computes infiltration using the Green & Ampt Infiltration Model which includes computing the time to ponding. The time to ponding is the length of time required for the precipitation to saturate the soil so that surface runoff begins (USACE, 2010). The Green & Ampt Infiltration Model is a physical model which relates the rate of infiltration to measurable soil properties such as porosity, hydraulic conductivity, and moisture content of a particular soil.

Infiltration is the movement of water downward through the soil. The rate at which water can flow through the soil depends on the properties of the particular soil and its water content at the surface. This loss of water to the soil is known as abstraction. Other loss mechanisms include streambed losses, interception, and storage within topographical depressions.

There are several models to calculate abstraction due to infiltration including the SCS method and the initial loss plus constant loss rate model. However, these models have limitations. The SCS-CN relating abstractions to soil types and landuse have been arbitrarily determined, and the initial loss plus constant loss rate model is a non-physical model calibrated with gagged data. A more advantageous method (soil-moisture accounting loss) to determine abstractions is to relate loss rates to physical characteristics of the watershed in a continuous simulation so that loss rates may be computed as a function of soil moisture conditions at the beginning of a rain storm (Reed & Maidment 1998).

4.4.6.1 Soil-Moisture Accounting Loss

The Soil-Moisture Accounting Loss (SMA) Method in HEC-HMS uses three layers to represent the dynamics of water movement in the soil. The model simulates the movement of water through and storage of water on vegetation, on the soil surface, in the soil profile, and in groundwater layers Bennett (1998). It is often used in conjunction with a canopy and surface method. Layers within the method include soil storage, upper groundwater, and lower groundwater. The method provides for wetting and recovery cycles and can be used for long periods of continuous simulation (USACE, 2010). The parameters of the SMA Method were determined by calibration with the observed data of the year of the Saxony flash flood event 2002. In this iterative process, candidate parameter values were proposed.

4.4.7 Reservoir Routing

A reservoir is an element with one or more inflow and one computed outflow. Inflow comes from other elements in the basin model. If there is more than one inflow, all inflows are added together before computing the outflow. It is assumed that the water surface in the reservoir pool is level. Several methods are available for defining the storage properties of the reservoir. This component can be used to model reservoirs, lakes, and ponds.

The storage-outflow relationship can be specified by three available methods:
• Storage-discharge,
• Elevation-storage-discharge, and
• Elevation-area-discharge.

In this study, the elevation-storage-discharge function was applied. Here, the outflow is computed from the storage-discharge data, and then elevation is computed from the elevation-storage data. The required parameters for this method are: storage, elevations and discharge values. Interpolation is used when the elevation-storage-discharge or elevation-area-discharge methods are used (USACE, 2010). Therefore, the initial conditions assumed that the inflow is equal to the outflow value. Gottleuba Catchment contains five reservoirs, the parameters of the elevation-storage-outflow method for each reservoir provided by the LTV.

4.4.8 Model Calibration and Verification

The HEC-HMS model was run after preparing and supplying the required input parameters. The SCS loss method was applied to calibrate the model using the observed discharge values at the basin outlet obtained by Müller (2008) for the Gottleuba Catchment on the occasion of the Saxon flood event in August 2002. The observed hydrograph is shown in Figure 4.30. HEC-HMS simulated the runoff hydrograph for the same event. This was subsequently compared with the observed hydrograph in order to calibrate the model.

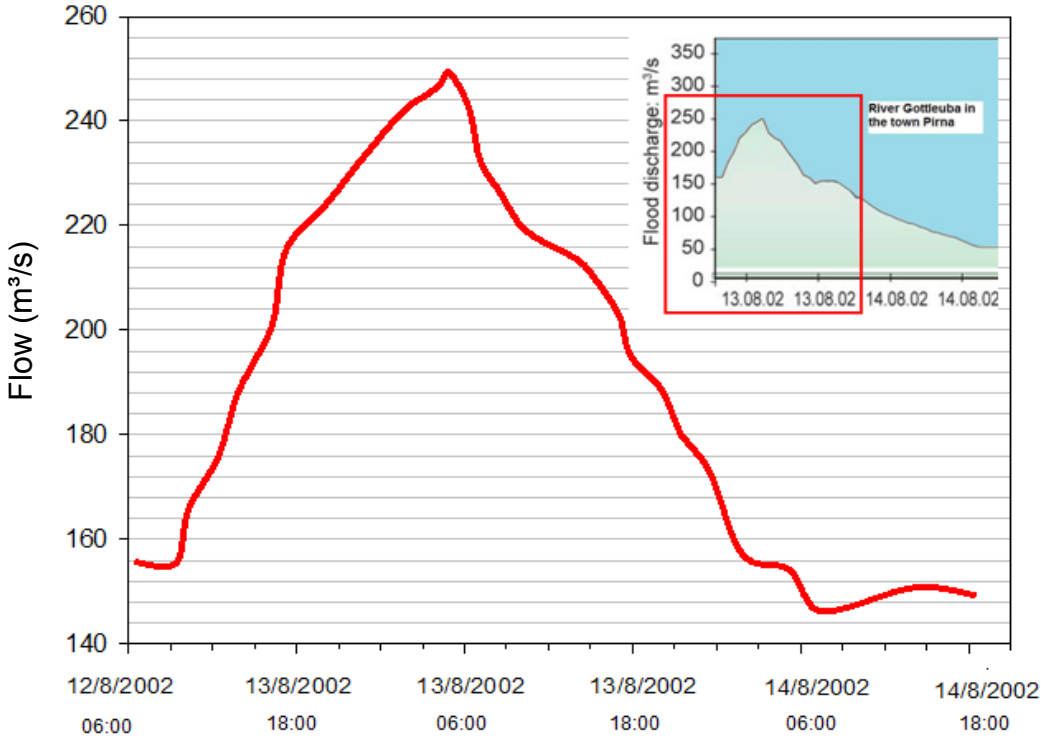

Figure 4.30: Hydrograph for 13.08.2002 Observed by Müller (2008), Redrawn by Elbialy (2011).

After fitting the simulated hydrograph to the measured one, the model was applied to generate the runoff values for the historical time period of the last ten years (from January 2000 to December 2009) using the SMA Loss Method. The soil-moisture values, required in the SMA method, were extracted using the BROOK90 software. BROOK90 is designed for evaporation and soil water. It simulates the water budget on a unit land area at a daily time step and is applicable to all land surfaces (hydrological model BROOK90, Federer, 1995). Inputs of daily precipitation, global radiation, relative humidity, wind speed, maximum and minimum air temperature were applied. An example of the plotted results for the year 2002 is shown in Figure 4.31.

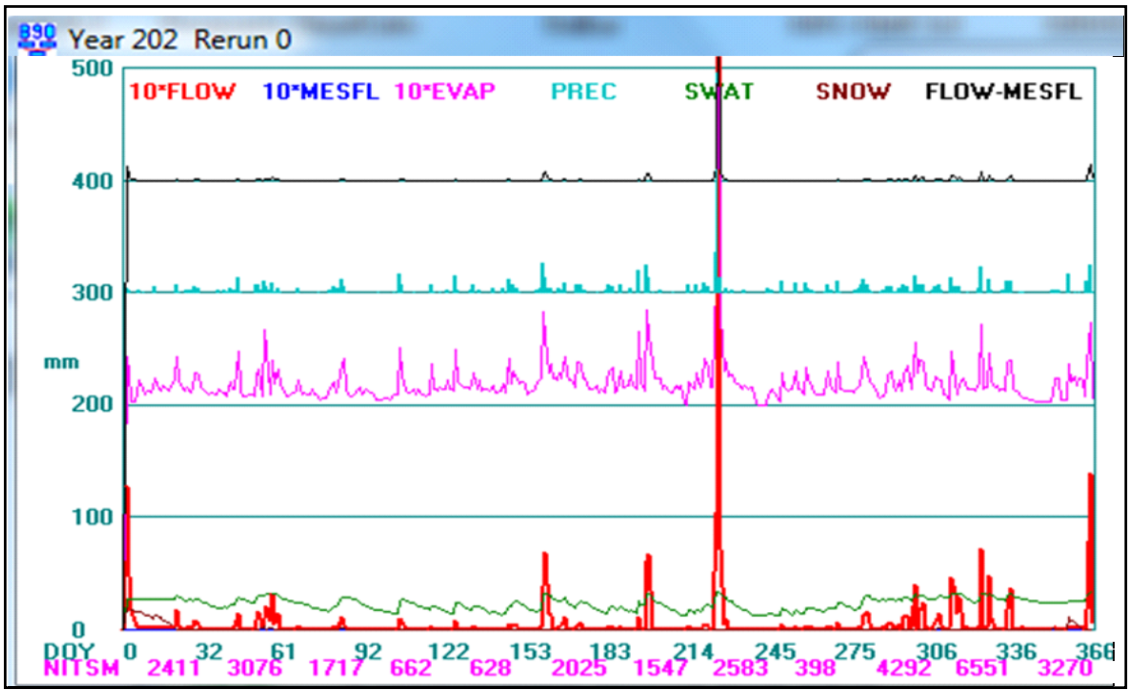

Figure 4.31: Plotted Results of BROOK 90. SWAT: Soil Water.

The obtained runoff results were used to validate the model in comparison to the observed discharge values at the Neundorf Hydrologic Station which is located in the East of the Gottleba Catchment. The simulated hydrograph was compared to the observed hydrograph as shown in Figure 4.32. The model performance was checked by two means of evaluation criteria namely, Root Mean Square Error (RMSE) and Theil's Coefficient (U) using the following formulas as given by Naylor (1970); Equations (31) & (32). The results are listed in Table 4.6.

$$\mathrm{RMSE} = \sqrt{\frac{1}{n}\sum_{i=1}^{n}(S_i - O_i)^2} \qquad (31)$$

$$U = \frac{\sqrt{\frac{1}{n}\sum_{i=1}^{n}(S_i - O_i)^2}}{\sqrt{\frac{1}{n}\sum_{i=1}^{n}(S_i)^2} + \sqrt{\frac{1}{n}\sum_{i=1}^{n}(O_i)^2}} \qquad (32)$$

Where: S_i = the simulated runoff records from the model,
O_i = the observed runoff records, and
n = the number of records.

The RMAE statistics have as the lower limit, the value of zero, which is the optimum value for them as it is for U. The smaller the RMSE value the better the model performance (Jacovides & Kontoyiannis, 1995).

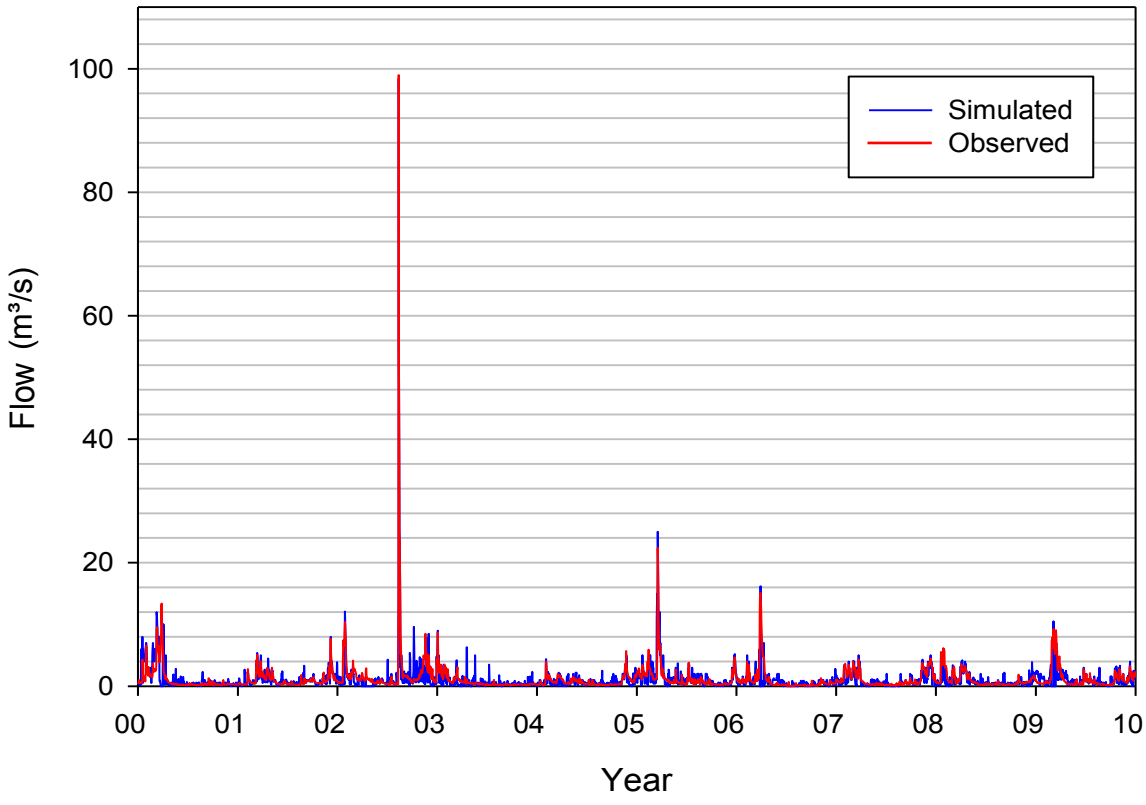

Figure 4.32: Simulated Flow versus Observed Flow from 01.01.2000 to 31.12.2009.

Table 4.6: Model Simulation Results from 01.01.2000 to 31.12.2009.

Station Neundorf	Peak flow (m^3/s)	Mean flow (m^3/s)	RMSE (m^3/s)	U
Simulated	98.4	1.05	1.62	0.38
Measured	99	1.17		

The runoff hydrograph was used as an indicator to evaluate the potential of the SAR data for soil-moisture retrieval. Therefore, the soil moisture extracted from the SAR data for each sub-basin was applied in the SMA Loss Method to determine the runoff hydrographs. In order to perform this evaluation, two rainfall periods were supplied to the model according to the obtained SAR data. The first was from 31.05.2010 to 31.08.2010. The obtained and the observed hydrographs are illustrated in Figures 4.33 & 4.34 and the results listed in Table 4.7. The second period was from 17.06.2010 to 31.08.2010. The obtained hydrographs were compared to the observed hydrographs of the Neundorf station. Hydrographs and accuracies are illustrated in Figure 4.35 and Table 4.8 respectively.

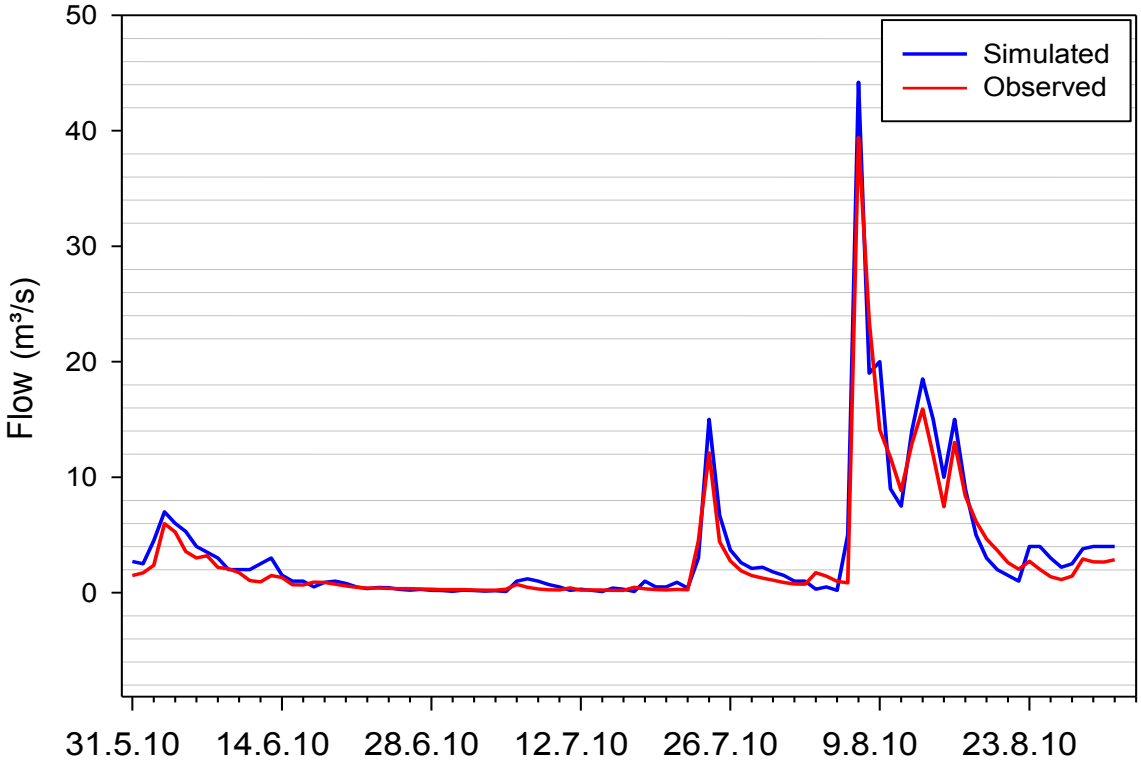

Figure 4.33: Simulated Flow versus Observed Flow from 31.05.2010 to 31.08.2010 Based on Soil Moisture Extracted from ALOS PALSAR Image on 31.05.2010.

Table 4.7: Model Simulation Results from 31.05.2010 to 31.08.2010.

Applied SAR data from 31.05.2010	Neundorf Station	Peak flow (m^3/s)	Mean flow (m^3/s)	RMSE	U
ALOS PALSAR	Simulated	42.23	3.67	1.42	0.09
	Observed	39.40	3.16		
TSX				1.58	0.12
	Simulated	44.20	3.77		

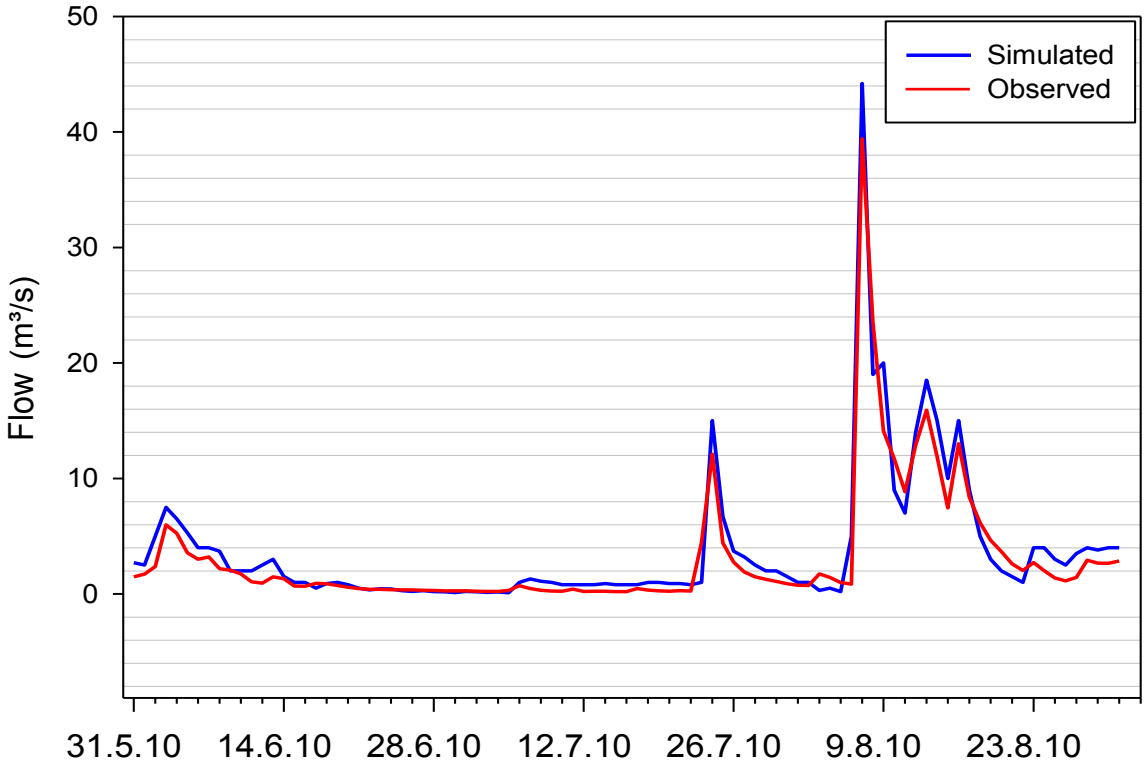

Figure 4.34: Simulated Flow versus Observed Flow from 31.05.2010 to 31.08.2010 Based on Soil Moisture Extracted from the TSX Image on 31.05.2010.

Table 4.8: Model Simulation Results from 17.06.2010 to 31.08.2010.

Applied SAR data from 17.06.2010	Neundorf Station	Peak flow (m^3/s)	Mean flow (m^3/s)	RMSE (m^3/s)	U
TSX	Simulated	43.77	3.92	1.51	0.11
	Observed	39.40	3.36		

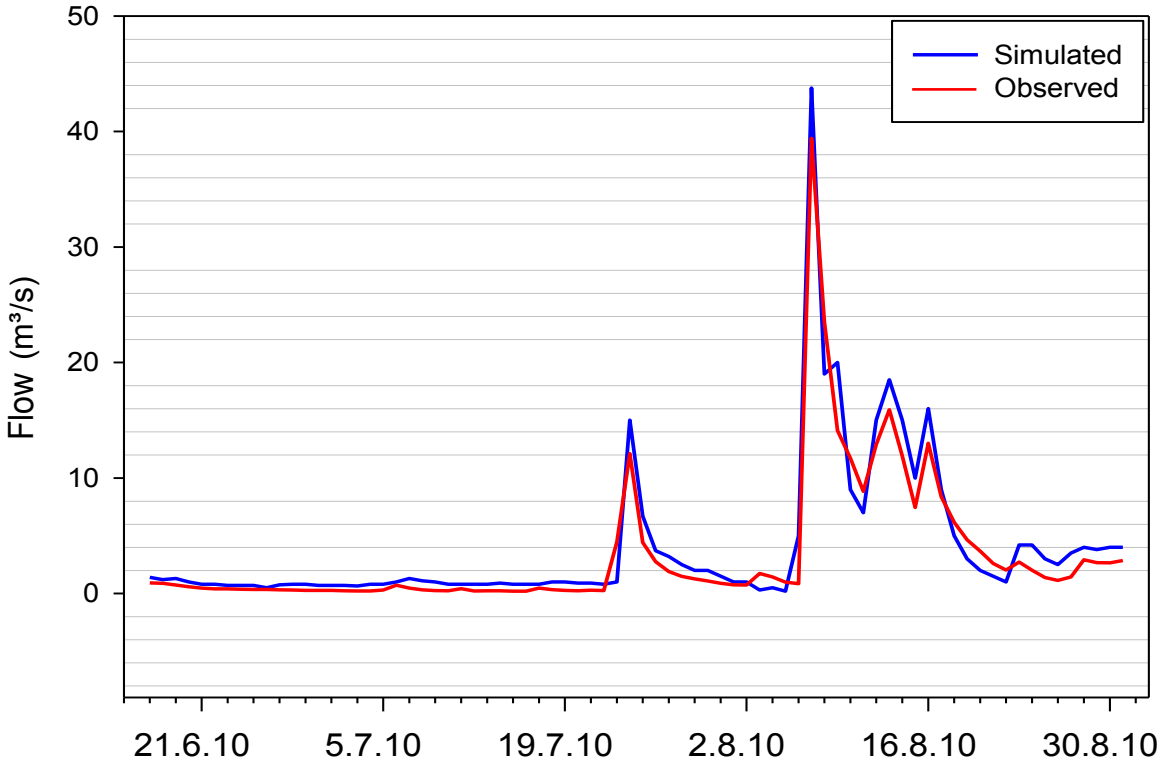

Figure 4.35: Simulated Flow versus Observed Flow from 17.06.2010 to 31.08.2010 Based on Soil Moisture Extracted from the TSX Image on 17.06.2010.

Chapter 5: Discussion of Results

5.1 Watershed Generation

In numerous studies examined the sensitivity of terrain attributes to DTM data source and grid resolution has been and several works explored what resolution is needed to accurately represent the key hydrological and geomorphical processes operating in selected landscapes (Wolock and Prices 1994; Quinn et al., 1995 & Moore, 1996). In this study high-resolution ALS-DTM 2m was used to delineate the boundaries of Gottleuba Catchment. To examine the accuracy of the applied DTM, a surveying that yielded elevations at definite points using a level device along reference line A-A was carried out under a dense canopy located in the middle of the study area. The levelling observations are listed in Table 7 in Appendix 1. The reference line profile was drawn as shown in Figure 5.2; the line slope was estimated as 7.3 %, this value was compared to the slope of the same line derived from the applied DTM, which was estimated to be 7.5 %. This result achieved a high accuracy of 97 %, subsequently positively reflected in the accuracy of the delineated watershed boundaries of the Gottleuba Catchment. The total area of the DTM generated watershed was 198.72 sqkm, the observed area of the watershed from the topographic maps obtained from the GeoSN amounts to 194.13 sqkm (see Figure 5.1) which corresponds to accuracy of 97.7 %.

DTM reconditioning using the drainage-network topographic dataset and the high-resolution ALS-DTM 2m was applied in the AHT. It is an implementation of the AGREE method developed at the Center for Research in Water Resources at the University of Texas at Austin. AGREE-DTM adjusts the surface elevation of the DTM to be consistent with stream coverage. It ''pushes'' the raw DTM along the stream to create a distinct profile along the streams which otherwise does not exist in raw DTMs. This is mainly due to lack of elevation data along streams in raw DTMs. The example in Figure 5.3 illustrates a stream cross-section profile B-B in the original DTM and the generated AGREE-DTM.

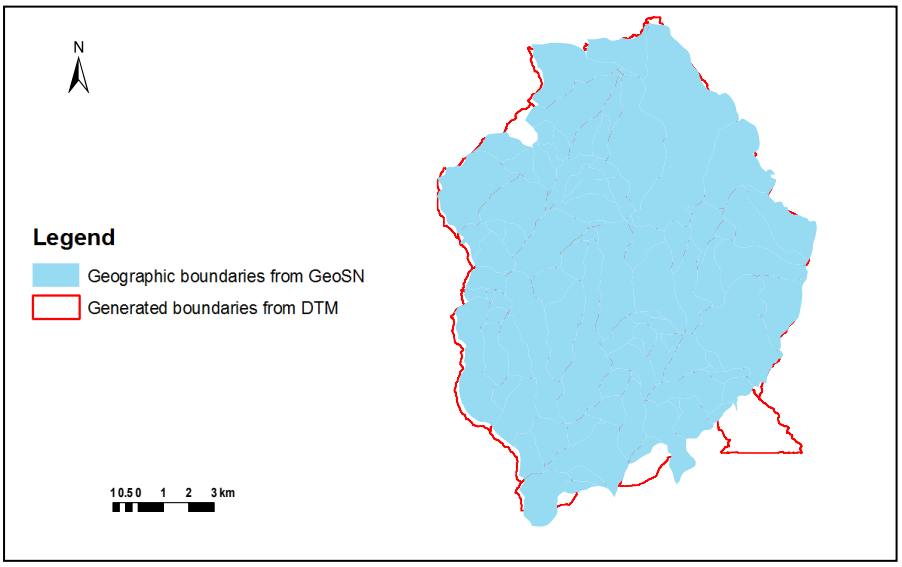

Figure 5.1: Generated and Geographic Boundaries of Gottleuba Catchment.

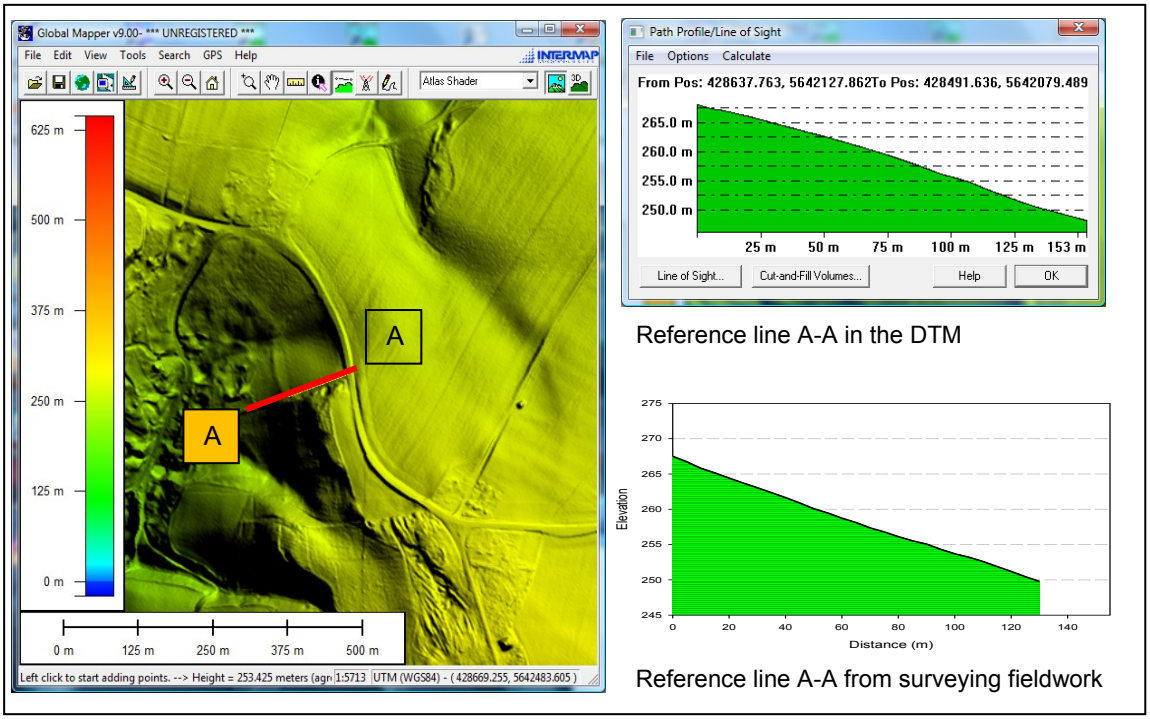

Figure 5.2: Reference Line Profile A-A.

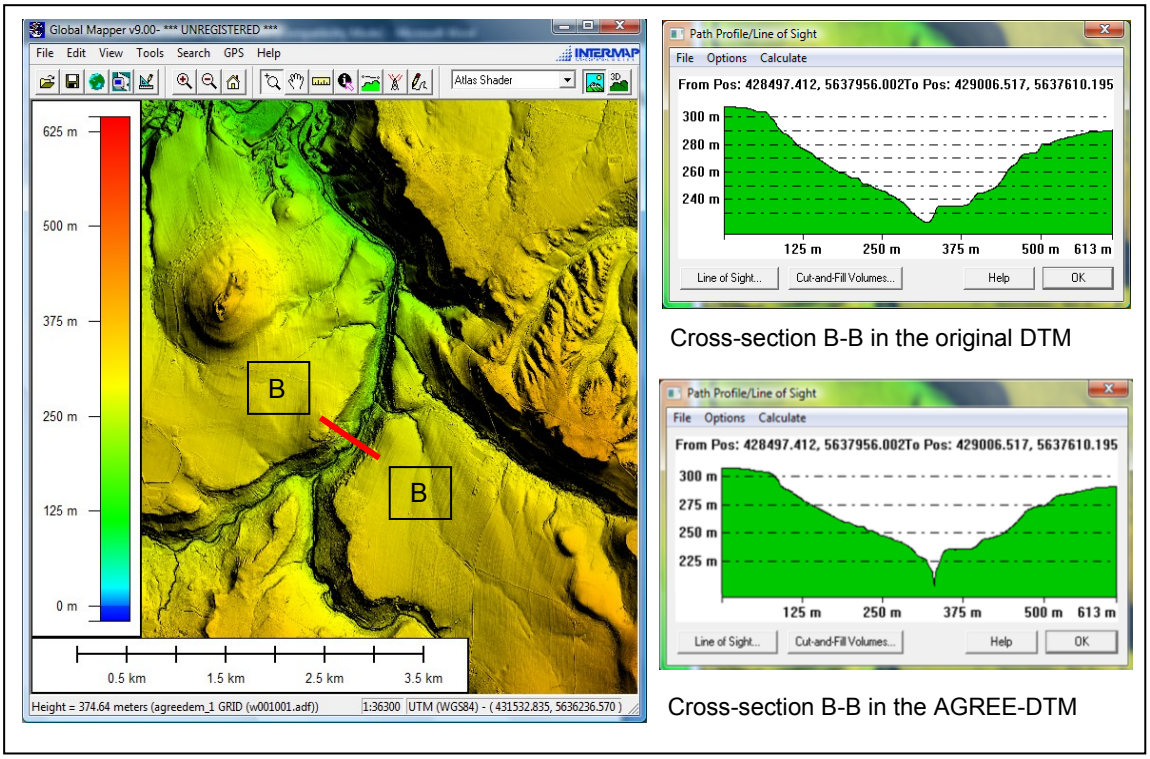

Figure 5.3: Stream Cross-Section Profile B-B.

5.2 Soil Moisture Extraction

The applied SAR data (TSX data with 9.65 GHz, λ = 3.0 cm, θi = 31˚ and 43˚ and ALOS PALSAR data with 1.27 GHz, λ = 25 cm, and θi = 34) in this study have different parameters, which mainly govern the behaviour of radar signals with the soil moisture. The like-polarisation HH is the common parameter for these data; this is because the cross-polarised return is usually weaker than the like-polarised return (CCRS RS Tutorial). The backscattering coefficient σ° was found to be more sensitive at like-polarisations (VV, HH) compared to cross-polarisations (VH, HV) (Bandyopadhyay, 1995).

The direct comparison between the backscattering coefficient and the in-situ measured soil moisture shows that σ° increases linearly with soil moisture for both TSX and ALOS PLASAR data (confirms previous studies, e.g. Ulaby et al., 1986 & Baghdadi et al., 2008). The relationship between soil moisture content and backscattering coefficient was determined at 43˚, 34° incidence angles and 9.65 plus 1.27 GHz on 31.05.2010. With the increase in frequency from 1.27 to 9.65 GHz, the values of the backscattering coefficient from bare soil increases from the range of (-15.58 dB to -13.76 dB) to (-10 dB to -8.33 dB), but sensitivity and correlation were better at 1.27 GHz as compared to 9.65 GHz. Therefore, for soil-moisture sensing lower frequencies are preferable to higher frequencies. Moreover, lower frequencies have additional advantages like a higher penetration capability in soil profile (Troch et al., 1997). For vegetation fields, the correlation between soil moisture and backscattering coefficient in the case of lower frequency is approximately doubled (R^2 increases from 0.44 to 0.85). These results agree with the reported results by Schumullius & Furrer (1992); they concluded that the L-band is the better for soil moisture determination under vegetation cover.

Furthermore, for bare fields the correlation between the measured soil moisture and backscattering coefficient was higher than the vegetation fields for the same SAR data type. For ALOS PALSAR data, the coefficient of determination for bare soil was 0.91, while in the case of vegetation fields, it equals to 0.85. For TSX data, the coefficient of determination for bare soil was 0.82, and for vegetation field 0.44.

This confirms the results of Tansly & Millington (2001). They explained that the sensitivity of σ° to soil moisture is in general decreased by the presence of a vegetation cover due to increased scattering and attenuation of the electromagnetic signal. The attenuation is in general a function of the vegetation parameters such as plant height, density, water content and shape of the plant. In addition, the vegetation layer contributes a backscatter component of its own due to volume scattering (Demirican et al., 1992). It is believed that water and chlorophyl content of the vegetation is mainly responsible for scattering and absorption (Behari, 2005).

The relationship between the measured soil moisture and backscattering coefficient extracted from the TSX data on 31.05.2010 (θi = 43˚) and 17.06.2010 (θi = 31˚) illustrates that σ° increases with the increase of incidence angle and soil moisture. With the decrease in incidence angle from 43˚ to 31˚,

the values of the backscattering coefficient from bare soil decreases from the range of (-10 dB to -8.33 dB) to be (-13 dB to -10 dB), but the achieved sensitivity and correlation were better at the lower incidence angle than at the higher one.

The measured TDR soil moisture-values were obtained on 31.05.2010, ranging between 14.1 and 47.3 %. For the data collected on 17.06.2010, the range of the measured soil-moisture values was between 11.2 and 25.3 %. These ratios show that the water content of the examined fields on 17.06.2010 were higher than the fields examined on 31.05.2010.

As soil moisture increases, the greater dielectric discontinuity between soil and air causes higher radar backscattering coefficients. At higher moisture values, however, variations reduced due to spatial variability are much lower than at lower soil values (Behari, 2005). Figure 6.1 shows a comparison between two extracts from the applied TSX data, fields with lower water they content appear darker than fields with higher water content. This is due to the increase of the radar backscattering coefficient by 3 dB.

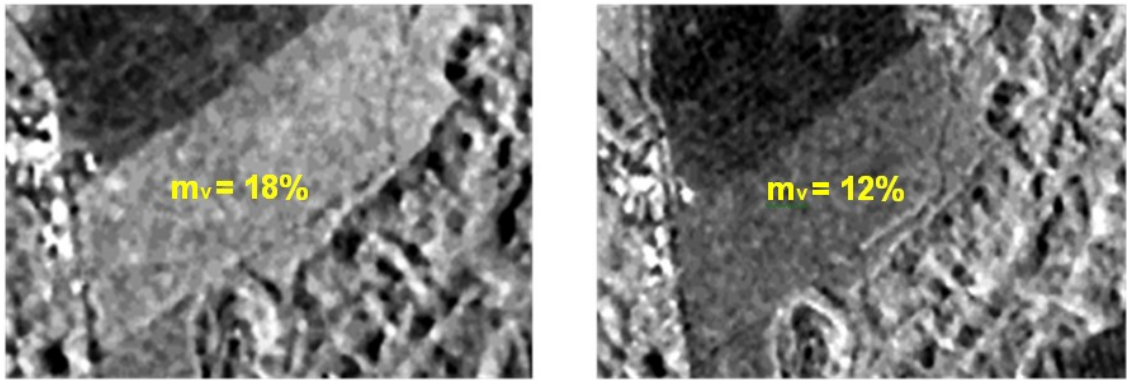

(a) (b)

Figure 5.4: a) Extract from TSX Image Obtained on 31.05.2010,
b) Extract from TSX Image Obtained on 17.06.2010.

For vegetation fields, the correlation between the moisture and backscattering coefficient obtained from TSX on 17.06.2010 was higher than the correlation obtained from TSX data on 31.05.2010. (R^2 increased from 0. 44 to 0.56). The low value of R^2 is partly attributed to the surface roughness and partly to the crop cover.

The deduced regression equations from the direct relationship between the measured soil moisture and backscattering coefficient for each SAR data were applied to generate the soil-moisture maps. Forests and urban areas represented obstacle to retrieve the soil maps. Hence, subsequently they were

excluded from the images and appeared as ''missed data'' (white zones). Since these missing parts are required as a data entry of the soil moisture for the hydrological modelling of each sub-basin, their soil moisture values were determined from the nearest neighbour pixels in each corresponding sub-basin and subsequently averaged in ArcGIS.

5.3 Hydrological Modelling

The observed flow from Neundorf hydrological station was applied to evaluate the simulated one from the model. Neundorf station is the nearest station to the mouth of the basin (about 5 km), so it represents more than 60 % of the whole catchment outlet flow.

The results of the hydrological modelling show that the simulated hydrograph, which applied the extracted soil moisture based on the ALOS PALSAR data, is more identical to the observed hydrograph than the simulated hydrographs that used the extracted soil moisture from the TSX data. Moreover, the simulated hydrographs that used the extracted soil moisture from the TSX on 17.06.2010 with a low incidence angle (31˚) is more precise than the simulated hydrographs that used the extracted soil moisture from the TSX on 31.05.2010 with a high incidence angle (43˚).

The acquired results from the hydrological modelling confirmed the results obtained from the direct comparison between the backscattering coefficient and the in-situ measured soil moisture. Furthermore, the use of HEC-HMS as a tool to examine the potential of the spaceborne SAR data for the extraction of soil moisture fulfilled the suggested methodological requirements. The present study is considered one of the earliest which applied this approach.

Meteorological data (precipitation records, global radiation, relative humidity, wind speed, maximum and minimum air temperature) were applied to simulate the soil moisture values in BROOK 90. The simulated soil moisture values were used in the SMA Method to obtain the flow hydrograph for the past ten years. A reasonable match between the modelled hydrographs and the observed one was achieved with RMSE = 1.62 and U = 0.38.

Chapter 6: Conclusions and Recommendations

6.1 Conclusions

The present study attempts to investigate the behavior of spaceborne SAR signals (TerraSAR-X and ALOS PALASAR-L band) as a function of soil moisture over bare and vegetated soil in the Gottleuba Catchment in Saxony, Germany. The acquired TSX data were obtained at different incidence angles (31° and 43°) with HH like-polarised radar modes, the obtained ALOS PALSAR image has an incidence angle 34° and HH polarisation mode. SAR data were analysed and compared with field-truth measurements of the soil moisture using a TDR - HH2 Moisture Meter. Based on rainfall records, the discharge in the Gottleuba Catchment was modelled using the extracted soil moisture values from the SAR data in the HEC-HMS software. The watershed boundaries and the geometric characteristics of the Gottleuba Catchment were generated using a high-resolution ALS-derived DTM (2m).

The results of the present study allow the following main conclusions:

1- The direct comparison between the backscattering coefficient in HH polarisation and the in-situ measured soil moisture shows that σ° increases linearly with soil moisture; moreover, it reveals a good correlation in bare fields. On the other hand, the correlation obtained for grass and crop fields was low.

2- The analysis of SAR data confirmed a significantly higher sensitivity of the L-band radar backscattering coefficient than the TSX to the soil moisture content.

3- In SAR images zones with low soil-water content appear darker than the high water content zones. Moreover, the TSX backscattering coefficient of the same fields is lower for the image with an incidence angle of 31° than the image with an incidence angle of 43° but the sensitivity and correlation were better at the lower incidence angle than at the higher one. In essence, the sensitivity of radar signals increases with increase of soil moisture and with the decrease of incidence angle and frequency.

4- Hydrological modelling was applied as an effective tool to assess the accuracy of the extracted soil moisture from the different SAR data. Furthermore, the simulated hydrographs confirmed the results of the direct comparison between the backscattering coefficient and the field measurements soil-moisture.

5- A precise basin model is needed to improve the spatial data entry required for the HEC-HMS simulation model. Consequently a high-resolution DTM has to be applied.

6- Provided the characteristics of the catchment are homogenous in meteorological / climatological and geo-parameters, it is justified to use a hydrological station which does not represent the whole catchment.

7- Based on meteorological data BROOK 90 yields encouraging results for the soil moisture simulation, which it is one of the difficult parameters to be measured over relatively large catchments in a cost-effective way and on a routine basis.

8- GIS and RS proved to be useful and powerful tools that can be implemented in soil- moisture mapping and hydrological modelling.

6.2 Recommendations

Although simulation models provide a greater range of information, these models are only as good as their input data and parameters, and to the degree they depict the physical processes involved. In many situations, the analyst must guess at values for some model parameters. If frequent surface soil moisture data were available, they would be valuable in the calibration and verification of models.

The results of the present study allow the following main recommendations:

1- Due to the frequent cancellation of the ALOS PALSAR data orders, it is recommended that any further orders should be placed earlier with highest priority. In addition, other SAR bands with longer wavelength and lower frequency such as P-band are recommended to be used because of their high sensitivity to soil moisture make use of its high sensitivity to soil moisture.

2- Further analysis should be carried out by integrating the extracted soil moisture from the SAR data with the retrieved soil moisture using BROOK 90 to substitute lake of radar data, especially in forest zones.

3- Soil moisture measurements alone cannot provide all the information necessary when dealing with agricultural and hydrologic problems. More physical soil properties are required such as surface roughness.

4- The Gottleuba Catchment does not have a hydrological station at its mouth. As a result, the overall outflow could not be measured. Therefore, it seems important to establish a hydrological station at the mouth of Gottleuba Catchment that improves the performance of the hydrological modelling at the basin and subsequently helps to avoid flood risks.

5- The spatial data generated from this study can be applied to many other hydrological models, such as calculating the peak discharge, to a flood forecasting system, for flood risk management, etc. Future studies can use the data generated from this research to understand other hydrological processes in the Gottleuba Catchment. Moreover, the findings of this study can be applied to other areas, which have to consider the appropriate parameters.

References

Abduwasit, G. & Qin, Q. (2004). Overview of Methods and Theories of Remote Sensing Monitoring and Exploration of Groundwater, Transactions of the CSAE, 20 (1), 184-188.

Albert, M. D., Tan, T. E., Ewe, H. T. & Chuah, H. T. (2005). A theoretical and measurement study of sea ice and ice shelf in antarctica as electrically dense media. Journal of Electromagnetic Waves and Applications, 19 (14), 1973-1981.

ALOS products (2007). Information ALOS PALSAR products for ADEN users. Reference: ALOS-GSEG-EOPG-TN-07-0001, Technical Note, ESA, 5-Apr-2007, http://earth.esa. int/download/alos/PALSAR_info_users_v1.1.pdf.

ALOS User handbook (2007). (http://www.eorc.jaxa.jp/ALOS/en/doc/ alos_u se rhb _en.pdf). Last access: 12 September 2010.

Al-Sabhan, W., Mulligan, M., Blackburn, G.A. (2003). A real-time hydrological model for flood prediction using GIS and the www. Comput., Environ. and Urban Systems 27 (2003), 9–32.

Alvarez, J., Casali, J., Gonzalez, M., & Verhoest, N. (2005). Correlation between ground measured soil moisture and RADARSAT-1 derived backscattering coefficient over an agricultural catchment of Navarre (North of Spain). Biosystems Engineering, 92 (1), 119−133.

Arwa, D.O. (2001). GIS Based Rainfall Runoff Model for the Turasha Sub Catchment Kenya, MSc. thesis. International institute for aero space survey and earth sciences, Enschede, the Netherlands.

Baghdadi, N., Aubert, M., Cerdan, O., Franchistéguy, L., Viel, C. & Martin, E. et al. (2007). Operational mapping of soil moisture using synthetic aperture radar data: application to Touch basin (France). Sensors Journal, 7, 2458−2483.

Baghdadi, N., Holah, N., & Zribi, M. (2006). Soil moisture estimation using multiincidence and multi-polarization ASAR SAR data. Journal of Remote Sensing, 27 (10), 1907−1920.

Baghdadi, N., Holah, N., Dubois, P., Prévot, L., Hosford, S. & Chanzy, A. et al. (2004). Discrimination potential of X-band polarimetric SAR data. Journal of Remote Sensing, 25 (22), 4933−4942.

Baghdadi, N., King, C., Bourguignon, A., & Remond, A. (2002). Potential of ERS and RADARSAT data for surface roughness monitoring over bare agricultural fields: application to catchments in Northern France. Journal of Remote Sensing, 23 (17), 3427−3442.

Baghdadi, N., Zribi, M., Loumagne, C, Ansart, P & Anguela, T.P. (2008). Analysis of TerraSAR-X data and their sensitivity to soil surface parameters over bare agricultural fields. Remote Sensing of Environment 112, 4370–4379.

Bandyopadhyay, S. (1995). Soil moisture and wheat growth assessment by microwave and optical remote sensing. Ph.D. Thesis, P.G. School, IARI, New Delhi, 125.

Bao, Y., Liu, L. & Wang, J. (2006). Estimation of Soil Water Content and Wheat Coverage with ASAR Image, Journ. of Remote Sensing, 10 (2), 253-271.

Behari, J. (2005). Microwave Dielectric Behavior of Wet Soils. School of Environmental Sciences, Jawaharlal Nehru University, New Delhi, India. Anamaya Publishers, New Delhi, India.

Benallegue, M., Taconet, O., Vidal-Madjar, D. & Normand (1995). The use of radar backscattering signals for measuring soil moisture and surface roughness. Remote Sensing of Environment, 53, 61-68.

Bennett, T.H. (1998). Development and application of a continuous soil moisture accounting algorithm for the Hydrologic Engineering Center Hydrologic Modeling System (HEC-HMS). MS thesis, Dept. of Civil and Environmental Engineering, University of California, Davis.

Beven, K. & Kirkby, M. (1979). A physically-based variable contributing area model of basin hydrology. Hydrological Sciences Journal, 24 (1), 43-69.

Beven, K.J. (1997). Distributed modelling in hydrology: applications of TOPMODEL. Chichester: Wiley.

Beven, K.J., Lamb, R., Quinn, P.F., Romanowicz. R. & Freer, J. (1995). Computer models of watershed hydrology. In V. P. Singh, TOPMODEL (Chapter 18, 627–668), Colorado, USA: Water Resources Publications.

Birkett, C. M. (1998). Contribution of the TOPEX NASA radar altimeter to the global monitoring of large rivers and wetlands. Water Resources Research, 34 (5), 1223–1239.

Birkett, C.M., Mertes, L.A.K., Dunne, T., Costa, M.H. & Jasinski, M.J. (2002). Surface water dynamics in the Amazon Basin: Application of satellite radar altimetry. Journal of Geophysical Research, 107 (D20), 8059–8080.

Brook, K.N., Folliott, P.E., Gregersen, H.M. & Thames, J.L. (1991). Hydrology and the Management of Watersheds. Iowa State Univ., Press, Iowa. 392p.

Bruckler, L., Wittono, H. & Stengel, P. (1988). Near surface moisture estimation from microwave measurements. Remote Sensing of Environment, 26, 101−121.

Buchroithner, M.F. & Granica, K. (1997). Applications of Imaging Radar in Hydro-Geological Disaster Management: A Review, Remote Sensing Reviews, 16, 1-134.

Burrough, P.A. (1997). Environmental modelling with geographical information systems. In Z. Kemp, Innovations in GIS 4, fourth national conference on GIS research UK (GISRUK), 143–153. London, UK: Taylor & Francis.

Buttle, J.M., Creed, I.F. & Pomeroy, J.W. (2000). Advances in Canadian Forest Hydrology, 1995 - 1998. Hydrological Processes 14, 1551-1578.

Canada Centre for Remote Sensing. Remote Sensing Tutorial: Fundamentals of Remote Sensing. (http://www.ccrs.nrcan.gc.ca/resource/tutor/. fundam/ index_eph p). Last access: 13 September 2010.

Chow, V.T., Maidment, D.R. & Mays, L.W. (1980). Applied Hydrology. McGraw-Hill New York.

Correia, F.N, Rego, F.C., Saraiva, M.D. & Ramos, I. (1998). Coupling GIS with hydrologic and hydraulic flood modelling, Water Resources Management, 12 (3), 229-249.

Correia, F.N., Saraiva, M.G. & Ramos, I. (1997). GIS-Based Flood Analysis and Floodplain Management, submitted to publication in Water Resource Management, Kluwer Academic Publishers, Dordrecht, Netherlands.

De Oliveira Campos, I., Mercier, F., Maheu, C., Cochonneau, G., Kosuth, P. & Blitzkow, D. et al. (2001). Temporal variations of river basin waters from Topex/Poseidon satellite altimetry; application to the Amazon basin. Comptes Rendus del Academie des Sciences, Paris, Sciences de la Terre et des Plane`tes, 333, 1–11.

DeBarry, P.A., Quimpo, R.G., Garbrecht, J., Evans, T.A., Garcia, L., Johnson, L.E., Jorgeson, J., Krysanova, V., Leavesley, G., Maidment, D.R., Nelson, E.J., Ogden, F.L., Olivera, F., Seybert, T.A., Sloan, W.T., Burrows, D., Engman, E. T., Binger, R., Evans, B.M. & Theurer, F. (1999). GIS modules and distributed models of the watershed (Special Report, July 1999). ASCE Task Committee on GIS Modules and Distributed Models of the Watershed.

Demirican, A., Ramach, H. & Mauser, W. (1992). Extraction of plant and soil parameters from multi-tempral ERS-1 SAR data of the Freiburg test site. Proc. First ERS-1 Symposium, 4 – 6 Nov. 1992, Cannes, France, 631–639.

DeVautier, B.A. & Feldman, A.D. (1993). Review of GIS applications in hydrologic modelling, Journal of Water Resources Planning and Management, 119 (2), 246-261.

Djokic, D., Ye, Z. & Miller. A. (1997). Efficient Watershed Delineation Using ArcView and Spatial Analyst, Proc. 17th Annual Esri User Conference, San Diego, CA.

Dubois, P., Van, J.J., & Engman, E.T. (1995). Measuring of soil moisture with imaging radars. IEEE Transactions on Geosciences and Remote Sensing, 33 (4), 915−926.

Engman, E. T. & Gurney, R. J. (1990). Remote Sensing in Hydrology. Chapman & Hall, London, UK.

Engman, E.T. (1991). Applications of Microwave remote sensing of soil moisture for water resources and agriculture. Remote Sens. Environ, 35 (2-3), 213-226.

Engman, E.T. & Gurney, R.J. (1991). Remote Sensing in Hydrology. Chapman and Hall, New York.

Engman, E.T., Chauhan, N. (1995). Status of microwave soil moisture measurements with remote sensing, Remote Sensing of Environment, 51 (1), 189-198. January 1995,

Federer, C.A., BROOK90 (1995). a simulation model for evaporation, soil water, and stream flow, Version 3.1. computerfreeware and documentation. USDA Forest Service, Durham, USA, 1995.

Frey, C. (2004). What does GIS Bring to Hydrologic Modelling, URL: http://geosun.sjsu.edu/paula/285/285/cf_sem.htm#Hydrologic_modeling, S JSU Geology Department, San Jose State University. Last access: 25 September 2010).

Fritz, T. & Eineder, M. (2008). "TerraSAR-X Basic Product Specification Document", TX-GS-DD-3302, Issue 1.5, February 2008.

Fung, A.K. (1994). Microwave Scattering and Emission Models and their Applications. Boston, MA: Artech House, 573.

Garbrecht, J., & Martz, L.W. (1999). Digital Elevation Model Issues in Water Resources Modeling, Proceedings of the 19th Esri Users Conference, San Diego, CA.

Goodchild, M.F., Haining, R., & Wise, S. (1992). Integrating GIS and spatial data analysis: Problems and possibilities. Journal of Geographical Information Systems, 6, 407-423.

Grimshaw, D.J. (1994). Bringing Geographical Information Systems into Business, Longman, London.

Grove, M., Harbor, J. & Engel, B. (1998). Composite versus distributed curve numbers: effects on estimates of storm runoff depths: Journal of the American Water Resources Association, 34, 1015-1023.

Gumbo, B., Munyamba, N., Sithole G. & Savenihe, H.G. (2001). Coupling of Digital Elevation Model and Rainfall-Runoff Model in Stonn Drainage Network Design, Proceedings of the 2nd WARFSAIWaterNet Symposium: Integrated Water Resources Management: Theory, Practice, Cases, 30-31, Cape Town.

Guo Xiaoyin & Cheng Guodong (2004). Advances in the Application of Remote Sensing To Evapotranspiration Research, Advance in Earth Sciences, 19 (1), 107-114.

Gustafsson, P. (1993). High resolution satellite data and GIS as a tool for assessment of groundwater potential of semi-arid area. In: Sixth Thematic Conference on Geologic Remote Sensing. 8 -11 February, 1993 at Pasadena, California, USA.

Hallberg, G.R., Hoyer, B.E. & Rango, A. (1973). Application of ERTS-1 imagery to flood inundation mapping, NASA Special Publication No. 327, Symposium on significant results obtained from Earth Resources Satellite 1, (1A), 745-753.

Hellwegger, F.L. & Maidment, D.R. (1999). Definition and connection of hydrologic elements using geographic data, Journal of Hydro logic Engineering, 2 (1), 10-18.

Hess, L.L., Melack, J.M., Novo, E.M.L.M., Barbosa, C.C.F., & Gastil, M. (2003). Dual-season mapping of wetland inundation and vegetation for the central Amazon basin. Remote Sensing of Environment, 87 (4), 404–428.

Hetherington, E.D. (1987). The Importance of Forests In the Hydrological Regime. Canadian Aquatic Resources, Canadian Bulletin of Fisheries and Aquatic Sciences 215, Healy MC, Wallace RR. Department of Fisheries and Oceans: Ottawa, 179-211.

Hu, X., Gong, J. & Pan, J. (2003). Current Situation of Remote Sensing Technology in the Contemporary Era and its Developing Tendency, Engineering Journal of Wuhan University, 36 (3A), 195-198.

Huang, Y., Hu, W. & Zhang, A. (2006). Flood-Causing Torrential Rain Forecasting and Warning System for Huaihe River, Meteorological Monthly, 32 (5), 105-109.

Hydrology Handbook (ASCE Manual and Reports on Engineering Practice) (1996). American Society of Civil Engineers; 2 nd edition (June 1996).

Ijjas, G. & Rao, Y.S. (1992) Passive microwave remote sensing of soil moisture from aircraft in Hungary. Journal of Remote Sensing, 13 (3), 471–79.

Jackson, J. & Schmugge, J. (1989). Passive Microwave Remote Sensing System for Soil Moisture: Some Supporting Research. IEEE Transactions on Geosciences and Remote Sensing, 27 (2).

Jacovides, C.P. & Kontoyiannis, H. (1995). Statistical procedures for the evaluation of evapotranspiration computingmodels. Agric. Water Manage. 27, 365–371.

Jagadeesha, C.J. (1999). Water Resources Development and Management, Asia's first GIS/GPS/RS/ monthly magazine (November-December).

King, K.W., Arnold, J.G. & Bingner, R.L. (1999). Comparison of Green-Ampt and curve number methods on Goodwin Creek watershed using SWAT, Transactions of the ASAE, 42 (4), 919-925.

Krishnamurthy, J. & Srinivas, G. (1995). Role of geological and geomorphological factors in groundwater exploration: A study using IRS-LISS-II data. Journal of Remote Sensing, 16, 2595-2618.

Krishnamurthy, J. , Venkatesh, K.N., Jayraman, V. & Manivel, M. (1996). An approach to demarcate groundwater potential zones through remote sensing and a geographical information system. Journal of Remote Sensing, 7, 1867-1884.

Le Hégarat, S., Zribi, M., Alem, F., Weisse, A. & Loumagne, C. (2002). Soil moisture estimation from ERS/SAR data: Toward an operational methodology. IEEE Transactions on Geoscience and Remote Sensing, 40 (12), 2647−2658.

Leopold, L.B., Wolman, M.G., & Miller, J.P. (1964). Fluvial Processes in Geomorphology. W.H. Freeman, San Francisco, California.

LfULG (Saxon State Office for Environment and Geology, 2004). Event analysis August 2002 flood in the watercourses of the Eastern Mountains. Saxoprint GmbH, Saxony, Germany.

Lillesand, T.M. & Kiefer, R.W. (1979), (1994), (2000) and (2008). Remote Sensing and Image Interpretation, John Wiley and Sons, New York.

Liu, C., Xia, J. & Guo, S. (2004). Advances in Distributed Hydrological Modeling for Yellow River Basin, Advances in Water Science, 15 (4), 95 - 499.

Liu, D., Li, F. & Huang, Y. (2005). The Application of Remote Sensing Technology in the Campaign of Anti-drought and Anti-flood in Heilongjiang Province, Journal of Heilongjiang Hydraulic Engineering College, 32 (2), 110-111.

Liu, S. & Zhang, W. (2004). Distributed Hydrological Model and Integrated GIS and Remote Sensing Study, Advances in Marine Science, (22), 216-222.

Macelloni, G., Paloscia, S., Pampaloni, P., Sigismondi, S., de Matthæis, P., Ferrazzoli, P., Schiavon, G. & Solimini, D. (1999). The SIR-C/X-SAR experiment on Montespertoli: sensitivity to hydrological parameters. Journal of Remote Sensing, 20 (13), 2597-2612.

Maheu, C., Cazenave, A., & Mechoso, C.R. (2003). Water level fluctuations in the Plata basin (South America) from Topex/Poseidon satellite altimetry.Geophysical Research Letters, 30 (3), 1143–1146.

Maidment, D.R. (1993). GIS and hydrological modelling. In Goodchild, M.F., Parks, B., & Steyaert, L., Environmental modelling with GIS, 147–167. New York, USA: Oxford University Press.

Maidment, D.R. (1996). GIS and hydrological modeling - An assessment of progress. Paper presented at The Third International Conference on GIS and Environmental Modeling, Santa Fe, NM. Available: http://www.ce.utexas.edu /prof/ maidment/gishydro/meetings/santafe/santafe.htm. Last access: 02 August 2010.

Mailhot, A., Rousseau, A., & Massicotte, S. (1997). A watershed-based system for the integrated management of surface water quality: the GIBSI system. Water Science Technology, 36 (5), 381–387.

Males, R. M. & Grayman, W.M. (1992). Past, Present and Future of Geographic Infonnation Systems, Water Resources, no. 87. The Universities Council on Water Resources, 5-11.

Mangsilp, R. (2007). GIS and Hydrological Model for Flood Risk Area Assessment in Maetaeng Watershed, Chiang Kai Prvince. Fac. of Grad. Studies, Mahidol Univ. M.Sc. (Inf. Man. on Env. and Res.) no. 81.

Manson, H.R. (2003). Uncertainty and sensitivity analysis of GIS based continuous hydrological modelling, M.A.Sc. Thesis, Ryerson University, Toronto, Ontario, 127 p.

Socher, M. (2007). Flood Risk Management in the Elbe River Basin (ERB) Transposition of a New European Approach. ÚstínadLabem, 5.-6. November 2007. http://www.glowa-elbe.de/pdf/konf_nov2007/SocherUsti.pdf. Last access: 18 September 2010.

Martin, C. (Editor) (2002): Lexikon der Geowissenschaften (CD), Spektrum Akademischer Verlag GmbH, Heidelberg.

Mattia, F., Satalino, G., Dente, L., & Pasquariello, G. (2006). Using a priori information to improve soil moisture retrieval from ENVISAT ASAR AP data in semiarid regions. IEEE Transactions on Geosciences and Remote Sensing, 44 (4), 900−912.

McCuen, R.H. (1982). A Guide to Hydrologic Analysis Using SCS Methods, Prentice-Hall, New Jersey, USA.

McDonnell, R.A. (1996). Including the spatial dimension: Using geographical information systems in hydrology. Progress in Physical Geography, 20, 159-177.

Meijerink, A.MJ., Brouwer, H.A.M., Mannaerts, C.M. & Valenzuela, C.R. (1994). Introduction to the Use of Geographic Information Systems for Practical Hydrology, International Institute for Aerospace Survey and Earth Sciences (ITC), Enschede, Netherlands, 234 p.

Mertes, L.A.K., Daniel, D.L., Melack, J.M., Nelson, B., Martinelli, L.A. & Forsberg, B.R. (1995). Spatial patterns of hydrology, geomorphology, and

vegetation on the floodplain of the Amazon River in Brazil from remote sensing perspective. Geomorphology, 13, 215–232.

Metcalfe, R.A. & Buttle, J.M. (2001). Soil Partitioning and Surface Store Controls on Spring Runoff From A Boreal Forest Peatland Basin In North-Central Manitoba, Canada. Hydrological Processes 15, 2305-2324.

Miller, R.C., Guertin, D.P., & Heilman, P. (2004). Information technology in watershed management decision making. Journal of the American Water Resources Association, AWRA, April, 2004, 40 (2), 347–357.

Mohan & Shrestha, M.N. (2000). A GIS based Integrated Model for Assessment of Hydrological change due to Land use modifications, proceeding of symposium on Restoration of Lakes and Wetlands, Indian Institute of Science, November 27-29, 2000, Banglore, India.

Moore, I.D., Turner, A.K., Wilson, J.P., Jenson, S.K. & Band, L. (1993). GIS and land surface-subsurface process modelling. In M. F. Goochild, B. Parks, & L. Steyaert, Environmental modelling with GIS, 196 – 230. New York, USA: Oxford University Press.

Moore, I.D. (1996). Hydrologic-modelling and GIS. GIS and Environmental Modelling: Progress and Research Issues (Goodchild, M.F., Steyaert, L.T. & Parks, B.O., editors). Fort Collins, Colombia, 143-148.

Moran, M.S., Daniel C., Jiaguo, Q. & Edson, E. (2000). Soil moisture evaluation using multi-temporal synthetic aperture radar (SAR) in semiarid rangeland, Journal of Agricultural and Forest Meteorology 105, 69–80.

Moran, M.S., Inoue, Y., Barnes, E.M. (1997). Opportunities and limitations for image-based remote sensing in precision crop management. Journal of Remote Sensing 61, 319-346.

Morgan, T.R. & Polcari, D.G. (1991). Get set! Go for mapping, modeling, and facility management. Proceeding of Computers in the Water Industry Conference, AWWA, Houston, TX.

Morrison, R.B. & White, P.G. (1976). Monitoring flood inundation, in ERTS-1 A New Window on our Planet, 196-208, U.S. Geological Survey Professional, 929.

Müller, U. (2008). Flood protection with dams and flood control reservoirs-before and after the extreme flood event of August 2002, Saxon, Dams and Reservoirs 2008, 18 (2), 85-91.

NAYLOR, T.H. (1970). Computer Simulation Experiment with Models of Economic System. John Wiley Company.

Nelson, E.J., Jones, N.L. & Jorgeson, J.D. (1995). A comprehensive environment for watershed modelling and hydrological analysis. In Water

resources engineering, proceedings of the first international conference August 14–18, 829–833. San Antonio, TX: American Society of Civil Engineers.

NOHRSC (2005). Unit Hydrograph Technical Manual. Retrieved May 26, 2009, from National Operational Hydrologic Remote Sensing Center: http://www.nohrsc.noaa.gov/technology/gis/uhg_manual.html. Last access: 25 August 2010.

Nyberg, L., Manfred, S., Mellander, P., & Bishop, K.H. (2001). Soil Frost Effects On Soil Water and Runoff Dynamics Along A Boreal Forest Transect: 1. Field Investigations. Hydrological Processes, 15, 909-926.

Obled, C.H., Wendling, J. & Beven, K. (1994). The sensitivity of hydrological models to spatial rainfall patterns: an evaluation using observed data, Journal of Hydrology, 159, 305-333.

Oh, Y. (2004). Quantitative retrieval of soil moisture content and surface roughness from multipolarized radar observations of bare soil surfaces. IEEE Transactions on Geoscience and Remote Sensing, 42 (3), 596−601.

Olivera, F., Lear, M., Famiglietti, J. & Asante, K. (2002). Extracting low-resolution river networks from high-resolution digital elevation models. Water Resour. Res. 38 (11).

Pang, Z., Fu, J. & Li, J. et al. (2004). Remote Sensing Model for Estimating Evapotranspiration Based on Energy Balance, Advances in Water Science, 15 (3), 364-368.

Peng W., Zhou J., He Z. & Yang C. (2008). INTEGRATED USE OF REMOTE SENSING AND GIS FOR PREDICTING SOIL EROSION PROCESS .The International Archives of the Photogrammetry, Remote Sensing and Spatial Information Sciences. Vol. XXXVII. Part B4.

Peter, F., Hans, M.G. & Leonard, F.D. (2003). Hydrology and the Management of Watersheds, third edition. USA, Iowa State University Press.

Pitz, W. (2006). The TerraSAR-X Satellite, Proceedings EUSAR 2006, Dresden.

Radforth, N.W. & Brawner, C.O. (1977). Muskeg and the Northern Environment, University of Toronto Press, 399.

Rahman, M.M., Moran, M.S., Thoma, D.P., Bryant, R., Collins, C.D.H. & Jackson, T. et al. (2008). Mapping surface roughness and soil moisture using multi-angle radar imagery without ancillary data. Remote Sensing of Environment, 112 (2), 391−402.

Reddy, M. (2008). Remote Sensing and Geographical Information Systems. Hyderabad, India: BSB – 500095- A.P.

Reed, S. & Maidment, D. (1998): Coordinate transformations for using NEXRAD data in GIS-based hydrologic modeling. Accepted in J. Hydrol. Engineering.

Romanowicz, R., Beven, J., Freer, J. & Moore, R. (1993). TOPmodel as an application module within WIS. Proceeding of Hydrogis '93: Application of GIS in hydrology and water resources. 19-22 April 1993, Vienna Austria, IAHS publication, 211-223.

Sabins, F. (1997): Remote Sensing, Principles and Interpretation, W.H. Freeman and Company, NewYork.

Sacramento City/County Drainage Manual, Hydrology Standards, Volume II, December 1996.

Saraf, A.K. & Jain, S.K. (1994). Integrated use of remote sensing and GIS methods for groundwater exploration in parts of Lalitpur District, U.P. In: International Conference on Hydrology and Water Resources. 20-22 December, 1993 at New Delhi, India.

Satalino, G., Mattia, F., Davidson, M., Le Toan, T., Pasquariello, G. & Borgeaud, M. (2002). On current limits of soil moisture retrieval from ERS-SAR data. IEEE Transactions on Geoscience and Remote Sensing, 40 (11), 2438−2447.

Schultz, G.A. & Engman, E.T. (2000). Remote Sensing in Hydrology and Water Management, NASA/Goddard Space Flight Center, Greenbelt, MD, USA.

Schumullius, C. & Furrer, R. (1992). Frequency dependence of radar backscattering under different moisture conditions of vegetation covered soil. Journal of Remote Sensing, 13, 2233–2245.

Seiler, R., Schmidt, J., Diallo, O. & Csaplovics, E. (2009). Flood monitoring in a semi-arid environment using spatially high resolution radar and optical data. Journal of Environmental Management, 90, 2121-2129.

Sener, E., Davraz, A., & Ozcelik (2005). An integration of GIS and remote sensing in ground water investigations: a case study in Burdur, Turkey. Hydrogeology Journal, 13, 826-834.

Seth, S.M., Jain, S.K., & Jain, M.K. (1999). Remote Sensing and GIS Application Studies at National Institute of Hydrology. Map India.

Shamsi, U.M. (2002). GIS Tools for Water, Wastewater, and Stormwater Systems, American Society of Civil Engineers, Reston, Virginia. 375p.

Singh, V.P. (1995). Computer Models of Watershed Hydrology, Water Resources. Publications, Highlands Ranch, Colorado., 1130p.

Smith, K. & Ward, R.C. (2008). Floods: Physical Processes and Human Impacts. John Wiley & Sons, Ltd., (UK).

Smith, L.C. (1997). Satellite remote sensing of river inundation area, stage and discharge: A review. Hydrological Processes, 11, 1427– 1439.

Soergel, U. (2010). Review of Radar Remote Sensing on Urban Areas, in Radar Remote Sensing of Urban Areas. Springer, New York.

Strahler, A.N. & Strahler, A.H. (1983). Modern Physical Geography. John Wiley & Sois, New York. 532p.

Sui D.Z. & Maggio, R.C. (1999). Integrating GIS with hydrological modelling: practices, problems and prospects. Computers Environment and Urban Systems, 23 (1), 33-51.

Sun, M., Liu, Z. & Lu, M. (2005). The Study of Monitoring ET by SEBEL and its Application in Water Resource Management of Hai River Basin, Journal of Irrigation and Drainage, 24 (3), 74-76.

Sun, M., Liu, Z. & Wu, B. et al. (2005). Monitoring Method of Evapo-transpiration by Remote Sensing and its Application in Water Resource Management, 16 (3), 468-474.

Susan, M., Daniel C., Jiaguo, Q. & Edson, E. (2000). Soil moisture evaluation using multi-temporal synthetic aperture radar (SAR) in semiarid rangeland, J. Agricultural and Forest Meteorology 105, 69–80.

Tansly, K.J. & Millington, A.C. (2001). Investigating the potential for soil moisture and surface roughness monitoring in dry lands using ERS SAR data. Intl. Journal of Remote Sensing, 22 (11), 2129–2149.

Tarboton, D.G., Bras, R.L. & Rodriguez-Iturbe, I. (1991). On the extraction of channel networks from digital elevation data. Journal of Hydrol. Processes, 5 (1), 81–100.

Tashpolat, T., Cui, J. & Ding, J. (2005). Study on the Means of Groundwater Distribution beneath the Oasis-Desert Ecotone in an Arid Area by Using Thermal Infrared Data, Arid Land Geography, 28 (2), 252-257.

The SAR-Guidebook (2007). Examples based on SARscape. CREASO GmbH. Sarmap.

Toyra, J., Pietroniro, A., & Martz, L.W. (2001). Multisensor hydrologic assessment of a freshwater wetland. Remote Sensing of Environment, 75, 162–173.

Tribe, A. (1992). Automated recognition of valley lines and drainage networks from grid digital elevation models: a review and a new method. Journal of Hydrology, 139, 263–293.

Troch, P.A., Vandersteene, F., Sh, Z., Hoeben, R. & Wüthrich, M. (1997). Estimating microwave observation depth in bare soil through multi-frequency

scatterometry, In: 1st EMSL User Workshop Proceedings, Ispra, Italy, April 23–24.

Tsilibaris, X., Buchroithner, M.F (1989). Spatial Frequency Analysis of Spaceborne SAR Imagery. Proceedings of the 9th EARSeL Symposium, Espoo 1989, 360-365.
Ulaby, F.T., Dubois, P.C. & Van Zyl, J. (1996). Radar mapping of surface soil moisture. Journal of Hydrology, 184, 57–84.

Ulaby, F.T., Moore, R.K. & Fung, A.K. (1982). Microwave Remote Sensing, Active and Passive, Volume I: Microwave Remote Sensing.

Ulaby, F.T., Moore, R.K. & Fung, A.K. (1986). Microwave Remote Sensing. Active and Passive. Volumes 2 and 3. From Theory to Applications. Artech House Inc., Norwood, MA.

United States Department of Agriculture (USDA) (1986). Urban Hydrology for Small Watersheds. Soil Conservation Service, Engineering Division. Technical Release 55 (TR-55).

USACE (2010). Hydrologic Modeling System HEC-HMS, Users Manual. U.S. Army Corps of Engineers. Retrieved August 2010, from http://www.hec.usace.army.mil/software/hechms/documentation.html. Last access: 18 September 2010.

U.S Army Corps of Engineers (USACOE), HEC-HMS User's Manual, Version 2.1, Hydrologic Engineering Center, Davis California.

VerWest, J. (2002). Hydrologic Analysis in Flat Terrain, URL: http://ceprofs.tamu.eduifoliveralTxAgGIS/Spring2002/verwest/verwest.htm Department of Civil Engineering, Texas A&M University.

Wang, J., Jiang, D. & Wang, H. et al. (2003). Retrieval of Annual Precipitation in Yellow River by RS, Resources Science, 25 (6), 8-13.

Wang, J., Gao, F. & Liu, S. et al. (2003). Remote Sensing Retrieval of Evapotranspiration over the Scale of Drainage Basin, Remote Sensing Technology and Application, 18 (5), 332-338.

Wang, Y. & Zhang, Y. (2005). Study on Remote Sensing of Water Depth based on BP Artificial Neural Networks, The Ocean Engineering, 23 (4), 33-38.

Wang, Z., et al. (2004). The contrast research of the methods of restraining the speckle noise of SAR images. In: XXth ISPRS Congress, Istanbul, 129-133.

Weimann, A., Schumann, A., Jörn, P., & Günther, R. (1998). Soil moisture estimation with ERS-1 SAR data in the East-German loess soil area. Journal of Remote Sensing, 19 (2), 237−243.

WET Sensor User Manual v1.3 (2005). Delta-T Devices Ltd. UK. Last access: 2 August 2010.

Wilson, J.P., Mitasova, H. & Wrightang, D. (2000). Water resources applications of GIS. Articles currently under peer review by the URISA Journal, University Consortium for Geographic Information Science (UCGIS) Web site, www.ucgis. org/apps_white/water.html. Last access: 12 September 2010.

WMS (1999). WMS watershed modelling system, reference manual. Brigham Young University- Environmental Modelling, Research Laboratory.

Wolock, D.M. & Prices, C.V. (1994). Effects of Digital Elevation Map Scale' and Data Resolution on a Topographically-Based Watershed Model. Water Resources Research, 30 (11), 3041-3052.

Wu, X. & Liu, C. (2002). Progress in Watershed Hydrological Models, Progress in Geography, 21 (4), 341-348.

Yang, G., Hu, Z. & Liu, Z. (2003). Analysis of Surface Water System in Plain with the DEM and RS, Geotechnical Investigation & Surveying, 6, 47-49.

Zhang, C., Ni, S. & Liu, Z. (2006). Review of Monitoring Soil Moisture Based on Remote Sensing, The Study of Mechanism Agriculture, 6, 58-61.

Zhang, H. & Sha, J. (2005). Study of the Method of Remote Sensing Monitoring the Soil Moisture, Journal of Chinese Agriculture, 21 (2), 301-311.

Zribi, M., & Dechambre, M. (2002). A new empirical model to retrieve soil moisture and roughness from C-band radar data. Remote Sensing of Environment, 84, 42−52.

Zribi, M., André, C., & Decharme, B. (2008). A method for soil moisture estimation in Western Africa based on ERS Scatter meter. IEEE Transactions on Geoscience and Remote Sensing, 46 (2), 438−448. Fundamentals and Radiometry, Artech House, USA.

Internet References

www1: http://wapedia.mobi/commons/Pirna.

www2:http://translate.google.com/translate?js=n&prev=_t&hl=en&ie=UTF-8&l-ayout=2&eotf=1&sl=de&tl=en&u=http%3A%2F%2Fwww.landesvermessung.sachsen.de%2Finhalt%2Fprodukte%2Fatkis%2Fdgm%2Fdgm_detail.html. Last access: 10 August 2010.

www3: http://www.erdas.com/tabid/84/currentid/1050/default.aspx. Last access: 12 August 2010.

www4: http://www.hec.usace.army.mil/software/hec-hms/. Last access: 12 August 2010.

www5: http://www.hec.usace.army.mil/software/hec-geohms/index.html. Last access: 14 August 2010.

www6: http://forums.esri.com/forums.asp?c=121. Last access: 15 August 2010.

www7: http://home.roadrunner.com/~stfederer/brook/brook90.htm. Last access: 15 Sep. 2010.

www8: http://www.nws.noaa.gov/oh/hrl/gis/data.html. Last access: 18 Sep. 2010.

Appendix 1

Tables of the measured soil moisture and the retrieved backscattering coefficients.

Table 1

	TDR- measurements (m_v %)					
	Field1	**Field 2**	**Field 3**	**Field 4**	**Field 5**	**Field 6**
Ploughed / Bare Fields on 31.05.2010	16.10	16.60	15.88	15.12	14.10	15.93
	16.20	16.82	16.68	15.13	14.31	16.83
	16.70	16.92	16.71	15.40	14.34	16.97
	17.20	17.29	16.90	15.60	14.51	16.97
	17.30	17.80	16.94	16.21	14.56	17.88
	17.32	18.20	17.85	16.35	14.98	17.98
	18.80	18.50	17.87	16.90	15.72	18.87
	18.82	18.80	17.90	17.21	15.79	18.90
S.D	1.27	1.06	1.04	1.17	1.02	1.14
m_v (average) %	17.72	17.97	17.48	16.41	15.17	17.78
σ° (TSX) dB	-8.33	-8.78	-9.05	-9.56	-10.00	-9.00

Table 2

	TDR- measurements (m_v %)					
	Field 1	**Field 2**	**Field 3**	**Field 4**	**Field 5**	**Field 6**
Grassland / Vegetations on 31.05.2010	40.40	36.4T0	36.90	37.00	33.60	37.30
	40.80	38.80	38.70	37.70	36.80	37.40
	41.90	39.10	39.50	38.90	38.10	38.30
	44.40	39.20	40.70	39.00	41.20	40.50
	44.80	39.28	40.80	40.10	42.00	40.60
	44.90	40.70	41.60	41.50	42.00	41.20
	46.30	42.90	41.80	41.90	42.20	41.30
	47.30	42.90	41.80	42.70	42.20	42.30
S.D	2.54	2.19	1.74	2.05	3.24	1.92
m_v (average) %	43.85	39.91	40.22	39.85	39.76	39.86
σ° (TSX) dB	-11.33	-13.22	-12.00	-11.93	-12.22	-13.11

Table 3

	TDR- measurements (m_v %)					
	Field 1	**Field 2**	**Field 3**	**Field 4**	**Field 5**	**Field 6**
Ploughed / Bare Fields on 31.05.2010	16.10	16.60	15.88	15.12	14.10	15.93
	16.20	16.82	16.68	15.13	14.31	16.83
	16.70	16.92	16.71	15.40	14.34	16.97
	17.20	17.29	16.90	15.60	14.51	16.97
	17.30	17.80	16.94	16.21	14.56	17.88
	17.32	18.20	17.85	16.35	14.98	17.98
	18.80	18.50	17.87	16.90	15.72	18.87
	18.82	18.80	17.90	17.21	15.79	18.90
	19.16	19.30	18.90	17.51	16.28	19.65
	19.60	19.53	19.19	18.71	17.16	17.78
S.D	1.27	1.05	1.04	1.17	1.02	1.14
m_v (average) %	17.72	17.97	17.48	16.41	15.17	17.78
σ° (ALOS) dB	-13.76	-13.95	-14.45	-14.90	-15.58	-14.24

Table 4

	TDR- measurements (m_v %)					
	Field 1	**Field 2**	**Field 3**	**Field 4**	**Field 5**	**Field 6**
Grassland / Vegetations on 31.05.2010	40.40	36.4T0	36.90	37.00	33.60	37.30
	40.80	38.80	38.70	37.70	36.80	37.40
	41.90	39.10	39.50	38.90	38.10	38.30
	44.40	39.20	40.70	39.00	41.20	40.50
	44.80	39.28	40.80	40.10	42.00	40.60
	44.90	40.70	41.60	41.50	42.00	41.20
	46.30	42.90	41.80	41.90	42.20	41.30
	47.30	42.90	41.80	42.70	42.20	42.30
S.D	2.54	2.19	1.74	2.05	3.24	1.92
m_v (average) %	43.85	39.91	40.22	39.85	39.76	39.86
σ° (ALOS) dB	-14.98	-15.78	-15.73	-15.57	-15.42	-15.63

Table 5

	TDR- measurements (m_v %)					
	Field 1	**Field 2**	**Field 3**	**Field 4**	**Field 5**	**Field 6**
Ploughed / Bare Fields on 17.06.2010	16.14	19.80	16.61	10.96	10.59	12.85
	17.08	19.92	16.80	12.70	11.29	13.95
	17.19	20.78	17.86	12.82	13.24	14.25
	18.20	21.02	18.59	13.20	13.42	14.25
	18.29	22.24	18.71	13.72	13.64	14.75
	18.83	22.30	20.40	13.74	14.38	14.75
	18.93	24.92	20.60	14.70	14.51	15.35
	20.34	25.32	20.95	15.42	15.20	15.67
S.D	1.31	2.11	1.70	1.35	1.59	0.87
m_v (average) %	18.12	22.04	18.82	13.41	13.28	14.48
σ° (TSX) dB	-10.77	-10.00	-11.44	-13.00	-12.77	-11.80

Table 6

	TDR- measurements (m_v %)					
	Field 1	**Field 2**	**Field 3**	**Field 4**	**Field 5**	**Field 6**
Grassland / Vegetations on 17.06.2010	15.12	18.78	16.10	12.85	13.19	15.23
	16.21	20.73	16.80	13.95	14.24	15.41
	17.13	22.32	17.60	14.25	14.28	16.13
	17.13	22.38	18.10	14.25	15.19	16.14
	17.15	22.43	18.90	14.75	15.28	16.18
	17.42	23.10	20.50	14.75	16.18	16.22
	18.28	23.12	20.60	15.35	16.68	16.95
	18.58	23.45	21.70	15.67	17.26	17.16
S.D	1.10	1.56	1.99	0.87	1.37	0.66
m_v (average) %	17.13	22.04	18.79	14.48	15.29	16.18
σ° (TSX) dB	-10.78	-10.43	-11.44	-13.25	-14.77	-14.68

Table 7: Levelling Field Work

Station	Backsight	Interme-diate	Foresight	Depression (m)	Levels	Distance (m)
1	0.07				**267.5**	0
2		0.84		0.77	**266.73**	5
3		1.77		0.93	**265.8**	10
4		2.43		0.66	**265.14**	15
5		3.15		0.72	**264.42**	20
6	0.33		3.85	0.70	**263.72**	25
7		1.00		0.67	**263.05**	30
8		1.70		0.70	**262.35**	35
9		2.40		0.70	**261.65**	40
10		3.15		0.75	**260.90**	45
11	0.60		3.97	0.82	**260.08**	50
12		1.21		0.61	**259.47**	55
13		1.94		0.73	**258.74**	60
14		2.56		0.62	**258.12**	65
15		3.32		0.76	**257.36**	70
16	0.42		3.89	0.57	**256.79**	75
17		1.09		0.67	**256.12**	80
18		1.67		0.85	**255.54**	85
19		2.15		0.48	**255.06**	90
20		2.88		0.73	**254.33**	95
21		3.52		0.64	**253.69**	100
22	0.45		4.00	0.48	**253.21**	105
23		1.06		0.61	**252.6**	110
24		1.78		0.72	**251.88**	115
25		2.47		0.69	**251.19**	120
26		3.21		0.74	**250.45**	125
27			3.88	0.67	**249.78**	130

Table 8: TDR Verification

Sample	Container weight (gm)	weight of (wet sample + container) (gm)	weight of (dry sample + container) (gm)	Gravimetric Soil Moisture %	Sample volume (cm^3)	Sample weight (gm)	Bulk Density %	Volumetric Soil Moisture %	TDR Readings %	RMSR %
1	447.6	628.39	605.59	14.43	98.175	157.99	1.61	23.22	23.5	**0.98**
2	364.99	552.56	518.45	22.23	98.175	153.46	1.56	34.74	33.9	
3	42.29	221.74	190.03	21.46	98.175	147.74	1.50	32.30	33.9	
4	449.7	608.74	581.42	20.74	98.175	131.72	1.34	27.83	28.6	
5	42.2	214.5	183.6	21.85	98.175	141.4	1.44	31.47	32.3	
6	138.8	317.68	285.16	22.22	98.175	146.36	1.49	33.12	31.5	
7	137.57	306.34	275.02	22.79	98.175	137.45	1.40	31.90	29.5	
8	140.69	316.6	284.51	22.31	98.175	143.82	1.46	32.69	32.5	
9	139.73	319.75	286.02	23.06	98.175	146.29	1.49	34.36	33	
10	138.88	307.46	280.23	19.26	98.175	141.35	1.44	27.74	24.5	

Appendix 2

Photos of the Tested Fields

All photos were taken by the author on the Gottleuba Catchment fields, south of Pirna, Saxony, Germany. May/June 2010.

Bare Field

Ploughed Field

Recently Sown Corn Field

Vegetated Corn Field

Grassland

TDR - HH2 Moisture Meter

Soil Moisture Sampling

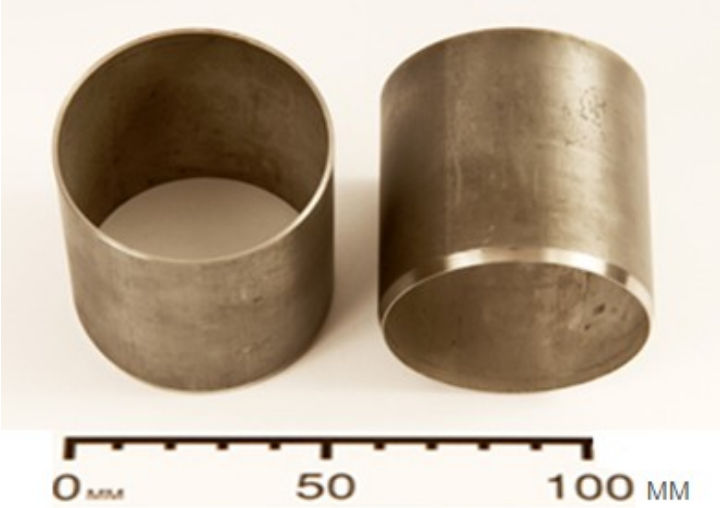

Soil Core Sampler